

Copyright

by

Jared Austin Allison

2020

**The Dissertation Committee for Jared Austin Allison Certifies that this is the  
approved version of the following Dissertation:**

**Radio Frequency Additive Manufacturing: A Volumetric Approach to  
Polymer Powder Bed Fusion**

**Committee:**

Carolyn C. Seepersad, Supervisor

Joseph J. Beaman

Richard H. Crawford

Christopher J. Tuck

**Radio Frequency Additive Manufacturing: A Volumetric Approach to  
Polymer Powder Bed Fusion**

**by**

**Jared Austin Allison**

**Dissertation**

Presented to the Faculty of the Graduate School of

The University of Texas at Austin

in Partial Fulfillment

of the Requirements

for the Degree of

**Doctor of Philosophy**

**The University of Texas at Austin**

**August 2020**

## **Dedication**

To Lexi, for her unwavering support and for believing in me when I needed it most.

## Acknowledgements

*“If I have seen further, it is by standing on the shoulders of giants.”*

*-Isaac Newton*

This work would not have been possible without the encouragement and support of many giants in my life. I am grateful to be grounded by a loving wife and parents who have never doubted my abilities and inspired me to pursue my passions. I would also like to acknowledge Dr. John Pearce for opening his lab to me and for his enduring patience in repeatedly explaining the fundamentals of electromagnetics as many times as I needed to reach an acceptable level of understanding. I am indebted to Dr. Pearce for dedicating countless hours to my experiments while giving me the autonomy to learn things for myself.

I would also like to thank my collaborators at the University of Nottingham for their contributions to this project and for welcoming me warmly during my two visits to England. Specifically, Professor Tuck, Professor Hague, Dr. Dimitrakis, and Dr. Sohaib were instrumental in the development of this work, and I am extraordinarily grateful for their efforts. I extend my appreciation to my dissertation committee for challenging me throughout this project and for offering their attention and guidance in preparing this document. I am also thankful for the numerous professors at the University of Texas who have personally mentored me and imbued me with valuable knowledge throughout my time as a graduate student.

I am fortunate to have been involved in a research lab that fostered companionship in addition to collaboration, and there are several members of my lab that deserve special recognition. I would like to thank my undergraduate assistants, Ashley Yang and Miranda

Georgeson, for their involvement in this project. I also appreciate Conner Sharpe and Nick Rodriguez for being great listeners and helping me overcome numerous technical challenges. Thank you to Clint Morris, Michelle Pang, David Debeau, Tyler Wiest, Oliver Uitz, Ademola Oridate, Hongtao Song, Andrew Allan, and Connor Gunsbury for providing a pleasant work environment and facilitating thought-provoking discussion. I am immensely grateful for Dr. Carolyn Seepersad for the incredible amount of support she has contributed over the past five years. I do not take the opportunities she has given me for granted. I am also thankful for my colleagues outside of engineering including Kirsten Hall, Sierra Senzaki, Kristin Foringer, Kaitlyn Farrell Rodriguez, and Sneha Tharayil who have offered alternate perspectives to my work. Furthermore, to anyone that has not been mentioned but has helped me along the way, thank you for your guidance and mentorship. If I have accomplished anything, it has been through the love and care of many individuals that have impacted my life.

This material is based on work supported by the National Science Foundation under Grant No. CMMI-1728015. Any opinions, findings, and conclusions or recommendations expressed in this material are those of the author and do not necessarily reflect the views of the National Science Foundation.

## **Abstract**

# **Radio Frequency Additive Manufacturing: A Volumetric Approach to Polymer Powder Bed Fusion**

Jared Austin Allison, PhD

The University of Texas at Austin, 2020

Supervisor: Carolyn C. Seepersad

Polymer powder bed fusion (PBF) additive manufacturing offers a number of advantages over conventional manufacturing techniques, particularly in the areas of reduced tooling costs and the added geometric complexity available to designers. However, existing methods require heat to be applied to the powder bed at each layer to fuse the powders and form parts. The layer-wise heating strategies used in current PBF processes contribute to a reduction in the mechanical performance of the parts and increase the time required to fabricate them.

To address these issues, a volumetric heating strategy is implemented through a novel radio frequency additive manufacturing (RFAM) process. Radio frequency (RF) radiation is a heating mechanism that is capable of penetrating into materials to cause a simultaneous temperature rise throughout the material volume. Given the insulating nature of most polymers, electrically conductive dopants can be added to a polymer powder bed such that the effective composite properties are suitable for RF heating. By selectively patterning the dopant in the powder bed and applying RF radiation, heat generation can be contained to the RF-absorbing doped region with little effect to the surrounding powder

bed. With powder mixtures of nylon 12 as the polymer and graphite as the dopant, it is possible to fuse the host polymer using RF radiation as the sole energy source.

One of the consequences of creating parts with this method is the complex interaction between the part geometry and the applied RF field that can cause non-uniform heating to develop within the part. Aided by computational design approaches, methods for improving the heating uniformity are proposed including a functional grading scheme to vary the dopant concentration throughout the powder bed. To validate the computational models and further develop the RFAM process, the design of a prototype machine capable of three dimensional dopant patterning is presented. The prototype system is used to create RFAM parts and evaluate the effectiveness of the different strategies aimed at improving the heating uniformity within the doped powder beds. As a result of this work, the feasibility of a volumetric, RF-assisted additive manufacturing process is demonstrated.



## Table of Contents

<b>List of Tables .....</b>	<b>xii</b>
<b>List of Figures.....</b>	<b>xiii</b>
<b>Chapter 1: Introduction .....</b>	<b>1</b>
1.1 Issues Associated with Layer-Wise Polymer Powder Bed Fusion (PBF) .....	1
1.2 The Need for Volumetric Sintering .....	3
1.3 Research Objectives.....	4
1.3.1 Proposed Radio Frequency Additive Manufacturing System.....	4
1.3.2 Summary of Research Tasks.....	6
<b>Chapter 2: Radio Frequency Heating Background and Applications.....</b>	<b>8</b>
2.1 Radio Frequency Heating .....	8
2.1.1 Fundamentals of Electromagnetic Heating.....	8
2.1.2 Impact of Radiation Frequency.....	14
2.2 RF Heating Applications.....	16
2.2.1 History of RF Heating.....	16
2.2.2 Potential Challenges.....	18
2.3 Electrically Conductive Polymer Composites .....	18
2.3.1 Applications of Electrically Conductive Polymer Composites .....	18
2.3.2 Percolation Limit in Electrically Conductive Composites.....	19
2.3.3 Candidate Materials for RFAM .....	20
2.4 Closure .....	23
<b>Chapter 3: Electrical Property Measurement and Radio Frequency Heating of Graphite-Doped Polyamide (Nylon) 12 .....</b>	<b>24</b>
3.1 Permittivity Measurements of Graphite-Doped Nylon 12 Powders .....	24
3.1.1 Graphite-Doped Nylon 12 Composites.....	24
3.1.2 Impedance Spectroscopy to Measure Dielectric Properties.....	25
3.1.3 Electrical Properties of Graphite-Doped Nylon 12 Mixtures .....	28
3.2 RF Heating Experiments for Graphite-Doped Nylon 12 Mixtures.....	36
3.2.1 Experimental Apparatus.....	36

3.2.2	Sample Preparation .....	38
3.2.3	RF Heating Results and Discussion .....	40
3.2.4	Mechanical Properties of Sintered Parts .....	47
3.3	Closure .....	50
<b>Chapter 4: Computational Design Strategy to Improve RF Heating Uniformity ....</b>		<b>53</b>
4.1	Prediction of Temperature Rise and Phase Transition Using Finite Element Analysis .....	53
4.1.1	AC/DC Model Parameters .....	54
4.1.2	Heat Transfer Model Parameters .....	56
4.2	Dependence of Heating Uniformity on Doped Geometry .....	59
4.3	Computational Approaches to Functionally Grade Electrical Conductivity ....	64
4.3.1	Computational Challenges with Traditional Optimization Techniques.....	64
4.3.2	Heuristic Tuning Method .....	68
4.3.3	Changing Electrode Configuration to Improve Heating Uniformity .....	80
4.3.4	Multiple Electrode Configurations to Ease Functional Grading Effort .....	83
4.4	Closure .....	86
<b>Chapter 5: Design of a Dopant Delivery Mechanism for RFAM .....</b>		<b>87</b>
5.1	System Requirements for the RFAM Process .....	87
5.1.1	Dopant Delivery Requirements.....	87
5.1.2	Build Chamber Requirements.....	88
5.1.3	RF Generator Requirements .....	89
5.2	Design of a Powder Deposition System.....	90
5.2.1	Powder Dosing Mechanism .....	91
5.2.2	Build Chamber Design.....	93
5.2.3	Process Planning .....	95
5.2.4	Functional Grading with Powder Deposition Machine .....	98
5.2.5	Powder Deposition Limitations .....	99
5.3	Inkjet System for Patterning Dopant.....	100
5.3.1	System Design .....	100
5.3.2	Build Chamber Design.....	102
5.3.3	Functional Grading .....	103

5.4	Closure .....	104
<b>Chapter 6: RFAM Capabilities and Design Guidance .....</b>		<b>106</b>
6.1	RF Heating Experiments and Geometric Improvement.....	106
6.1.1	RF-Sintered Parts and Functional Grading Experiments.....	106
6.1.2	RF Experiments on Inkjet-Printed Samples.....	115
6.2	Design Considerations for RFAM .....	120
6.2.1	Effect of Process Parameters on Heating Uniformity.....	120
6.2.2	RFAM Design Guidance.....	127
6.3	Closure .....	132
<b>Chapter 7: Conclusion .....</b>		<b>133</b>
7.1	Summary of Work.....	133
7.2	Contributions.....	137
7.3	Future Work .....	139
7.4	Closure .....	142
<b>References .....</b>		<b>144</b>

## List of Tables

<b>Table 1.1</b>	Summary of research tasks to be addressed in this work.....	6
<b>Table 3.1</b>	Mechanical properties of laser sintered nylon 12 compared with RF-sintered properties. The error from the experimental results corresponds to the standard error of the measurements across the five samples.....	50
<b>Table 4.1</b>	Electrical properties used in simulation for doped and virgin powder regions.....	55
<b>Table 4.2</b>	Thermal properties used in the simulations, including phase change. The values corresponded to pure nylon 12 powder and were taken from sources in literature. ....	58
<b>Table 6.1</b>	Measurement comparisons between geometry predictions in COMSOL® and experimentally-fused parts. ....	113
<b>Table 6.2</b>	RFAM design guidelines with electrodes marked in purple.....	131

## List of Figures

<b>Figure 1.1</b>	RFAM conceptual design. The dopant is in each layer of the powder bed. Electrodes deliver the electromagnetic energy to the part to fuse the powders together. ....	5
<b>Figure 2.1</b>	The electromagnetic spectrum comparing the frequency and wavelength for various recognized bands. Adapted from [23].....	9
<b>Figure 2.2</b>	Circuit representation of a source and load. The source includes a voltage ( $V_S$ ) as well as a resistance ( $R_S$ ). Power dissipation across the load ( $R_L$ ) is determined by the voltage drop across it ( $V_L$ ).....	12
<b>Figure 2.3</b>	Normalized voltage across the load compared to the source voltage ( $V_L/V_S$ ) and normalized power dissipated across the load compared to its maximum ( $P_L/P_{max}$ ). ....	13
<b>Figure 2.4</b>	Standing wave formed by the superposition of a forward propagating electric field (green) and a backward propagating reflected electric field (blue). The standing wave creates nodal locations (circled in red) where the electric field remains at zero for all time instances. ....	15
<b>Figure 2.5</b>	Graphite structure adapted from [83]. Graphite is made up of carbon sheets and held together through weak Van der Waals forces.....	21
<b>Figure 2.6</b>	Chemical structure for nylon 12 adapted from [87]. Each vertex represents individual $CH_2$ groups.....	22
<b>Figure 3.1</b>	Diagram of the coaxial chamber used for impedance measurement. The diameter of the inner electrode (a) was 1.59 cm, and the diameter of the outer electrode (b) was 7.94 cm. The powder was held in place by a Teflon block that separated the two electrodes. Copper strips soldered to the electrodes provided connection to the input terminals of the impedance analyzer. ....	26
<b>Figure 3.2</b>	Circuit diagram for the impedance measurements. The parasitic R, L, and C components of the fixture must be removed from the measured impedance to determine the complex capacitance of the material. ....	27
<b>Figure 3.3</b>	Effective electrical conductivity vs. frequency for 30% graphite by weight.....	29
<b>Figure 3.4</b>	Effective electrical conductivity vs. frequency for nylon/graphite mixtures containing between 10% and 60% graphite by weight. ....	31
<b>Figure 3.5</b>	Effective electrical conductivity as a function of graphite content at 27.12 MHz .....	32
<b>Figure 3.6</b>	Relative permittivity as a function of graphite content at 27.12 MHz.....	33
<b>Figure 3.7</b>	Loss tangent as a function of graphite content at 27.12 MHz .....	35

<b>Figure 3.8</b>	Penetration depth as a function of graphite content at 27.12 MHz.....	36
<b>Figure 3.9</b>	Experimental applicator showing powder cavity, electrodes, and connections to RF generator .....	37
<b>Figure 3.10</b>	Faraday cage surrounding applicator showing IR camera mounted above the sample.....	38
<b>Figure 3.11</b>	Thin forms used to selectively dope the powder bed into regions of circular (left), square (center), and rectangular (right) cross sections. ....	39
<b>Figure 3.12</b>	Process showing how the PLA forms are used to separate doped powder from virgin. a) The chamber was filled with a base layer of virgin powder. b) The form was placed in the center of the chamber and surrounded by additional powder to create a cavity. c) The cavity was filled with graphite-doped powder. d) The form was removed to create an interface between doped and virgin powder.....	39
<b>Figure 3.13</b>	Average surface temperature of the doped region after 90 seconds of RF exposure. The doped region had a circular cross section, and the tuning parameters of the RF generator were held constant.....	41
<b>Figure 3.14</b>	Temperature profile after 5 minutes RF exposure for a doped region defined by a circular cross section. The electrodes are parallel to the top and bottom of the image, and the direction of the electric field is shown. ....	43
<b>Figure 3.15</b>	Temperature profile after 6 minutes RF exposure for a doped region defined by a square cross section. The electrodes are parallel to the top and bottom of the image, and the direction of the electric field is shown. ....	44
<b>Figure 3.16</b>	Temperature profile after 5 minutes RF exposure for a doped region defined by a rectangular cross section. The electrodes are parallel to the top and bottom of the image, and the direction of the electric field is shown. ....	44
<b>Figure 3.17</b>	Fused part created from a selectively doped powder bed in which the geometry was defined by a circular cross section. The doped region contained 30% graphite by weight, and the part was exposed to RF radiation for five minutes.....	46
<b>Figure 3.18</b>	Fused part created from a selectively doped powder bed in which the geometry was defined by a square cross section. The doped region contained 30% graphite by weight, and the part was exposed to RF radiation for seven minutes and thirty seconds.....	46
<b>Figure 3.19</b>	Fused part created from a selectively doped powder bed in which the geometry was defined by a rectangular cross section. The doped	

	region contained 30% graphite by weight, and the part was exposed to RF radiation for six minutes. ....	46
<b>Figure 3.20</b>	Position of ASTM D638 type V tensile bar with respect to RF-sintered geometry.....	48
<b>Figure 3.21</b>	ASTM D638 type V tensile bar machined from RF-sintered specimens.....	48
<b>Figure 3.22</b>	Characteristic stress/strain response from RF-sintered tensile specimens.....	49
<b>Figure 4.1</b>	Simulated domains in COMSOL®. The electrodes are represented by voltage boundary conditions. The doped region and surrounding region are distinguished by prescribing electrical properties corresponding to the doped and virgin nylon powders, respectively.....	58
<b>Figure 4.2</b>	Temperature distribution at the center cross section for a sphere (a) and cube (b). The white lines in the image correspond to the electric field lines in the powder bed. ....	59
<b>Figure 4.3</b>	Comparison between the simulated surface temperature and the experimentally measured surface temperature for doped regions with square, circular, and rectangular cross sections. The numbers in the figure correspond to the temperature measurement locations. ....	61
<b>Figure 4.4</b>	Comparison between experimental (left) and simulated geometry (right) by considering the volume in the liquid phase at the end of the simulation run .....	63
<b>Figure 4.5</b>	Cubic spline definition of electrical conductivity. The black points represent the control points of the spline. The control points are 4 dimensional where the first three are spatial, and the fourth corresponds to the electrical conductivity.....	66
<b>Figure 4.6</b>	Spline representation of the cubic geometry. The dashed lines represent the lines of symmetry imposed during the optimization. The black points are the control points for the spline, and the arrows represent the direction of movement.....	67
<b>Figure 4.7</b>	Normalized average temperature as a function of electrical conductivity.....	69
<b>Figure 4.8</b>	Flowchart describing how the heuristic tuning method was applied to the simulation results. The variables $n$ and $n_{\max}$ represented the current and maximum iteration, while $i$ and $i_{\max}$ corresponded to the current and maximum number of nodes. The proportionality constant, $K$ , was uniquely assigned to each node for every iteration.....	70
<b>Figure 4.9</b>	Mesh convergence for square prism. The x axis is the inverse of element size, and so higher values represent a finer mesh. ....	73

<b>Figure 4.10</b>	Simulated geometries used in the heuristic tuning method. The dark regions represent the doped geometry where the tuning was applied, and the location of the electrodes with respect to the geometry are indicated in purple. The dimensions of the chamber are 6.24x6.24x2.0 cm.....	74
<b>Figure 4.11</b>	Comparison between constant conductivity (left) and functionally graded conductivity (right) for a 4x4x1 cm square prism, where t represents the simulated RF exposure time and UI is the uniformity index.....	75
<b>Figure 4.12</b>	Comparison between constant conductivity (left) and functionally graded conductivity (right) for a triangular prism with a side length of 4 cm and 1 cm thickness, where t represents the simulated RF exposure time and UI is the uniformity index. ....	76
<b>Figure 4.13</b>	Comparison between constant conductivity (left) and functionally graded conductivity (right) for a 4 cm outer diameter, 2 cm inner diameter, and 1 cm thick ring, where t represents the simulated RF exposure time and UI is the uniformity index. ....	77
<b>Figure 4.14</b>	Spatially tuned conductivity for a 4x4x1 cm square prism at the center cross section. ....	77
<b>Figure 4.15</b>	Spatially tuned conductivity for a triangular prism with a side length of 4 cm and depth of 1 cm at the center cross section. ....	78
<b>Figure 4.16</b>	Spatially tuned conductivity for a 4 cm outer diameter, 2 cm inner diameter, and 1 cm thick ring at the center cross section. ....	79
<b>Figure 4.17</b>	Electrode configurations for orientation-dependent simulations of a thin ring.....	80
<b>Figure 4.18</b>	Predicted geometry and uniformity index calculations for a thin ring in a single electrode configuration with constant electrical conductivity (left), single electrode configuration with functionally graded electrical conductivity (middle), and constant electrical conductivity with multiple electrode configurations (right) .....	81
<b>Figure 4.19</b>	Electrode configurations for orientation-dependent simulations of a longhorn head. The height, width, and thickness correspond to the bounding dimensions of the longhorn head geometry.....	81
<b>Figure 4.20</b>	Predicted geometry and uniformity index for longhorn head simulations in each electrode configuration as well as the two-stage combined configuration. ....	82
<b>Figure 4.21</b>	Electrode configurations for orientation-dependent simulations of a diamond.....	83



<b>Figure 4.22</b>	Predicted geometry and uniformity index for single electrode configuration heating and functional grading for the diamond geometry .....	84
<b>Figure 4.23</b>	Predicted geometry and uniformity index for multiple electrode configurations and functional grading for the diamond geometry.....	85
<b>Figure 4.24</b>	Spatially tuned conductivity for the diamond geometry with the electrodes in the first configuration (left) and multiple configurations (right) .....	85
<b>Figure 5.1</b>	MakerBot Replicator 2 modified to pattern doped dry powders. The 3 axes of movement and their respective stages are labeled.....	90
<b>Figure 5.2</b>	Build area showing the powder dosing mechanism, build chamber, and overflow tray .....	91
<b>Figure 5.3</b>	Dosing mechanism for depositing discrete volumes of doped powder ....	92
<b>Figure 5.4</b>	Powder dispensing mechanism as implemented in the final design of the patterning machine .....	93
<b>Figure 5.5</b>	Steps detailing the separation of the powder bed from the patterning machine to enable heating in the RF generator.....	94
<b>Figure 5.6</b>	Side view representation of doped layer before (left) and after (right) spreading. Each mound of doped powder was deposited at spacing of 1.82 mm in the x and y directions, and the layer thickness was 2 mm.....	96
<b>Figure 5.7</b>	Deposition points and paths (top) compared with patterned powder (bottom) for square, triangular, and ring geometries .....	97
<b>Figure 5.8</b>	Functionally graded layer files for a square prism for the bottom (left) and top (right) layers. The colors in the image represent the powder mixture to be deposited in the (x,y) location, and the graphite content increases with increasing powder designation.....	99
<b>Figure 5.9</b>	Proposed build chamber design for the inkjet system where the chamber is divided into three regions containing nylon and carbon dopant, loose nylon powder, and nylon mixed with a binder to form the walls. ....	102
<b>Figure 5.10</b>	Possible patterns for doping a 4x4 grid of pixels to different concentrations .....	104
<b>Figure 6.1</b>	Comparison between uniformly doped samples and functionally graded samples with corresponding RF exposure times in minutes.....	107
<b>Figure 6.2</b>	Surface temperature for square prism captured at the end of the heating stage for a uniform dopant distribution (left) and functionally graded dopant (right).....	108

<b>Figure 6.3</b>	Fused ring geometry after two-stage heating where the powder bed was heated for one minute in each electrode configuration. Top/Bottom and Left/Right refer to the position of the electrodes with respect to the image. ....	109
<b>Figure 6.4</b>	Fused parts from uniform dopant concentration after heating in multiple electrode configurations with corresponding RF exposure times in minutes. Top/Bottom and Left/Right refer to the position of the electrodes with respect to the image. ....	110
<b>Figure 6.5</b>	Fused parts from square diamond geometry heated in four configurations with RF exposure times in minutes. a) Single electrode orientation with uniform dopant. b) Single electrode orientation with functionally graded dopant. c) Two electrode orientations with uniform dopant. d) Two electrode orientations with functionally graded dopant.....	112
<b>Figure 6.6</b>	Histograms comparing the aggregated, functionally graded conductivity values across the part domains for the one-stage (left) and two-stage (right) heating strategies .....	114
<b>Figure 6.7</b>	Three dimensional strut geometry as positioned in the powder bed with the electrodes marked in purple.....	114
<b>Figure 6.8</b>	Fused part removed from powder bed after two-stage heating of the thin ring lattice structure. ....	115
<b>Figure 6.9</b>	Temperature rise as a function of carbon content for inkjet-printed samples after 10 minutes of RF exposure .....	117
<b>Figure 6.10</b>	Fused part from laboratory-scale inkjet printer, showing the printed part (left) and fused part after RF exposure (right). The printed dimensions of the part were 20x20x10 mm, and the final dimensions were 16x12x4 mm.....	118
<b>Figure 6.11</b>	Temperature rise as a function of ink concentration after drying in a 140°C oven overnight .....	119
<b>Figure 6.12</b>	Tuned electrical conductivity divided into 1, 2, 4, 8, and 16 levels as well as the continuously tuned conductivity for the 4x4x1 cm square prism .....	121
<b>Figure 6.13</b>	Uniformity index as a function of the number of dopant levels used to functionally grade the powder bed.....	122
<b>Figure 6.14</b>	Simulated temperature distributions in COMSOL®, taken 5 mm from the top and bottom faces for each of the grading levels .....	123
<b>Figure 6.15</b>	Heating uniformity as a function of electrode spacing, $d$ , defined as the distance between the edge of the part and the electrode .....	124

<b>Figure 6.16</b>	Uniformity index as a function of electrode voltage .....	126
<b>Figure 6.17</b>	Simulated geometry and uniformity index for triangle with filleted corners.....	128

## **Chapter 1: Introduction**

Additive manufacturing (AM) of thermoplastic polymers typically consists of depositing material or energy on a layer-by-layer basis. Parts are created by selectively melting and re-solidifying the polymer into the cross section of the desired geometry at each layer, and the process is repeated until the entire geometry has been defined. Although there are a variety of AM classifications, the most widely used methods for thermoplastic polymers are material extrusion and powder bed fusion (PBF). In material extrusion systems, the polymer often takes the form of a filament strand that is melted and forced through a nozzle. The molten polymer is patterned into the desired shape and must re-solidify before subsequent layers can be deposited above it. PBF processes involve applying a thermal heat source to thin layers of polymer powder to selectively melt the regions of the powder bed corresponding to the part volume [1]. Powder bed fusion has an advantage over material extrusion because the powder beds in PBF processes are self-supporting and do not require support structures when fabricating overhangs and complex internal channels.

### **1.1 ISSUES ASSOCIATED WITH LAYER-WISE POLYMER POWDER BED FUSION (PBF)**

The layer-wise heating strategies implemented in existing PBF methods negatively impact the mechanical performance of printed parts and the efficiency of fabricating them. Selective laser sintering (SLS) is a polymer PBF method that has gained widespread recognition for its ability to create geometrically complex parts without the need to incorporate support structures. SLS is a layer-based process that uses a carbon dioxide laser to fuse polymer powder together to form parts. The performance of laser sintered parts is limited by the ability to precisely control the thermal conditions within the machine. Namely, the temperature of the part bed can substantially affect the quality of parts

produced [2]. The cyclic heating and cooling of each layer can contribute to inhomogeneous shrinkage and the development of internal residual stresses [3] [4] [5]. Mercelis and Kruth provide two explanations for the mechanisms that contribute to residual stress in SLS parts. The first occurs as a result of the large thermal gradients that exist around the laser spot during scanning, and the second happens during the cool-down phase when the molten top layers experience a different rate of thermal contraction versus the bottom layers [6]. Thus, the primary sources for the shrinkage and curling of SLS parts arise from the concentrated energy from the laser and the layer-wise heating that prevents the parts from cooling uniformly. The thermal conditions of SLS can also contribute to a decrease in mechanical properties. The parts tend to behave as transversely isotropic in ultimate tensile stress and modulus. The strength is generally considered isotropic within the plane of the layers with a reduction of as much as 10-15% between layers [7] [8]. Scan strategy, layer scanning time, and cooling between layers have been shown to effect the anisotropy of SLS parts [9]. The presence of thermal gradients across the surface of the powder bed can also contribute to large variations in strength that depend on the location of the part within the build chamber [10].

Selective laser sintering is further limited by the processing time required to make parts. The primary factor contributing to decreased production rates is the time required for the machine to reach thermal equilibrium. Warm-up and cool-down stages can add four hours or more to the total build time [11]. There is a waiting period associated with heating newly deposited layers of powder before sintering that can account for up to 15% of the total build time, while as much as 25% of the total time is dedicated to scanning the cross section of each layer with the laser [12]. The mechanical property and processing speed deficiencies of SLS parts are a direct result of the layer-wise heating strategy used to fabricate them.

## 1.2 THE NEED FOR VOLUMETRIC SINTERING

The heat sources in existing commercial PBF systems are classified based on the heating strategy used to fuse the part volume. The laser in SLS is a point-wise heating mechanism where the build area is segmented into a series of vectors that define the laser path, and fusion occurs at a single point in each time instance. Although the velocity of the laser across the powder surface can be as high as 5,000 mm/s in SLS systems, the scanning speed is a limiting factor in the overall processing time [13].

To improve the speed of polymer powder bed fusion, two processes that incorporate line-wise heating strategies were developed. Line-wise heating involves passing an infrared (IR) lamp across the powder bed, and selective fusion is achieved by depositing additives to distinguish the part region from the surrounding powder bed. In selective inhibition sintering (SIS), the part is differentiated from the powder bed by placing a sintering inhibitor such as potassium iodide or sodium hypochlorite in the regions of the powder bed where fusion is not desired [14]. The powder bed is then irradiated with an IR lamp to fuse the entire part surface at each layer. At the end of the build process, the solid part can be separated from the powder bed at the inhibitor interfaces where fusion was prevented during the IR exposure [15]. High speed sintering (HSS) is another PBF process with a line-wise heating strategy. HSS uses an inkjet print head to deposit an infrared-absorbing material to define the part geometry for each layer in the powder bed. Similar to SIS, the surface of the powder bed is then irradiated with an IR lamp, and fusion occurs in the part region where the radiation is more readily absorbed [16]. The line-wise heating methods of SIS and HSS offer processing speed benefits over SLS, but each of the three processes are limited to fusing the part layers individually.

Volumetric powder bed fusion schemes are needed to eliminate the negative effects of layer-wise heating and repeated thermal cycling by applying heat to the entire powder

bed in a single stage. A three dimensional heating strategy could offer additional improvements to the processing speed and efficiency of polymer PBF compared with the point-wise and line-wise methods used in existing commercial systems. A volumetric AM system would also remove the re-solidification and cooling stages that cause internal residual stresses to develop at the layer interfaces in layer-wise heating strategies. Reducing the residual stresses would mitigate the adverse effects of warping and anisotropic mechanical properties associated with layer-wise heating.

Volumetric additive manufacturing approaches have been successfully applied to thermoset photopolymers using a tomographic reconstruction technique [17] [18]. In this method, cross-linking within a resin chamber is initiated by intersecting multiple projections of patterned light. The part is polymerized in a single stage without layers and is the first demonstration of a truly volumetric AM process. However, the materials are restricted to photosensitive thermoset polymers, and the process is incapable of producing parts in thermoplastic polymers. The focus of this dissertation is on the development of a novel volumetric AM process for thermoplastic polymers that delivers energy to the powder bed in the form of RF radiation to fuse the polymer in a single heating stage, thereby enabling more rapid fabrication of parts with potential improvements in mechanical properties.

### **1.3 RESEARCH OBJECTIVES**

#### ***1.3.1 Proposed Radio Frequency Additive Manufacturing System***

The proposed radio frequency additive manufacturing (RFAM) process leverages the insulating properties of thermoplastic powders, which make them relatively transparent to electromagnetic radiation. Insulating polymers can be made electrically conductive through the addition of dopants such as metal powder, carbon black, and graphite [19]. By selectively doping a polymer powder bed with an electrically conductive material and

exposing the powder bed to RF radiation, heat can be generated in the doped regions with little effect on the surrounding powder. The dopant is patterned according to the desired part geometry, and only regions of the powder bed that have received dopant generate sufficient heat to fuse the host polymer. Figure 1.1 details a schematic of the proposed RFAM process.

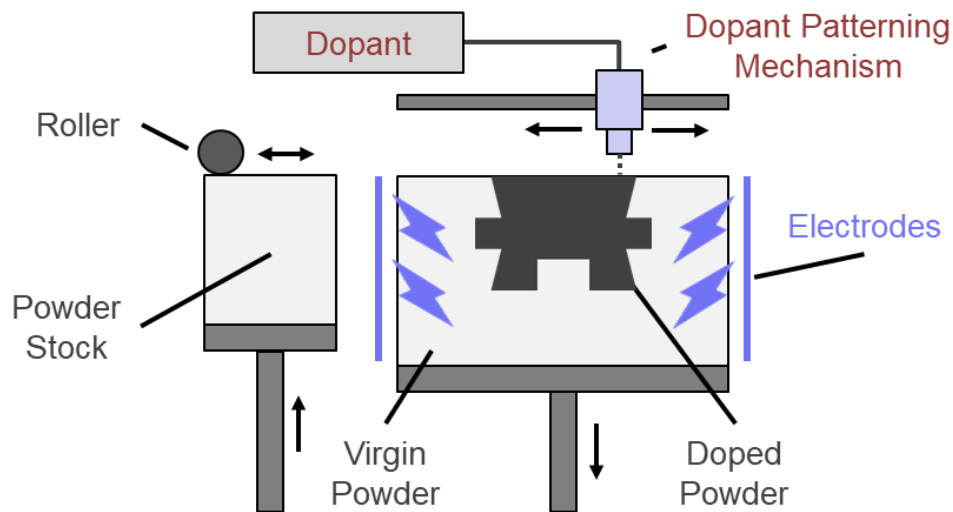


*Figure 1.1 RFAM conceptual design. The dopant is in each layer of the powder bed. Electrodes deliver the electromagnetic energy to the part to fuse the powders together.*

Although the specific architecture of the machine may vary, the RFAM process consists of the following fundamental steps:

1. Raise the powder stock piston to supply a specified volume of virgin powder, and lower the build chamber piston by one layer thickness.
2. Spread the freshly supplied powder across the build surface using a roller or scraper to establish a thin layer of virgin powder that covers the build area.
3. Selectively pattern the electrically conductive dopant to the powder bed according the cross section of the intended geometry.
4. Repeat steps 1-3 until the part geometry has been defined in its entirety by the dopant, resulting in a powder bed consisting of a doped powder region surrounded by un-doped, virgin powder.



5. Subject the powder bed to RF radiation by activating electrodes on opposing faces of the build chamber. Expose the powder bed for a sufficient duration to ensure fusion of the doped region.
6. Allow the powder bed to cool, and remove the fused part from the surrounding powder.

In most RF heating applications, the electrical properties are homogenous throughout the material and independent of the geometry [20] [21]. For RFAM, however, the geometry of the part and the distribution of electrical conductivity throughout the part are created simultaneously, and the process enables spatial tuning of electrical properties throughout the part. The proposed strategy differs from other PBF processes such as SLS, SIS, and HSS by replacing multi-stage, layer-wise energy delivery with a single-stage, volumetric source. By using a single heating and cooling cycle, RFAM will have the potential to improve both part properties and processing time relative to the other methods.

### ***1.3.2 Summary of Research Tasks***

The development of the RFAM process is divided into four research tasks that are addressed in subsequent chapters of this dissertation. The four tasks are summarized in Table 1.1.

*Table 1.1 Summary of research tasks to be addressed in this work*

1	Establish the feasibility of RFAM through electrical property measurements and RF heating experiments
2	Develop computational models to predict heating characteristics and improve heating uniformity
3	Design a mechanism capable of patterning the dopant throughout the powder bed
4	Assess RFAM capabilities, validate the computational models, and generate design rules

The feasibility of the RFAM process (Task 1) is demonstrated in Chapter 3 through electrical property measurements and RF heating experiments on composite mixtures of

polymer and dopant. It is shown that RF radiation can be used as the sole energy source to achieve fusion in the doped powders. Unintended geometric anomalies in the fused parts motivate the computational modelling efforts of Task 2. The focus of Chapter 4, then, is to develop computational models to predict temperature rise during RF heating as well as devise methods for improving the heating uniformity to mitigate the geometric anomalies. Several solutions for improving the heating characteristics for various geometries are proposed and evaluated using the computational models.

Task 3 is addressed in Chapter 5, where two methods for patterning the dopant within the powder bed are defined. The primary requirements for an RFAM system are specified, and the design of a prototype machine capable of depositing the dopant in fixed concentrations is illustrated. Chapter 6 is aimed at evaluating the capabilities and limitations the RFAM system as outlined in Task 4. The computational models developed in Task 2 are validated by fabricating parts in several geometries and implementing the techniques for improving heating uniformity. Lastly, design guidelines are distilled from the experimental results to identify geometric features and part characteristics that are well-suited to the RFAM process.

The next chapter is dedicated to introducing the concept of RF heating and educating the reader on the principles that govern the heating characteristics of different materials. Previous applications of RF heating are presented, and candidate materials for the RFAM process are explored.

## Chapter 2: Radio Frequency Heating Background and Applications

Radio frequency (RF) radiation is considered as a volumetric energy source because it can penetrate into materials, and RF heating refers to the use of RF radiation to generate heat within a material. The degree of heating depends on several factors that will be explained in this chapter. The governing relationships for RF heating will be described as well as the historical applications of RF heating. Lastly, a connection will be made between previous conductive polymer research and RF heating for use in the radio frequency additive manufacturing process.

### 2.1 RADIO FREQUENCY HEATING

#### 2.1.1 Fundamentals of Electromagnetic Heating

RF heating is achieved by transferring electromagnetic (EM) energy into materials. Losses within the materials generate heat in the presence of an EM field. The EM energy takes the form of propagating waves comprised of oscillating electric and magnetic fields. The relationship between the electric field ( $\mathbf{E}$ ), magnetic field ( $\mathbf{B}$ ), charge density ( $\rho_v$ ), and current density ( $\mathbf{J}$ ) are described by Equations 2.1-2.4, also known as Maxwell's equations. Maxwell's equations provide the fundamental basis behind electromagnetic theory, and the governing relationships are useful in solving RF heating problems [22].

$$\textit{Faraday's Law} \quad \nabla \times \mathbf{E} = -\frac{\partial \mathbf{B}}{\partial t} \quad [2.1]$$

$$\textit{Ampere's Law} \quad \nabla \times \mathbf{H} = \mathbf{J} + \frac{\partial \mathbf{D}}{\partial t} \quad [2.2]$$

$$\textit{Gauss' Law} \quad \nabla \cdot \mathbf{D} = \rho_v \quad [2.3]$$

$$\nabla \cdot \mathbf{B} = 0 \quad [2.4]$$

The energy dissipated in RF heating applications can be determined by applying the Poynting Power Theorem (Equation 2.5) and constitutive relationships (Equations 2.6-2.8), where the power loss is a function of the Poynting vector ( $\mathbf{S}$ ), angular frequency of

radiation ( $\omega$ ), electrical conductivity ( $\sigma$ ), permittivity ( $\epsilon$ ), and permeability ( $\mu$ ) of the material.

$$-\nabla \cdot \mathbf{S} = \mathbf{J} \cdot \mathbf{E} + j\omega \mathbf{D} \cdot \mathbf{E} + j\omega \mathbf{B} \cdot \mathbf{H} \quad [2.5]$$

$$\mathbf{J} = \sigma \mathbf{E} \quad [2.6]$$

$$\mathbf{D} = \epsilon \mathbf{E} \quad [2.7]$$

$$\mathbf{B} = \mu \mathbf{H} \quad [2.8]$$

The electromagnetic spectrum is used to classify waves based on their frequency and corresponding wavelength, as depicted in Figure 2.1 [23]. The EM spectrum spans many orders of magnitude in frequency, with gamma rays comprising the highest frequency and RF waves making up the lowest. There is an inverse relationship between frequency and wavelength, so the lower frequency radio waves are also the longest. RF occupies the frequency range between 3 kHz and 300 MHz, and frequencies between 300 MHz and 300 GHz are considered microwaves [24]. The Federal Communications Commission designates specific bands within the EM spectrum for use in Industrial, Scientific, and Medical (ISM) applications. According to the ISM allocations, the allowable frequencies for RF applications are 6.78 MHz, 13.56 MHz, 27.12 MHz, and 40.68 MHz, while the frequencies designated for microwave applications are 915 MHz and 2.45 GHz for microwave applications [25].

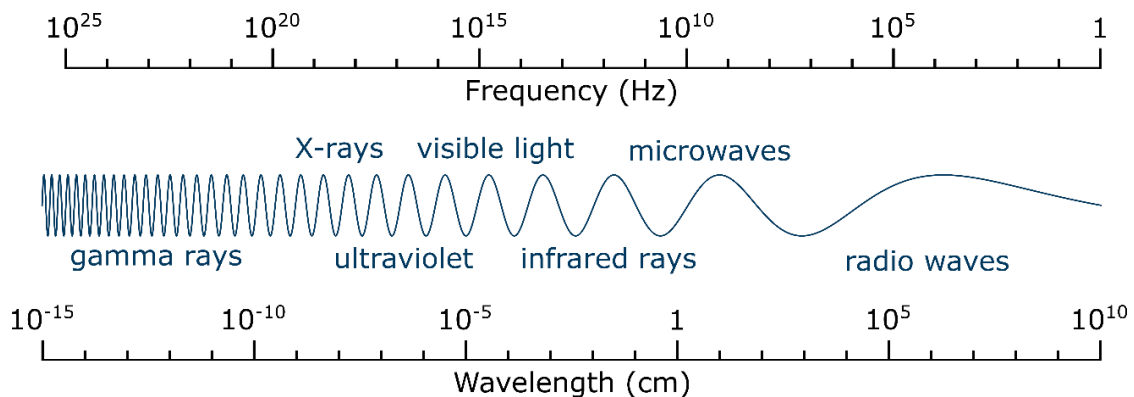


**Figure 2.1** The electromagnetic spectrum comparing the frequency and wavelength for various recognized bands. Adapted from [23]

RF heating differs from conduction-based heating methods such as ovens and lamps in that heating occurs simultaneously throughout the entire material volume. As a volumetric energy source, RF heating can be an effective method in materials with poor thermal conductivity, high density, or high specific heat [26]. RF heating can offer greater energy-efficiency and require less time than conduction-based heating processes [24] [27]. RF radiation also provides greater control than other methods because the heat source can be switched on and off instantaneously [24].

RF and microwave heating are also known as dielectric heating. Dielectrics are insulating materials that can both store and dissipate electrical energy [28]. The degree to which dielectrics heat depends on several factors. The Poynting Power Theorem can be used to derive the relationship shown in Equation 2.9, where the power dissipation per unit volume depends on the frequency of radiation ( $\omega$ ), the permittivity of free space ( $\epsilon_0 = 8.85 \times 10^{-12}$  F/m), the effective loss factor of the material ( $\epsilon''_{eff}$ ), and the developed electric field within the material ( $E_{rms}$ ) [29].

$$P = \omega \epsilon''_{eff} \epsilon_0 E_{rms}^2 \quad [2.9]$$

The loss factor is part of an intrinsic material property called permittivity, which describes how energy is stored and dissipated in the presence of an electric field. Permittivity is a complex quantity (Equation 2.10) where the real part ( $\epsilon'$ ) is a measure of storage capacity, and the imaginary part ( $\epsilon''$ ) relates to energy loss.

$$\epsilon^* = \epsilon' - j\epsilon''_{eff} \quad [2.10]$$

Permittivity reflects the extent to which the molecules within a material polarize in an electric field. For a lossless medium, the permittivity consists only of the real component, and energy is stored as the molecules realign from their equilibrium position to oppose the electric field. Real dielectrics have a complex permittivity to account for losses. There are two primary mechanisms for dielectric loss. Losses can arise due to

polarization effects of bound charges and ohmic conduction of free charges. Together, the two mechanisms comprise the effective loss factor of the material:

$$\varepsilon_{eff}'' = \varepsilon'' + \frac{\sigma}{\omega\varepsilon_0} \quad [2.11]$$

The first term in Equation 2.11 ( $\varepsilon''$ ) accounts for losses associated with the polarization of bound charges in a time-varying electric field and depends on the radiation frequency. As the frequency increases, the rotation of dipoles in the material begin to lag the electric field, resulting in loss. The specific mechanisms of polarization losses are often difficult to distinguish but can be in the form of dipolar, electronic, atomic, and interfacial losses within the material at a specific frequency [24] [29] [30]. The second term in Equation 2.7 corresponds to losses incurred as a result of ohmic conduction of free charges. Ohmic conduction depends on the electrical conductivity ( $\sigma$ ) of the material which is a measure of the density of free charges as well as their mobility [22]. The movement of free charges in the presence of an electric field causes a current flow which in turn gives rise to losses and heating.

Considering electrical conductivity is defined as a material's ability to allow current flow, it may not be intuitive that conductivity contributes to loss. Electrical conductivity and loss can be explained through elementary circuit theory and extended to the case of electromagnetic fields. Electrical conductivity is inversely proportional to resistance, so it will be shown that decreasing the resistance (increasing the electrical conductivity) in a simple circuit leads to greater power dissipation. Ohm's law states that voltage is the product of current and resistance (Equation 2.12), and the power dissipated across a resistor is given by Equation 2.13 [22]. In the first case ( $I^2R$ ), power dissipation rises linearly with resistance, but with the square of current. By definition, electrical resistance is the opposition to current flow, so an increase in resistance necessarily leads to a decrease in

current and thus power dissipation. The relationship is clearer in the second case ( $V^2/R$ ) where power is inversely proportional to the resistance.

$$V = IR \quad [2.12]$$

$$P = I^2R = \frac{V^2}{R} \quad [2.13]$$

Equation 2.13 shows that decreasing the resistance leads to greater power dissipation. The effect is limited in real circuits, however, where reducing the resistance causes a reduction in the voltage drop across the resistor. Figure 2.2 shows a simple circuit consisting of a voltage source ( $V_S$ ), source resistance ( $R_S$ ), and load resistance ( $R_L$ ).

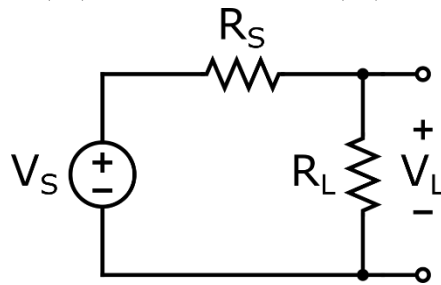


**Figure 2.2** Circuit representation of a source and load. The source includes a voltage ( $V_S$ ) as well as a resistance ( $R_S$ ). Power dissipation across the load ( $R_L$ ) is determined by the voltage drop across it ( $V_L$ ).

From elementary circuit theory, the source voltage is divided between the source resistor and load resistor. If the load resistance were reduced to zero, there would be no voltage drop across the load resistor ( $V_L$ ) and no power dissipation. In general, the maximum power transfer to the load occurs when the load resistance matches the source resistance. The relationship between voltage drop and power across the load resistor as a function of load resistance is given in Figure 2.3, showing maximum power transfer when the ratio between the load and source resistors is equal to one.

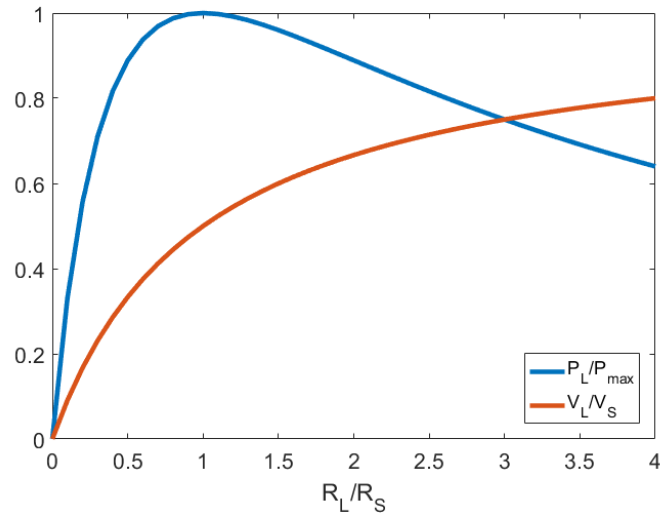


**Figure 2.3** Normalized voltage across the load compared to the source voltage ( $V_L/V_S$ ) and normalized power dissipated across the load compared to its maximum ( $P_L/P_{max}$ ).

The circuit analogy can be extended to electromagnetic fields. In the circuit example, decreasing the resistance led to an increase in power dissipation but was limited by the voltage drop across the resistor in a real circuit. Considering the point form of Ohm's law for electromagnetic fields in Equation 2.6, higher electrical conductivity gives rise to higher current density ( $\mathbf{J}$ ), measured in amps per square meter [22].

For a given electric field strength within a material, the power dissipated increases with increasing conductivity in the same way that power in the circuit increases with decreasing resistance. Therefore, electrical conductivity can be considered as part of a material's loss factor, but increasing the electrical conductivity does not improve heating *ad infinitum*. Just as decreasing the resistance of the load led to a reduction in the voltage drop in the circuit analogy, an increase in the electrical conductivity leads to smaller internal electric fields. In real systems, the properties of the load must be matched to the properties of the source, and heat generation is governed by the tradeoff between increasing the electrical conductivity and the corresponding reduction in the electrical field strength within the body.



In practice, radio frequency heating equipment consists of a generator and an applicator. The generator is used to supply the time-varying voltage, and the applicator directs the EM energy to the material. The applicator for electric field heating at RF frequencies generally consists of two parallel plate electrodes. Maxwell's equations show that a time-varying electric field induces a magnetic field. However, when the radiation wavelength is much larger than the dimensions of the applicator, the system is considered quasistatic, and the magnetic field contributions to heating can be ignored [31] [32]. Lossy dielectrics are heated by placing them between the applicator plates where the electric field is concentrated.

### **2.1.2 Impact of Radiation Frequency**

In designing a system to volumetrically fuse doped polymer samples, the frequency of radiation is a critical consideration. As an electromagnetic wave encounters a material, the energy of the wave diminishes as it is lost in the form of heat to the material. In dielectric heating applications, it is useful to consider the penetration depth of the radiation. Penetration depth is defined as the distance from the surface of a material at which the power of the wave is diminished to  $1/e$  (37%) of its original value. The penetration depth ( $\delta_p$ ) for lossy materials is given by Equation 2.14 [29]. The penetration depth is inversely dependent on the frequency of radiation ( $\omega$ ), the permeability of free space ( $\mu_0=1.26 \times 10^{-6}$  H/m), and the effective electrical conductivity within the media ( $\sigma_{eff}$ ).

$$\delta_p = \frac{1}{2} \sqrt{\frac{2}{\omega \mu_0 \sigma_{eff}}} \quad [2.14]$$

Using Equation 2.11, it can be shown that RF radiation at 27.12 MHz penetrates nearly ten times deeper than microwaves at 2.54 GHz. As the frequency is further increased into the infrared range, the penetration drops even further. Infrared is often considered to be a surface heating mechanism instead of volumetric because the penetration depths are

so small [33]. The goal of this work is to produce centimeter-scale parts, so RF is the preferred frequency due to the greater penetration depth into the samples.

The increased wavelength of RF radiation over microwave offers additional benefits in the design of the applicator. Using the principles of transmission line theory, Figure 2.4 shows a transmission line formed by two parallel plate electrodes with the electromagnetic wave propagating between them. As the incident wave encounters the end of the electrodes, the open circuit condition causes the wave to be reflected and propagate in the opposite direction. The superposition of the forward and backward propagating waves creates a standing wave in the electric field between the electrodes. At each half wavelength, nodes occur as a result of the standing wave effect, and the electric field is zero for all time instances [34]. The standing wave effect causes a non-uniform electric field within the applicator, and no heating occurs at the nodal sites where the electric field vanishes.

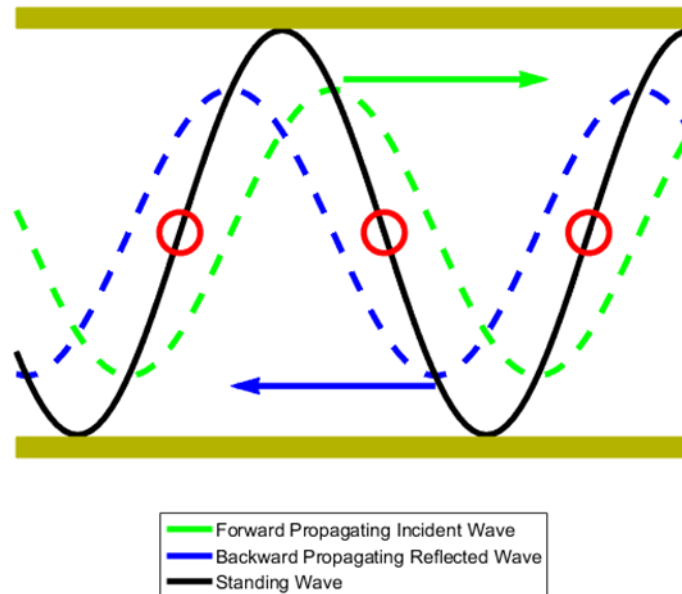


**Figure 2.4** Standing wave formed by the superposition of a forward propagating electric field (green) and a backward propagating reflected electric field (blue). The standing wave creates nodal locations (circled in red) where the electric field remains at zero for all time instances.

The size of the applicator (electrodes) relative to the radiation wavelength is known as the electrical size. Greater electric field uniformity can be achieved by using an electrically small applicator having dimensions that are one eighth of the wavelength or smaller. The wavelength of a 27.12 MHz RF wave is 11.06 m. To be classified as electrically small, the electrode dimensions must not exceed 1.38 m. On the other hand, microwaves at 2.54 GHz have a wavelength of 0.12 m and the applicator must be smaller than 1.5 cm to be considered electrically small. Household microwave ovens are electrically large multimode cavities, and highly variable electric fields are generated within them [35]. Although the heating uniformity can depend on the geometry of the load, standing waves within the microwave cavities can contribute to local hot and cold zones, and turntables are often implemented to improve heating uniformity by rotating the food through each of the zones. RF radiation offers the potential to heat larger parts with greater uniformity in the applied electric field than microwaves because of the longer wavelength of RF radiation. From the perspective of penetration depth and the formation of standing waves within the applicator, RF radiation is preferred over microwave radiation for the RFAM process.

## **2.2 RF HEATING APPLICATIONS**

### ***2.2.1 History of RF Heating***

The use of high frequency radiation in heating applications began in the late 19<sup>th</sup> century with independent experiments conducted by Jacques-Arsène d'Arsonval and Nicola Tesla that explored the effects of rapidly alternating electrical currents [36]. In 1893, d'Arsonval discovered that electric shocks supplied at frequencies above 5 kHz no longer produced muscle contraction and large electric currents could pass through the body without being felt [37]. Experiments by Nagelschmidt in 1907 demonstrated the medical potential for high frequency radiation when it was observed that currents could penetrate

deep into tissues, and the process was given the name “diathermy” [38]. In 1908, high frequency radiation was used to treat rheumatism and rheumatic arthritis [36].

Diathermy grew in popularity in the United States after World War I from an increased demand for physical therapy. Research continued through the 1920’s, where the attention shifted to higher frequency (and thus shorter wavelengths) of electromagnetic energy. With the introduction of wavelengths below 30 m, the field of diathermy was branched into two categories: long-wave diathermy for frequencies below 1 MHz and short-wave diathermy for frequencies between 10 and 100 MHz. Long-wave diathermy required the electrodes to be in direct contact with the tissue for heating to occur, while short-wave diathermy enabled contactless heating and was generally more convenient and safer [39]. It was for this reason that short-wave diathermy emerged as the preferred electrotherapy method. Depending on the application, different electrode configurations such as parallel plate and drum applicators could be used to target different tissues [40].

In addition to its use in the medical industry, RF heating began to gain traction in the food industry during and after World War II. The development of radio communication systems during the war led to an interest in measuring the dielectric properties of various materials [41]. By the mid 1940’s, RF was being considered for defrosting frozen foods [42], blanching vegetables [43], and rapid food cooking [44] [45]. The initial draw to RF was that food could be treated in its packaging to reduce handling contamination [46] [47]. With the commercial success of the microwave oven, RF heating in food processing declined during the latter half of the 20<sup>th</sup> century [41]. However, new applications for RF have been studied in recent years. In the food industry, RF has been used extensively to disinfect nuts [48] [49] [50] and grains [51] [52] [53] against insects and has also achieved success as a pasteurization method [54] [55]. RF heating has been shown to be effective as a post treatment process for baked goods [56] [57] and as a drying method for macadamia

nuts [58] and wood [59]. Numerous industries have benefitted from the utility of RF heating, and new applications of the technology continue to emerge.

### ***2.2.2 Potential Challenges***

Temperature prediction and heating uniformity are the greatest potential challenges when considering RF radiation in the application of a volumetric additive manufacturing process. Analytical solutions to RF heating problems are often too complex to calculate and require numerical approaches and finite element analyses to solve [31]. Though RF radiation offers greater heating uniformity than microwaves, non-uniform heating can still occur. Uneven heating can arise from the physical properties of the material such as the geometric, electrical, and thermal attributes as well as the properties of the RF system including the electrode spacing and engineering design of the apparatus [60]. Non-uniform heating for RF applications has been studied extensively through simulation and experimentation, and several attempts have been made to improve the uniformity by rotating the sample [61] [62], rounding corners [63], pulsing the energy input [64], and artificially thickening the cold regions [65]. Most of the research in this area has been applied to foods or products with predefined material properties, and the effect of locally tuning dielectric properties has received little attention [66].

## **2.3 ELECTRICALLY CONDUCTIVE POLYMER COMPOSITES**

### ***2.3.1 Applications of Electrically Conductive Polymer Composites***

Radio frequency additive manufacturing relies on mixing an electrical insulator with a conductor to achieve the necessary electrical properties suitable for RF heating. Most polymers are intrinsically non-conductive and resist the flow of electrical energy. Insulating polymers can be made electrically conductive through the addition of dopants such as metal powder, carbon black, and graphite [67]. In recent years, conductive polymer

research has been instrumental in the creation of antistatic components [68], wearable electronics [69] [70], and RFID tags [71].

The use of conductive composites in dielectric heating applications is limited, but vulcanizing rubber using microwaves achieved commercial success in the 1960's. Extruded rubber was treated with microwaves in a continuous industrial process to improve the efficiency of the vulcanization process [72]. Though polar forms of rubber could be treated without additives, the addition of carbon black enabled non-polar rubber to heat in the microwaves as well as enhanced the tensile strength. The improved microwave coupling and tensile strength resulting from the addition of carbon black led to the industrial success of the process [73]. The use of additives in composites to improve microwave heating has also been demonstrated by reducing the curing time of carbon black doped silicones [74]. RFAM seeks to extend the principles of dielectric heating of doped composites to achieve volumetric fusion of the host matrix.

### ***2.3.2 Percolation Limit in Electrically Conductive Composites***

Electrically conductive composites exhibit a well-known and well-documented behavior known as percolation. Percolation occurs when conduction pathways form in composites containing electrically conductive additives. When the volume concentration of the additive is low, electron transfer is prohibited by the insulating matrix material. Although the particles themselves are conductive, physical separation prevents the flow of electric current. As the volume fraction is increased, physical contact between particles causes the formation of conductive networks, and a sharp rise in the electrical conductivity of the composite is observed [75]. The volume fraction at which the composite transitions from an insulator to a conductor is known as the percolation limit or threshold. The percolation threshold of polymer composites can be affected by the properties of the dopant as well as the polymer. The packing pressure, geometry, porosity, and distribution of the

dopant filler can influence the percolation limit [76]. It has also been shown that the polarity, viscosity, and crystallinity of the polymer matrix have an effect on the volume fraction of filler necessary to achieve percolation [20] [77]. Percolation is an important parameter in the design of conductive composites because it represents the minimum dopant concentration necessary to achieve electrical conduction.

The percolation threshold for polymer and carbon black composites can vary between 3 and 20% carbon black by weight depending on how the mixtures were processed [19] [78]. Large volume fractions of filler can lead to reductions in the mechanical properties of the composite and increase the cost. Efforts to reduce the percolation threshold in composites has been widely studied in the literature. Hybrid dopants of carbon black and multi-walled carbon nanotubes have been shown to reduce the percolation threshold and improve mechanical properties [79] [80]. Carbon black and graphite fillers have also been studied, but the addition of the graphite had a negative effect on the flexural strength of the composite [81]. Chemical matching of the polymer matrix to lower the percolation threshold has also been demonstrated [82].

### ***2.3.3 Candidate Materials for RFAM***

The goal of this work is to present a new application of conductive polymers to RF heating. The materials used for the polymer matrix and conductive dopant are of critical importance, as their properties determine the degree of RF heating in the composite. Two candidate materials have been identified for the RFAM process. Graphite is used for the dopant, and the polymer is polyamide (nylon) 12.

Graphite is known to be a good conductor of electricity, and its electrical properties can be explained by its atomic structure. Graphite is an arrangement of tightly bonded hexagonal sheets of carbon atoms that are weakly bonded to each other, as depicted in Figure 2.5.

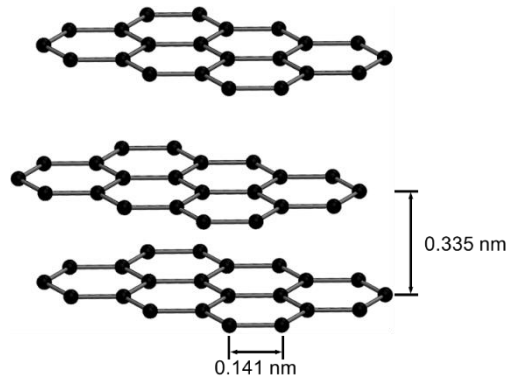


**Figure 2.5** Graphite structure adapted from [83]. Graphite is made up of carbon sheets and held together through weak Van der Waals forces.

The carbon atoms in graphite have a hybridized  $sp^2$  orbital structure in which each carbon atom is bonded to three other carbon atoms through strong sigma bonds leaving a single delocalized valence electron [84]. The orbital of the delocalized electron is oriented perpendicular to the layer plane, and bonding between layers is achieved through weak Van der Waals forces [83]. The layered structure of graphite accounts for anisotropic electrical properties. Electron movement is relatively unimpeded in the plane of the layers, but movement across layers is almost entirely restricted. The high conductivity along layer planes results from overlapping valence and conduction bands. For this reason, graphite is considered a semimetal although it contains no metallic elements [85]. The electrical conductivity of graphite powder depends on the particle morphology and the direction of measurement, but typical values are in the range of 10,000 to 50,000 S/m [86]. In addition to its electrical properties, graphite is inexpensive and safe to handle, making it a good candidate for the doping material in RFAM.

In contrast, polyamide 12 (PA 12 or nylon 12) is an insulating polymer that is suitable for the matrix in RFAM. Nylon 12 is a semicrystalline thermoplastic polymer that is named for the twelve carbon atoms present in its chemical structure, shown in Figure 2.6



[87]. Compared to other polyamides, nylon 12 is notable for its low moisture absorption, low melting point, and resistance to stress cracking. Like most polymers, nylon 12 is a good electrical insulator due to the large energy gap between the valence and conduction bands. Nylon 12 has an electrical conductivity of  $10^{-13}$  S/m and dielectric loss factor in the range of 0.03-0.09, making it nearly transparent to electromagnetic energy [88] [89] [90]. In the context of radio frequency additive manufacturing, electromagnetic transparency of the polymer is necessary to concentrate heat generation on the doped regions without heating the surrounding powder bed. The thermal insulating characteristics of nylon 12 also serve to confine the heating within the powder bed and limit unintended thermal conduction.

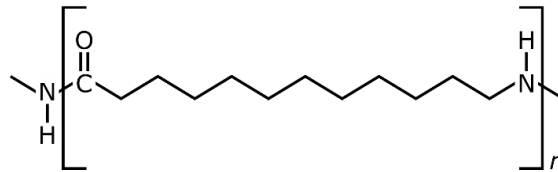


**Figure 2.6** Chemical structure for nylon 12 adapted from [87]. Each vertex represents individual  $CH_2$  groups.

The widespread use and availability of nylon 12 powder provides further support for its application in RFAM. Nylon has a long history in additive manufacturing and is commonly used in the selective laser sintering (SLS) process [91]. As a result, the sintering properties of nylon 12 powders are well-established, and the powders are readily available from a number of suppliers [92] [93] [94]. RFAM relies on the introduction of an electrically conductive dopant to an insulating polymer such that sufficient heating is achieved to locally fuse the polymer. The vast difference in electrical properties between graphite and nylon 12 make them suitable candidate materials for RFAM in which the effective properties of the composite dictate the amount of heating that can be attained.

## **2.4 CLOSURE**

In this chapter, the relationships that govern RF heating were discussed, and the historical background and use of RF heating was presented. Towards the development of a radio frequency additive manufacturing process, the properties of electrically conductive polymer composites were explored through previous studies in literature. Microwave and RF radiation have been used in the treatment of doped rubbers and silicones, but the use of RF radiation as the sole energy source to melt the polymers has not been demonstrated. In additive manufacturing, the selective heating of doped powder beds has been shown in the high speed sintering process, but volumetric heating through deeply penetrating RF radiation has not been demonstrated. In the next chapter, the electrical properties of nylon 12 and graphite powder mixtures are measured, and RF heating experiments are conducted in which selective fusion of the powders is achieved.

## **Chapter 3: Electrical Property Measurement and Radio Frequency Heating of Graphite-Doped Polyamide (Nylon) 12**

The previous chapter introduced RF heating and explained the various factors that contribute to power loss when materials are subjected to electromagnetic radiation. The electrical properties of the material have a significant effect on the degree of heating that can be achieved in RF heating applications. In the case of radio frequency additive manufacturing, the polymer must be heated beyond its melting temperature. This chapter focuses on electrical property measurements of nylon 12 and graphite mixtures, and an RFAM proof-of-concept demonstration is shown by selectively fusing the doped powders.

### **3.1 PERMITTIVITY MEASUREMENTS OF GRAPHITE-DOPED NYLON 12 POWDERS**

#### ***3.1.1 Graphite-Doped Nylon 12 Composites***

The electrical properties of insulating polymers can be enhanced through the addition of conductive dopants. Nylon 12 and graphite were identified as potential candidate materials for the polymer and dopant, respectively, based on the large difference in their electrical properties. This chapter focuses on the dielectric property measurement and RF heating of nylon 12 and graphite mixtures to determine the critical graphite content necessary to achieve fusion of the polymer. The feasibility of the radio frequency additive manufacturing process is established through successful fusion of the polymer using RF radiation as the sole energy source.

The nylon 12 and graphite were available as dry powders. The supplier of the nylon powder was Arkema, and the mean particle diameter was 42  $\mu\text{m}$  [95]. The graphite powder was supplied by Loud Wolf, and the mean particle size was 44  $\mu\text{m}$  with 99.9% purity. To determine the ideal nylon/graphite composition, mixtures of varying graphite contents were created. The graphite concentration was varied between 10 and 60% graphite by

weight, and the samples were hand mixed in a rigid container to evenly distribute the graphite.

### 3.1.2 Impedance Spectroscopy to Measure Dielectric Properties

Impedance spectroscopy was used to measure the electrical properties of the composite powder mixtures. In RF heating applications, the degree of heat generation is governed by the complex permittivity of the material which can be evaluated according to the material's impedance. The complex relative permittivity is comprised of two parts and is a function of frequency,  $\omega$  (rad/s), and the permittivity of free space,  $\epsilon_0$  (F/m). The real part is called the relative permittivity ( $\epsilon'_r$ ) and is a measure of the material's ability to polarize in an electric field to store charge. The effective electrical conductivity ( $\sigma_{eff}$ ) includes the imaginary component ( $\epsilon''_r$ ) and is a measure of the electric field losses in the material.

$$\epsilon = \epsilon'_r \epsilon_0 - j \frac{\sigma_{eff}}{\omega} = \epsilon'_r \epsilon_0 - j \left( \epsilon''_r \epsilon_0 + \frac{\sigma}{\omega} \right) \quad [3.1]$$

At RF frequencies, the conductivity losses,  $\sigma$  (translational motion of free charge), dominate the dielectric relaxation losses,  $\epsilon''_r$  (rotational and vibrational motion of bound charge). The impedance measurements were conducted using an HP 4194A Impedance Analyzer with frequency sweep capabilities. The mixtures were placed in a coaxial chamber and the impedance of the chamber and sample were measured using a frequency sweep from 40 kHz to 40 MHz. Figure 3.1 provides a schematic of the coaxial fixture with critical dimensions labeled. To avoid fringing field effects at the upper surface of the central electrode, the sample was partially filled only to a depth,  $h$ , in the chamber. Partially filling the chamber ensured a tangential  $\mathbf{E}$ -field boundary condition at the surface of the mixture during the measurements.

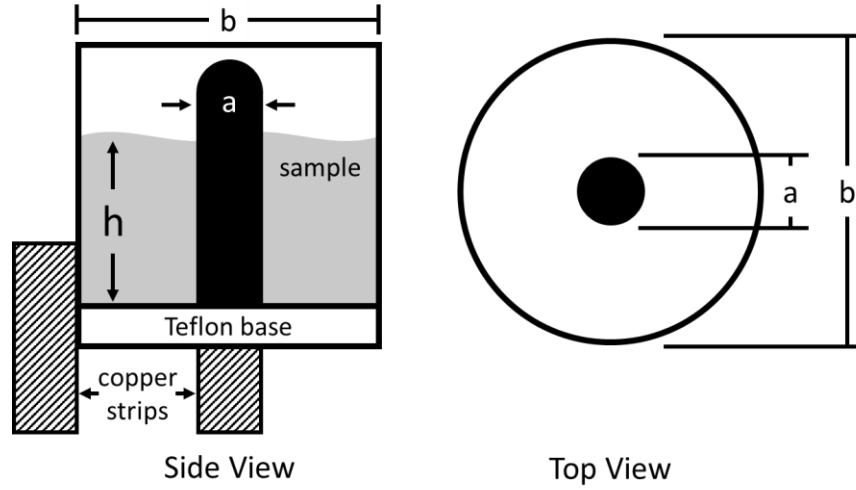


**Figure 3.1** Diagram of the coaxial chamber used for impedance measurement. The diameter of the inner electrode ( $a$ ) was 1.59 cm, and the diameter of the outer electrode ( $b$ ) was 7.94 cm. The powder was held in place by a Teflon block that separated the two electrodes. Copper strips soldered to the electrodes provided connection to the input terminals of the impedance analyzer.

The impedance analyzer measured the total complex impedance,  $Z_{meas}$ , of the fixture and sample at each frequency:

$$Z_{meas} = R_{meas} + jX_{meas} \quad [3.2]$$

where  $R_{meas}$  and  $X_{meas}$  are the measured resistance and reactance, respectively, and reactance is a function of angular frequency,  $\omega$ , inductance,  $L$ , and capacitance,  $C$ :

$$X_L = \omega L \quad [3.3]$$

$$X_C = -\frac{1}{\omega C} \quad [3.4]$$

To determine the properties of the sample alone, the parasitic resistance ( $R_{fix}$ ), inductance ( $L_{fix}$ ), and capacitance ( $C_{fix}$ ) from the fixture were removed in addition to the capacitance of the air displaced by the sample within the coaxial chamber ( $C_{air}$ ). Figure 3.2 shows an equivalent circuit of the fixture in which  $C_{mat}$  and  $R_{mat}$  are the capacitance and resistance of the material and  $Z_{meas}$  corresponds to the uncorrected, measured impedance. The

characteristic resistance, inductance, and capacitance of the coaxial fixture were measured to be 3.06  $\Omega$ , 119 nH, and 5.22 pF, respectively.

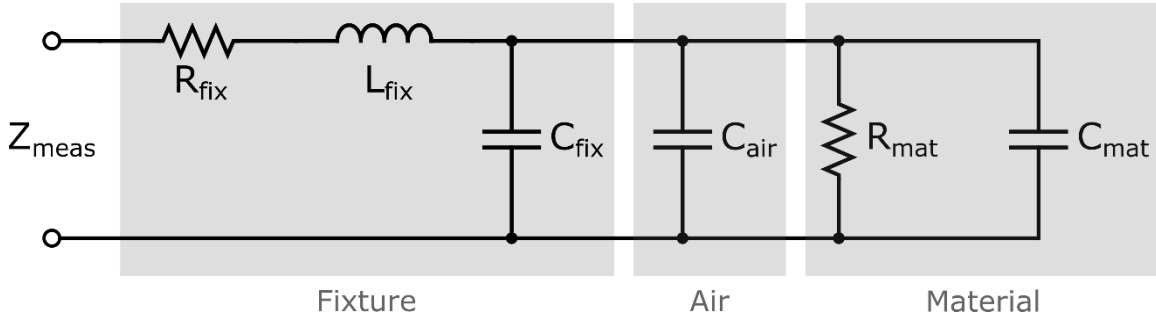


**Figure 3.2** Circuit diagram for the impedance measurements. The parasitic  $R$ ,  $L$ , and  $C$  components of the fixture must be removed from the measured impedance to determine the complex capacitance of the material.

The series fixture resistance and inductance were removed according to Equation 5, and the remaining quantity represents the impedance of the material and air within the chamber. The materials do not contribute to inductive measurements owing to the absence of a physical mechanism for storing magnetic field energy.

$$Z_{mat+air} = (R_{meas} - R_{fix}) + j(X_{meas} - \omega L_{fix}) = R_{mat+air} + jX_{mat+air} \quad [3.5]$$

Next, the impedance measurements were converted to admittance by taking the complex reciprocal. Admittance is also a complex quantity composed of the conductance ( $G$ ) and susceptance ( $B$ ). The conversion from impedance to admittance allows the parallel capacitance of the fixture and displaced air to be removed more readily through the susceptance.

$$Y_{air+mat} = \frac{1}{Z_{air+mat}} = G_{air+mat} + jB_{air+mat} \quad [3.6]$$

The relative permittivity of air is approximately one, and thus the capacitance of the air displaced is represented by the geometry of the chamber with inner and outer electrode diameters,  $a$  and  $b$ , the sample depth,  $h$ , and the permittivity of free space,  $\epsilon_0$ .

$$C_{air} = \frac{2\pi\epsilon_0 h}{\ln(b/a)} \quad [3.7]$$

The complex admittance of the material was then determined by removing the capacitance of the fixture and displaced air from the susceptance. The conductance of the air in the fixture ( $G_{air}$ ) was assumed to be negligible.

$$B = \omega C \quad [3.8]$$

$$Y_{mat} = G_{air+mat} + j[B_{air+mat} - \omega(C_{fix} - C_{air})] = G_{mat} + jB_{mat} \quad [3.9]$$

With all relevant parasitic properties removed, the capacitance of the material could be determined through the susceptance and frequency.

$$C_{mat} = \frac{B_{mat}}{\omega} \quad [3.10]$$

The effective electrical conductivity ( $\sigma_{eff}$ ) and the relative permittivity ( $\epsilon'_r$ ) were estimated from the complex capacitance as follows:

$$\sigma_{eff}(\omega) = \frac{G_{mat}(\omega)\ln(b/a)}{2\pi h} \quad [3.11]$$

$$\epsilon'_r(\omega) = \frac{C_{mat}(\omega)\ln(b/a)}{2\pi\epsilon_0 h} \quad [3.12]$$

Although the parallel resistance of the material does not appear directly in the conductivity calculation, it was taken into account implicitly through the conversion of impedance to admittance. It is important to note that the capacitive susceptance is a function of frequency, so the electrical properties are evaluated at a specific frequency, which was 27.12 MHz in this case.

### 3.1.3 *Electrical Properties of Graphite-Doped Nylon 12 Mixtures*

The effective electrical conductivity defined in Equation 3.11 represents the total loss factor of the material at a given frequency but does not provide information about the type of losses that are present. Electrical losses in time-varying fields are comprised of

conductive (translational) and polarization (rotational and vibrational) components. Although the specific form of loss does not influence the RF heating characteristics of the material, identifying the loss mechanisms can explain the behavior of the nylon/graphite composites as the graphite composition is increased. The frequency response of the electrical conductivity at a given graphite loading can be used to distinguish the conductive ( $\sigma$ ) losses from the losses due to polarization ( $\epsilon''$ ). Figure 3.3 gives the effective electrical conductivity as a function of frequency for the nylon mixture containing 30% graphite by weight.

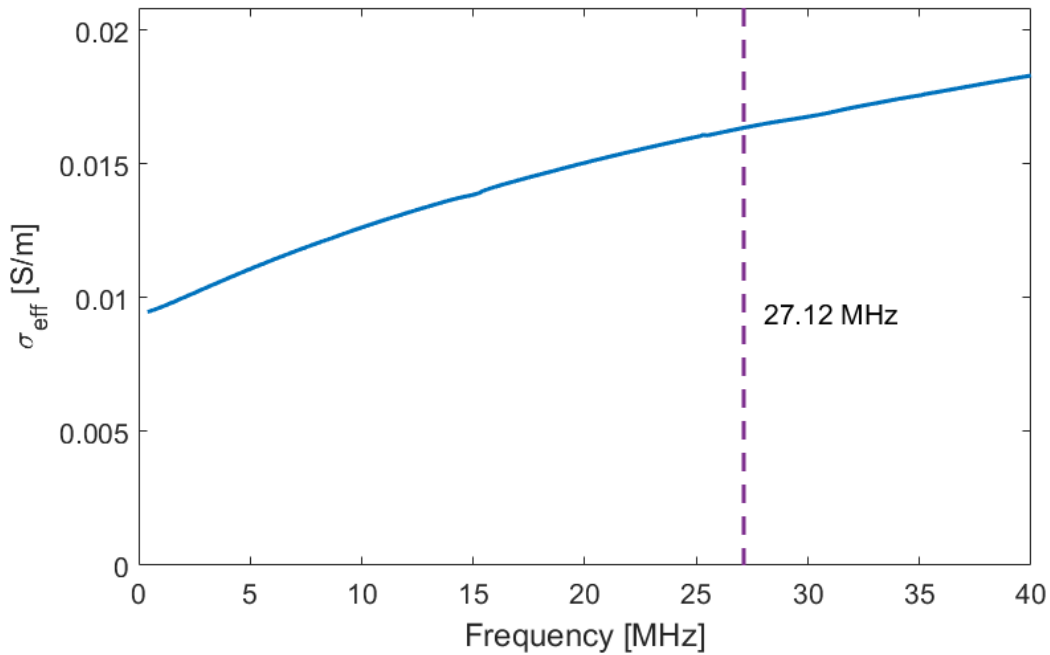


**Figure 3.3** Effective electrical conductivity vs. frequency for 30% graphite by weight

Rearranging the effective loss factor in Equation 2.7, the effective electrical conductivity can be expressed as a function of frequency. The conductivity term ( $\sigma$ ) on the right side of Equation 3.13 is called the DC conductivity because it typically does not have a frequency dependence. The effective electrical conductivity is sometimes referred to as the AC conductivity to include the frequency dependent polarization term ( $\epsilon''$ ).



$$\sigma_{eff} = 2\pi f \epsilon_0 \epsilon'' + \sigma \quad [3.13]$$

Equation 3.13 describes a line in which the y-intercept corresponds to the DC conductivity, and the slope is related to the polarization losses. A linear regression on the electrical conductivity data in Figure 3.3, then, can provide a comparative estimate of the sources of loss in the material. The linear regression on the 30% mixture data gives an  $R^2$  correlation of 0.98 and DC conductivity of 0.0103 S/m. At the design frequency of 27.12 MHz, the total effective electrical conductivity is 0.0161 S/m. An estimate of the polarization loss can be determined by subtracting the DC conductivity (0.0103 S/m) from the total effective conductivity (0.0161 S/m) at 27.12 MHz. The relative proportion of each loss mechanism is found by dividing the DC conductivity and polarization loss by the total conductivity. By this estimate, 36% of the loss is due to polarization effects while the remaining 64% can be attributed to electrical conduction.

The effective electrical conductivity as a function of frequency for mixtures containing between 10% and 60% graphite by weight is shown in Figure 3.4. In general, the effective electrical conductivity increases with frequency due to the combination of conductive and polarization losses. However, at graphite concentrations that are 40% by weight and higher, the conductivity decreases with increasing frequency.

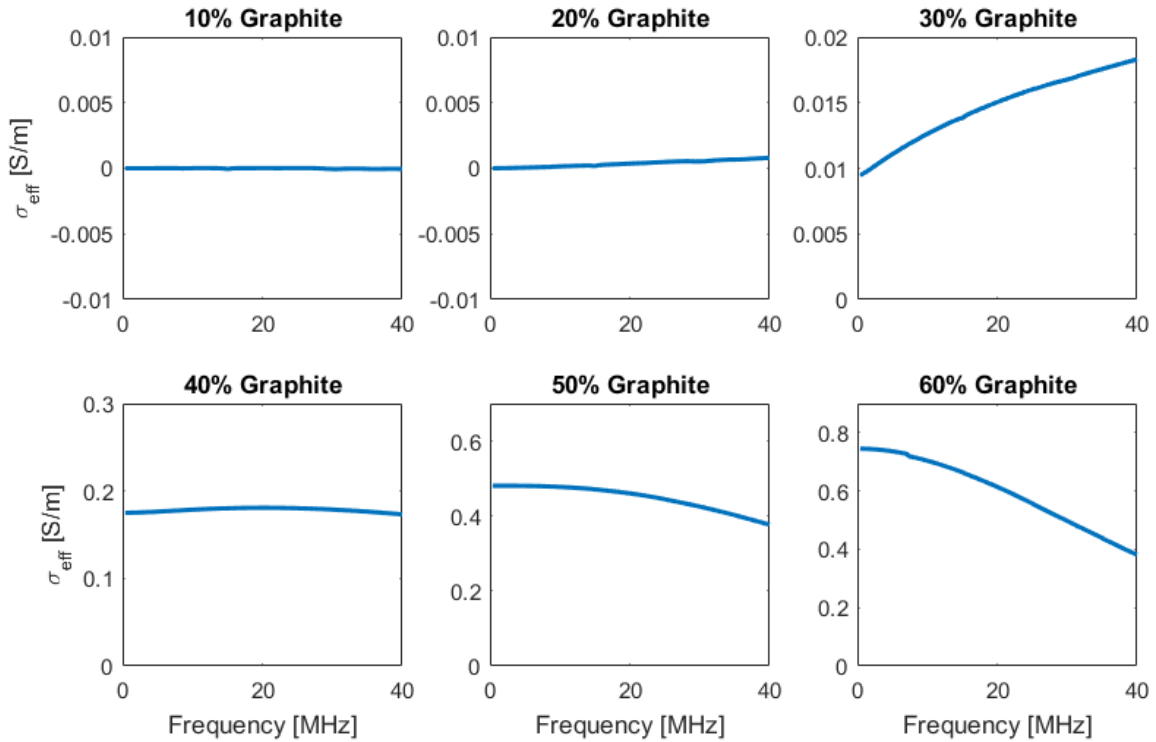


**Figure 3.4** Effective electrical conductivity vs. frequency for nylon/graphite mixtures containing between 10% and 60% graphite by weight.

From the conductivity data, it appears that both polarization and conductive losses contribute to the total conductivity of the nylon and graphite mixtures. In filler-matrix composites, the dominant polarization loss mechanism is Maxwell-Wagner interfacial loss where free charges accumulate at the particle interfaces [96]. The conduction losses in conductive composites can also arise from interfacial effects that are similar to Maxwell-Wagner [97]. As the frequency is increased, the charge flux is limited by the drift velocity of the electrons within the graphite which constitutes a loss mechanism and contributes to heating.

The effective electrical conductivity at 27.12 MHz as a function of graphite content is given in Figure 3.5. The results suggest the percolation limit for the nylon and graphite mixtures occurs around 30% graphite by weight. Below the percolation limit, the nylon powders prevent electrical conduction through physical separation of the graphite particles.

As the graphite content is increased above 30%, a steady increase in the electrical conductivity is observed.

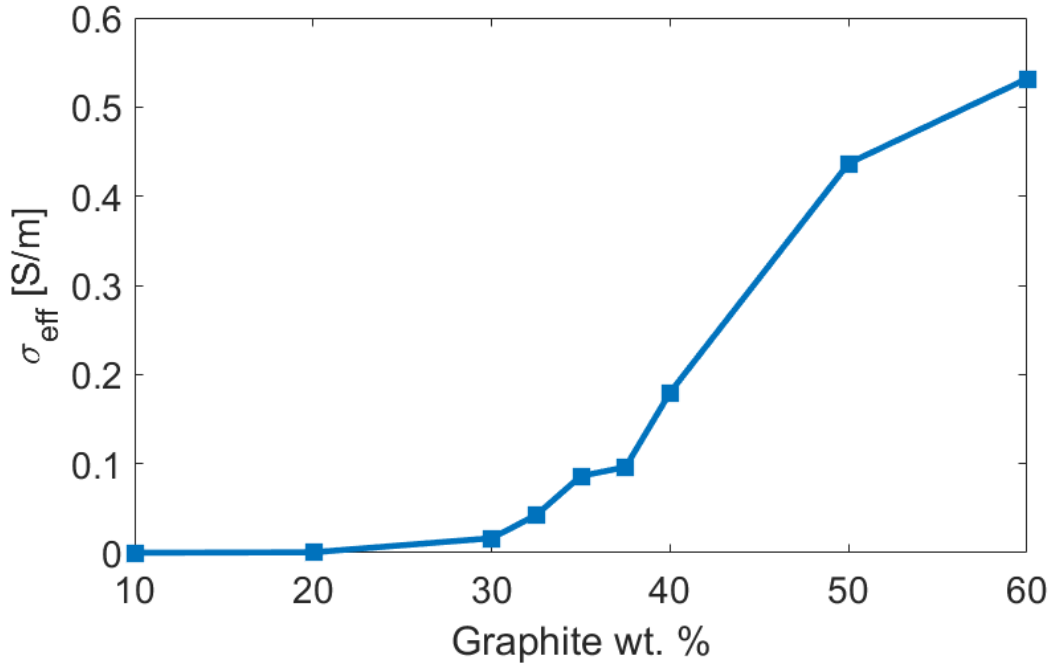


**Figure 3.5** Effective electrical conductivity as a function of graphite content at 27.12 MHz

In previous studies investigating the effect of increasing carbon black content on polymer composites, the percolation limit was clearly defined by a sharp increase in the electrical conductivity and quickly leveled out at higher concentrations [75] [79]. The percolation limit is not as clearly defined for the nylon/graphite mixtures, and the electrical conductivity gradually increases over a wide range of graphite content. One possible explanation for the wider percolation window in the graphite mixtures is that the anisotropic nature of graphite means the formation of conduction pathways is not a function of direct contact alone, but also the orientation of the graphite particles. In experiments conducted by Marinković et al. and Deprez et al., the effect of graphite orientation on the conductivity was studied by increasing the packing pressure of graphite powders. As the packing pressure increased, the graphite particles preferentially reoriented to cause an

increase in electrical conductivity [98] [86]. If the orientation of the graphite powders within the nylon composites is random, then it would be expected that increasing the loading would cause percolation to occur over a wider range of graphite concentrations.

In addition to the conductivity, the dielectric constant of the mixtures increases with graphite content. Shown in Figure 3.6, the dielectric constant appears to be divided into two distinct linear regions. The region of graphite concentrations below 37.5% is characterized by a gradual increase in the dielectric constant. Above 37.5%, however, the dielectric constant grows much more rapidly.

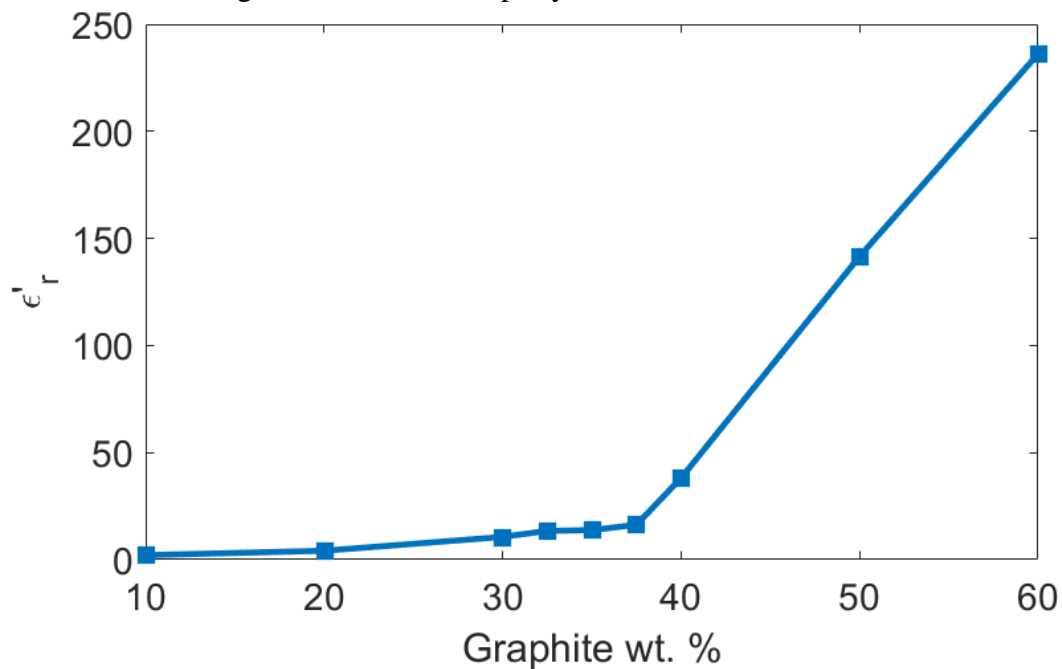


*Figure 3.6* Relative permittivity as a function of graphite content at 27.12 MHz

The observed increase in relative permittivity with increasing conductive filler content agrees with previous studies. It has been shown that conductive fillers in a polymer matrix exhibit an abrupt change and faster growth near the percolation threshold [99] [100]. The permittivity increase is most likely caused by charges building up at the interfaces between the conductive filler and the matrix which, interestingly, is the same mechanism that contributes to losses within the material [101] [102]. Even at high graphite loadings,

the polymer causes small insulating gaps between the graphite particles, and the system behaves like a network of connected capacitors [96]. As the graphite content is increased, the number of interfaces also increases causing a rise in the total capacitance and thus permittivity of the system.

The dielectric constant and effective conductivity both influence the RF heating characteristics of a material. Referring to Equation 2.5, the power dissipated is a function of the loss factor as well as the electric field developed within the material. In dielectrics, the electric field within the material is reduced by a factor of  $\epsilon_r'$  because polarization of the atoms in the material create an opposing electric field [103]. Superposition of the induced electric field with the applied electric field causes a reduction in the power dissipation as the relative permittivity increases. Therefore, there is a tradeoff between the material's loss factor and dielectric constant in RF heating. For this reason, the loss tangent is often considered in RF heating applications. The loss tangent of a material is the ratio between the effective loss factor and dielectric constant (Equation 3.14).

$$\tan\delta = \frac{\epsilon''_{eff}}{\epsilon'} \quad [3.14]$$

The loss tangent as a function of graphite content for the nylon mixtures is shown in Figure 3.7. Since the conductivity and relative permittivity both increase with graphite loading, the loss tangent provides a clear demonstration of the tradeoff that takes place. As the graphite content is increased, the loss tangent rises rapidly. However, it reaches a maximum value around 35% graphite before declining. The decrease in the loss tangent at higher graphite loadings shows the dielectric constant grows faster than the conductivity, and the shape of the trend aligns with the results of Yacubowicz et al. [99]. The loss tangent results suggest the 35% graphite mixtures is expected to have the highest degree of heating in RF radiation.

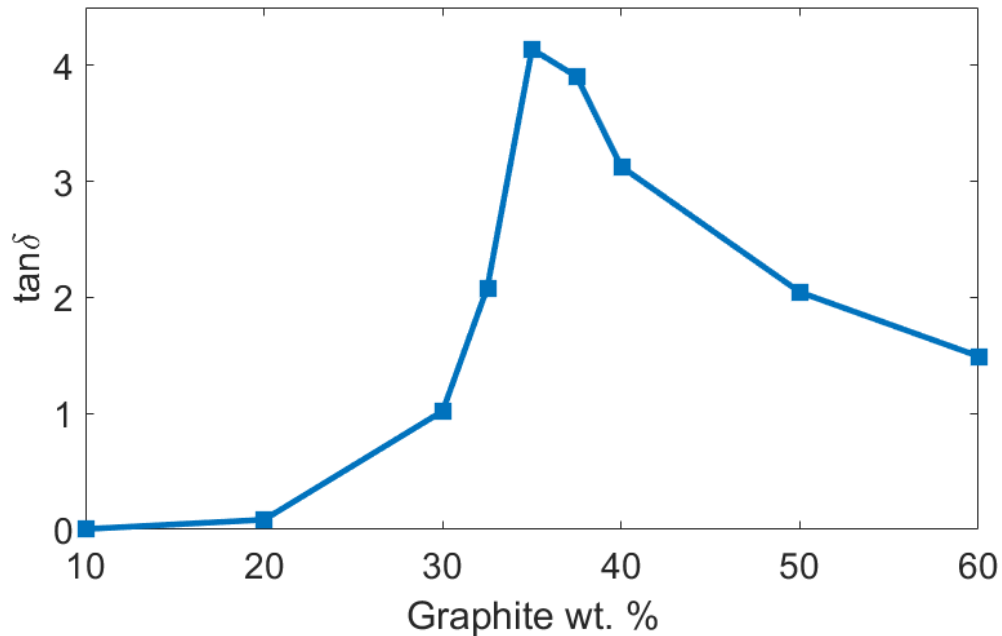


*Figure 3.7 Loss tangent as a function of graphite content at 27.12 MHz*

There is an inverse relationship between the electrical conductivity and penetration depth of RF radiation. The penetration depth as a function of graphite loading was calculated from the electrical conductivity measurements and is shown in Figure 3.8. The electrical conductivity increases with graphite content which then causes the penetration depth to decrease. The penetration depth for the 10% graphite mixture is 14.4 m and drops to 6.6 cm in the 60% sample. At 35% graphite by weight where the loss tangent reaches a maximum, the penetration depth is 16.4 cm. Penetration depth is an important parameter in RF heating because it determines the maximum part dimensions that can be heated.

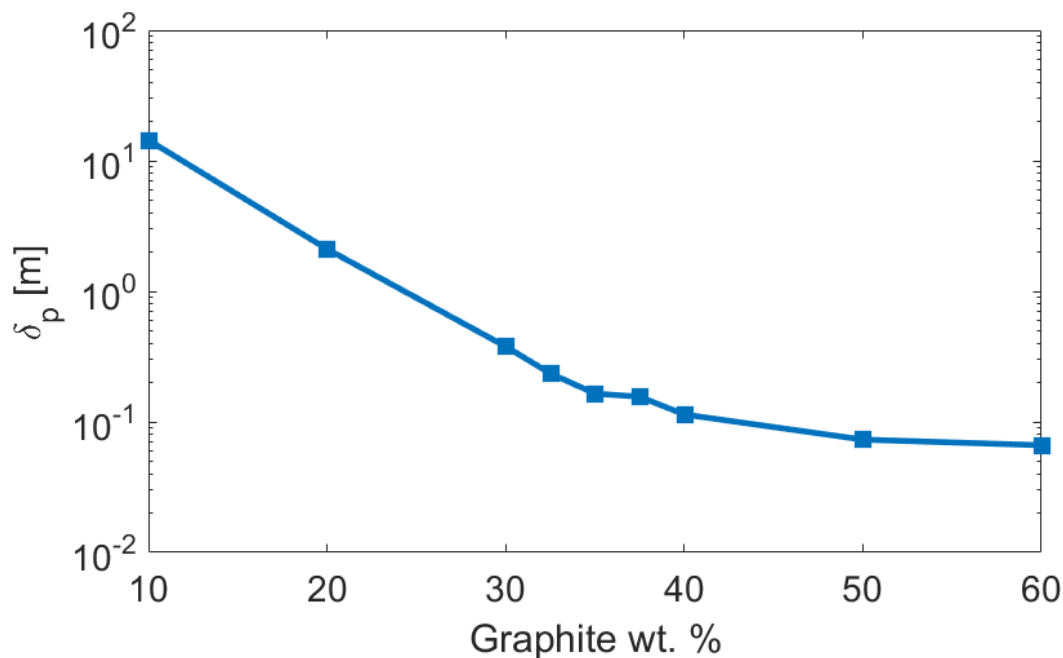


**Figure 3.8** Penetration depth as a function of graphite content at 27.12 MHz

The electrical properties of the nylon/graphite mixtures reveal interesting insights into the mechanism of charge storage and loss. The tradeoff between the electrical conductivity and relative permittivity in the loss tangent results indicate the expected dopant levels for the most effective RF heating. The penetration depth gives additional support for the choice of RF over higher frequencies and establishes the upper limit on the size of parts to be heated.

### **3.2 RF HEATING EXPERIMENTS FOR GRAPHITE-DOPED NYLON 12 MIXTURES**

#### **3.2.1 Experimental Apparatus**

The source of the RF radiation was a 560 W short wave diathermy machine manufactured by the Burdick Corporation with an operating frequency of  $27.12 \pm 0.16$  MHz. The diathermy machine featured a crystal controlled oscillator to minimize variation in the output frequency. In any RF application, maximum power transfer occurs when the load impedance matches the source impedance. The impedance was matched to the load by manually adjusting the output and tuning controls on the machine until the maximum

current was achieved, indicating the system was at resonance [104]. Newer diathermy equipment incorporates a matching circuit to continually tune the system without intervention.

The applicator, shown in Figure 3.9, consisted of parallel copper plates separated with threaded Teflon rods to enable adjustment of the electrode spacing. The electrodes were connected directly to the output of the diathermy machine and enclosed in a Faraday cage to prevent RF leakage. The electrode voltage was monitored through a differential capacitive voltage divider and an Iwatsu SS-5321 oscilloscope connected to the diathermy machine.

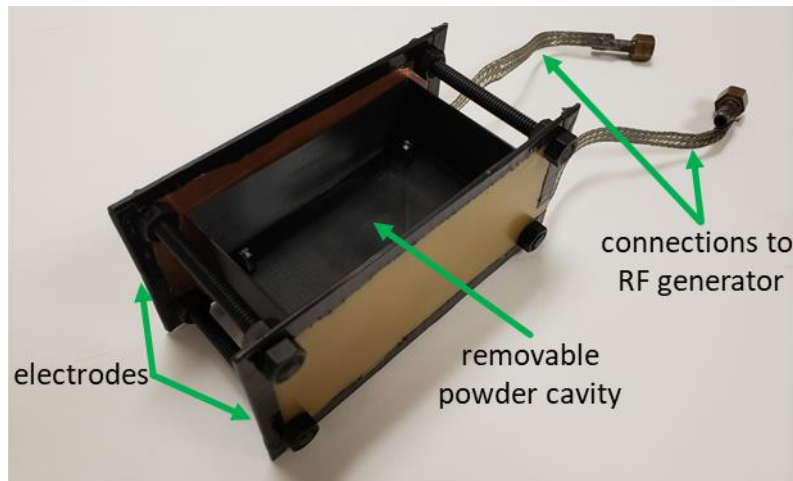


*Figure 3.9* Experimental applicator showing powder cavity, electrodes, and connections to RF generator

In-situ thermal monitoring of the samples was achieved using a FLIR E60 longwave infrared camera ( $\lambda = 7.5$  to  $13 \mu\text{m}$ ) that was mounted above the samples. The RF chamber, applicator, and camera configuration used in the experiments is shown in Figure 3.10. Non-contact infrared imaging was preferred over contact measurements such as thermocouples because it has no effect on the applied electric field, although it limits the measurements to the powder surface. Additionally, the IR measurements captured the temperature field, showing how the temperature was distributed across the surface.



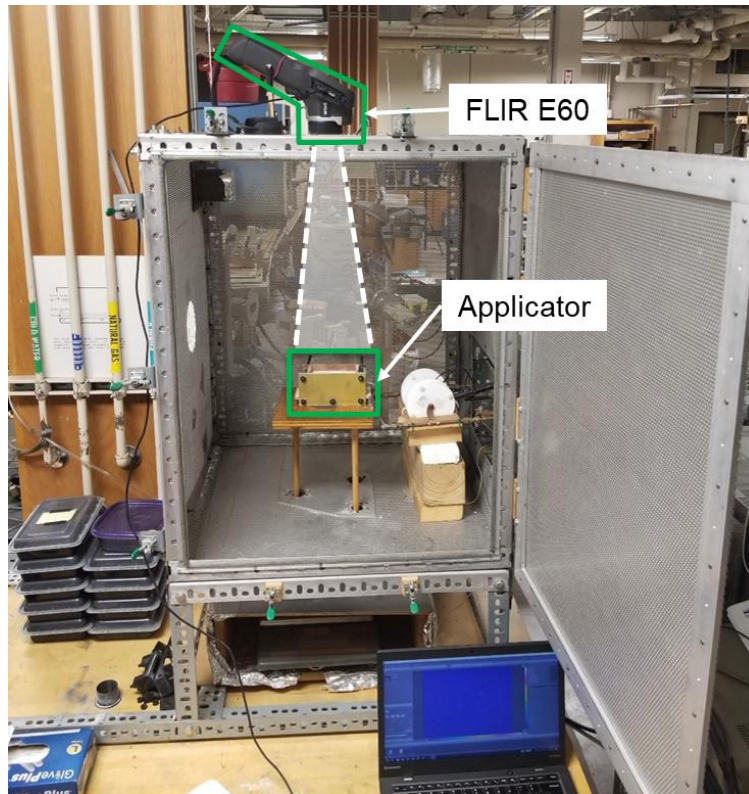


*Figure 3.10 Faraday cage surrounding applicator showing IR camera mounted above the sample*

### **3.2.2 Sample Preparation**

The goal of the RF heating experiments was to demonstrate selective heating in a powder bed containing virgin and doped powders. Preparation of the samples, then, required the powder bed to be separated into two distinct regions of virgin and doped powder. Thin PLA forms, shown in Figure 3.11, were used to selectively dope the powder bed into regions with circular, square, and rectangular cross sections. The forms allowed the geometry of the doped region to be clearly defined.

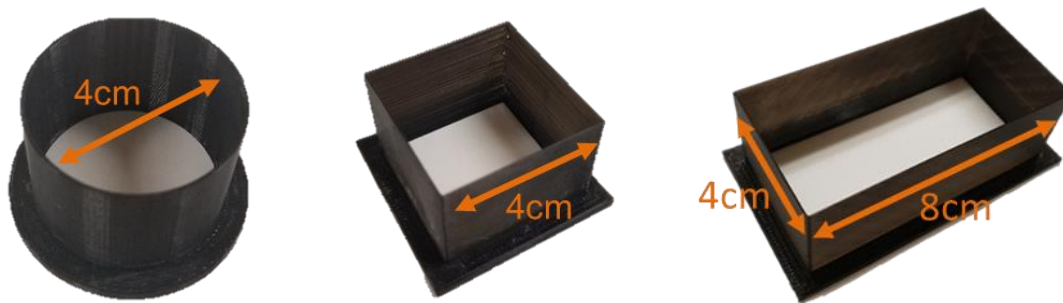


**Figure 3.11** Thin forms used to selectively dope the powder bed into regions of circular (left), square (center), and rectangular (right) cross sections.

The samples were prepared according to the steps outlined in Figure 3.12. The chamber was first partially filled with virgin nylon powder. Then, a small form was placed in the center and surrounded on all sides by additional virgin powder. Lastly, the doped powder was placed in the cavity that was created by the form, and the form was removed.

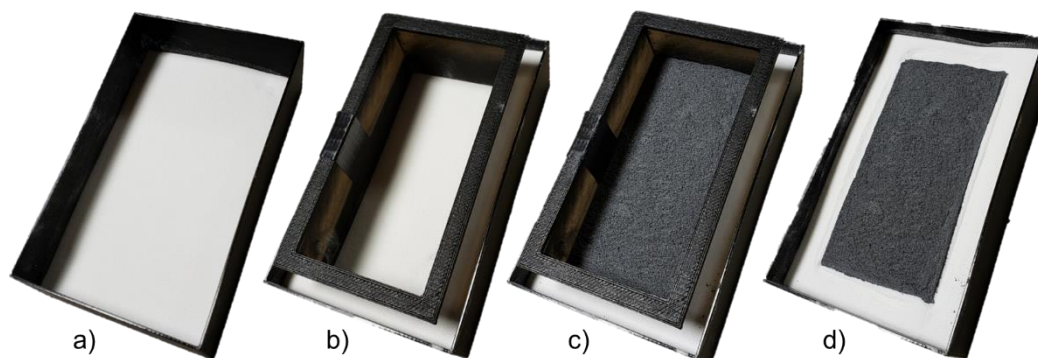


**Figure 3.12** Process showing how the PLA forms are used to separate doped powder from virgin. a) The chamber was filled with a base layer of virgin powder. b) The form was placed in the center of the chamber and surrounded by additional powder to create a cavity. c) The cavity was filled with graphite-doped powder. d) The form was removed to create an interface between doped and virgin powder.

After the form was removed, the powder bed consisted of a doped region having the cross section of the form surrounded by virgin powder. In this way, an unimpeded interface between the two regions was preserved to allow thermal conduction between them. In maintaining the boundary between the doped and virgin regions, the selectively doped powder bed provided a close approximation to the intended distribution of dopant

in the powder bed as part of a volumetric RF AM process. After defining the geometry of the doped region, the powder bed was placed between the electrodes in the RF chamber for the heating experiments.

### ***3.2.3 RF Heating Results and Discussion***

RF heating experiments were conducted to measure the effect of varying the graphite content on the temperature rise of the doped powders. The electrical property measurements were useful in determining the sources of charge storage and loss, but the properties represented intrinsic behavior of the materials and did not account for geometric effects. For each of the nylon/graphite mixtures, the circular form was used to define a cylindrical doped region. The circular cross section (Figure 3.11) was chosen for the initial experiments to minimize the number of corners and edges on the geometry that could lead to non-uniform heating. The tuning parameters of the RF generator were held constant for all experiments, and the surface temperature of the powder bed was recorded with the infrared camera. The average surface temperature of the doped region after 90 seconds of RF exposure as a function of graphite content is documented in Figure 3.13.

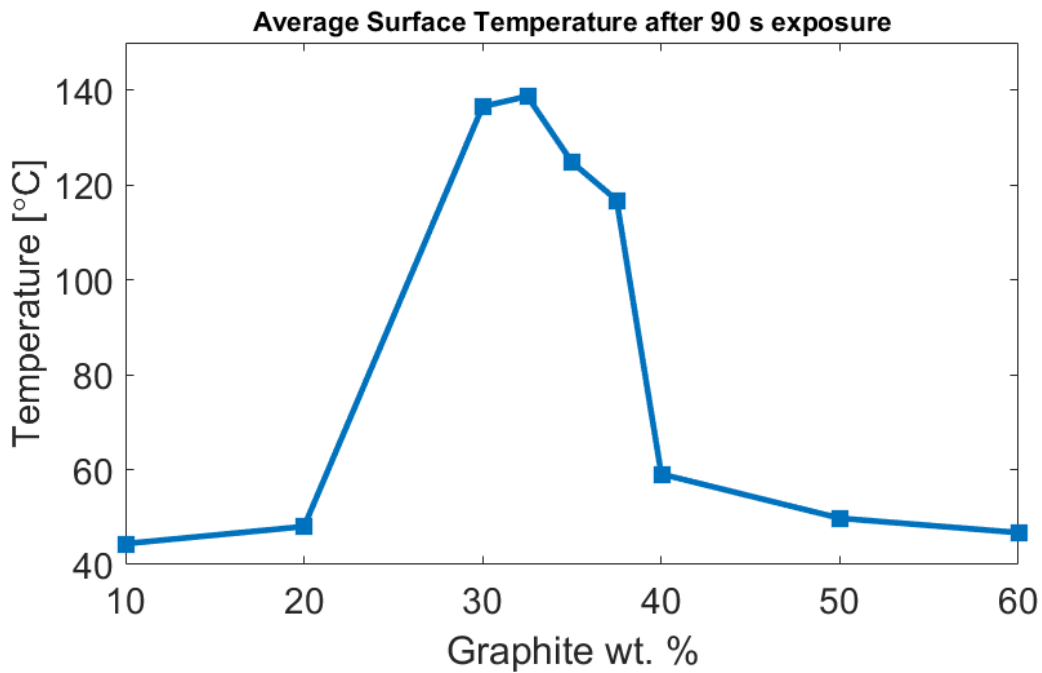


*Figure 3.13 Average surface temperature of the doped region after 90 seconds of RF exposure. The doped region had a circular cross section, and the tuning parameters of the RF generator were held constant.*

Very little heating occurred for graphite concentrations below 20% and above 40% by weight. However, the mixtures containing between 30% and 40% graphite produced a significant rise in surface temperature. The general trend from the RF heating experiments closely resembles the loss tangent data in Figure 3.7, although the maximum occurs at a lower graphite loading. The largest temperature rise occurred around 32.5% graphite, while the loss tangent was maximum at 35%. The limited heating in the lower concentrations can be attributed to the effective conductivity of the mixtures being sufficiently small to prevent substantial power loss. As the loading increased the loss tangent reached a maximum, corresponding to a maximum heat generation in the RF experiments. At higher concentrations, however, the heating data and loss tangent data differ. The loss tangent gradually declined after reaching a maximum, while the heating data showed a steep drop-off in temperature rise for concentrations above 40%. One possible explanation for the sharper decline in heating is the reduction in penetration depth that also occurred with

increasing graphite content. At higher graphite concentrations, the combination of decreasing loss tangent and penetration depth caused a larger decline in heat generation than could be explained by the loss tangent alone. Another potential reason for the reduction in absorption is the increase in drift velocity caused by higher **E**-field strengths in the RF heating experiments compared with those used in the electrical property measurements.

In addition to the electrical properties, the geometry of the material has been shown to influence the heating characteristics in RF applications. The presence of sharp corners and flat faces can distort the electric field within the material and result in non-uniform heating [21] [105]. Considering the fusion of graphite-doped nylon mixtures, non-uniform heating is undesirable because it can lead to unintended geometric artifacts in the fused parts. To investigate the effect of geometry on heating, RF experiments were conducted using the circular, square, and rectangular forms to define different geometries. Thermal images of the powder surface provided an indication of heating uniformity by showing the temperature distributions across the powder bed. For each of the RF experiments, the doped region contained 30% graphite by weight. In the absence of the conductive particles, the measured electrode voltage was approximately 1,070 V<sub>rms</sub>, corresponding to an estimated **E**-field strength of 343 V/cm. Figure 3.14 shows the surface temperature for a cylindrical doped region after five minutes of RF exposure. The electrodes in Figure 3.14 and subsequent infrared images were on the top and bottom with respect to the image, and the electric field direction is shown. The estimated **E**-field strength during the experiment was 375 V/cm. Notably, the IR measurements demonstrated selective heating of the doped powder, while the surrounding virgin powder was nearly unaffected by the radiation.

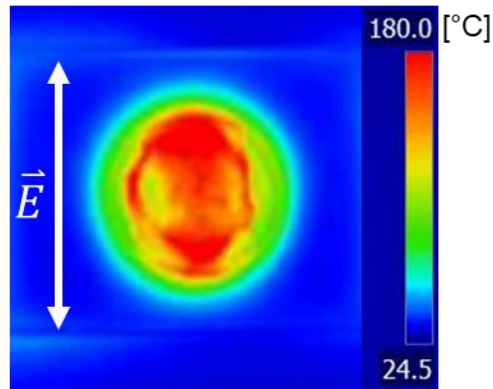


*Figure 3.14* Temperature profile after 5 minutes RF exposure for a doped region defined by a circular cross section. The electrodes are parallel to the top and bottom of the image, and the direction of the electric field is shown.

The temperature profile of the circular cross section indicated a higher concentration of heat in the center with lower heating on the sides. Some of the irregularities on the surface were a result of the powder consolidating as it was heated beyond its melting point. As the powder densified, cooler surrounding powder fell from the sides and created what appeared to be cooler regions on the part surface.

The surface temperature distribution for a doped region with a square cross section is given in Figure 3.15. The image was captured after six minutes of RF exposure, and electric field strength was approximately 331 V/cm. The temperature pattern for the square geometry indicated highly non-uniform heating in which some regions were substantially hotter than their surroundings. In particular, thermal concentrations occurred at the corners and extended through the center of the part. Each of the flat edges of the square cross section were characterized by cooler regions near the center of the edge.

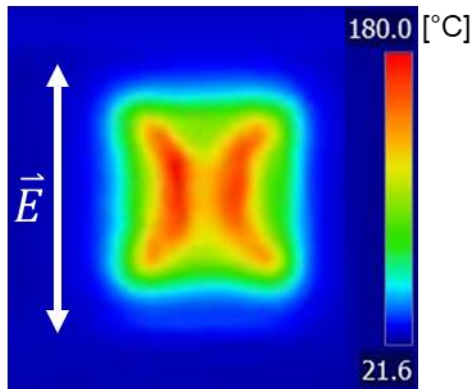


**Figure 3.15** Temperature profile after 6 minutes RF exposure for a doped region defined by a square cross section. The electrodes are parallel to the top and bottom of the image, and the direction of the electric field is shown.

Figure 3.16 shows the temperature distribution after five minutes of RF exposure for a rectangular cross section. During the experiment, the electric field strength was approximately 387 V/cm. Similar to the temperature pattern for the square cross section, the rectangular geometry showed highly non-uniform heating. Local hot spots in the corners of the rectangle were connected in the direction of the electric field, and the heating of the sides was substantially greater than in the center region. As with the circular cross section IR image, some of the irregularities were caused by the powder densification and subsequent powder falling to the molten surface.

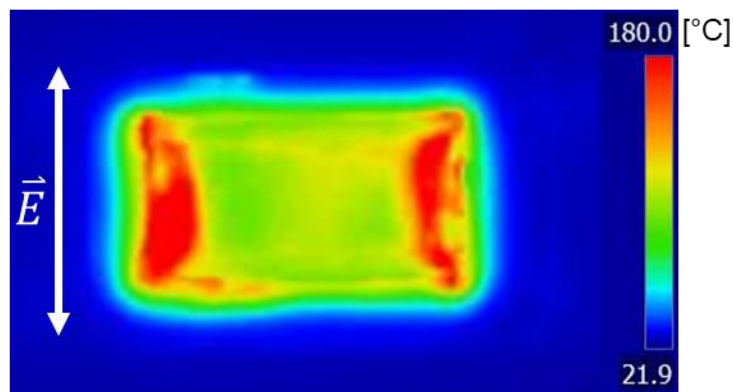


**Figure 3.16** Temperature profile after 5 minutes RF exposure for a doped region defined by a rectangular cross section. The electrodes are parallel to the top and bottom of the image, and the direction of the electric field is shown.

RF radiation was applied to the samples until substantial portions of the surface exceeded the melting temperature of the nylon 12, which was approximately 180°C. In these regions, the heat generation was sufficient to melt the nylon particles and allow fusion to take place as the powder bed cooled. As shown in Figures 3.17-3.19, the fused parts for each of the doped geometries highlighted the non-uniform heating that occurred as a result of the geometric definition. The total RF exposure time depended on the tuning parameters of the generator and the electrode voltage during the experiments. The heating times for the circular, square, and rectangular parts were five minutes, seven minutes and thirty seconds, and six minutes, respectively. In general, the shape of the parts matched the heating patterns in the IR images. However, out-of-plane curvature revealed effects that could not be predicted from the IR measurements. The circular cross section geometry produced a fused part that was elongated in the direction of the electric field with extreme curvature on the bottom surface. For the square cross section, the faces of the fused part were curved as the local cooler regions prevented fusion from taking place. The sides of the part were thicker in the direction of the electric field corresponding to the hotter regions in the thermal image of the powder surface. The fused geometry from the rectangular cross section followed similar trends found in the square where the faces were curved due to electric field distortions within the doped region. The side profile in Figure 3.19 highlights the thickening of the part on the sides in the direction of the electric field.



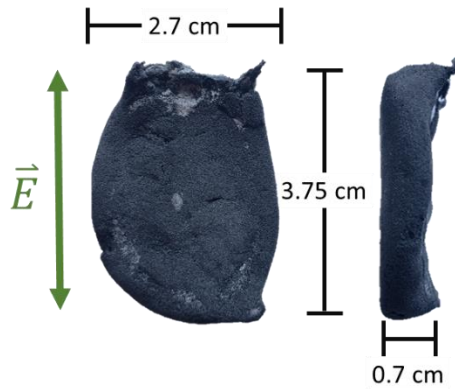


**Figure 3.17** Fused part created from a selectively doped powder bed in which the geometry was defined by a circular cross section. The doped region contained 30% graphite by weight, and the part was exposed to RF radiation for five minutes.

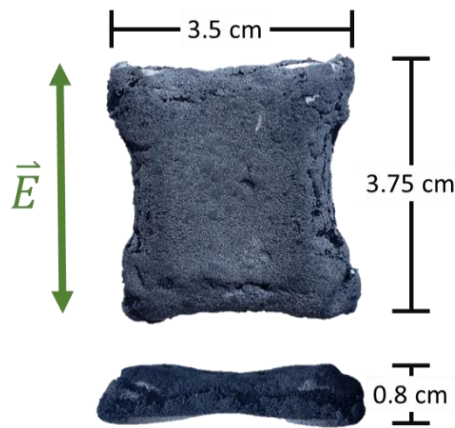


**Figure 3.18** Fused part created from a selectively doped powder bed in which the geometry was defined by a square cross section. The doped region contained 30% graphite by weight, and the part was exposed to RF radiation for seven minutes and thirty seconds.



**Figure 3.19** Fused part created from a selectively doped powder bed in which the geometry was defined by a rectangular cross section. The doped region contained 30% graphite by weight, and the part was exposed to RF radiation for six minutes.

Previous studies have investigated the geometric effect of heating uniformity in RF heating applications. Uyar et al. showed the development of temperature spikes at the edges and corners of block shaped foods subjected to RF radiation [21]. Although the applied electric field was uniform, the field became distorted through interactions with the material and boundary condition effects. Non-uniform heating was caused by local field concentrations within the material. The geometric irregularities in the RF-fused nylon parts were similarly caused by electric field distortions. The influence of geometry on heating uniformity is further explored in the next chapter.

Although the effects of geometry on heating uniformity require further investigation, the experiments demonstrated selective heating and volumetric powder fusion using RF radiation as the sole energy source. By combining particular proportions of nylon and graphite powders, the effective electrical properties of the composites were shown to generate sufficient heat from RF exposure to fuse the nylon particles.

#### ***3.2.4 Mechanical Properties of Sintered Parts***

The strength of the RF-sintered parts was evaluated by performing standard tension tests using an Instron model 3345 frame in a displacement-controlled experiment. The fused parts with a rectangular cross section were machined to conform with ASTM D638 type V standard tensile specimens. The specimens were positioned such that the gage sections aligned with the center of the fused parts as depicted in Figure 3.20. The parts were created under nominally identical processing conditions using a nylon/graphite mixture containing 30% graphite by weight and an RF exposure time of nine minutes. In total, five samples were created from the RF-sintered parts, and the mechanical properties were assessed.

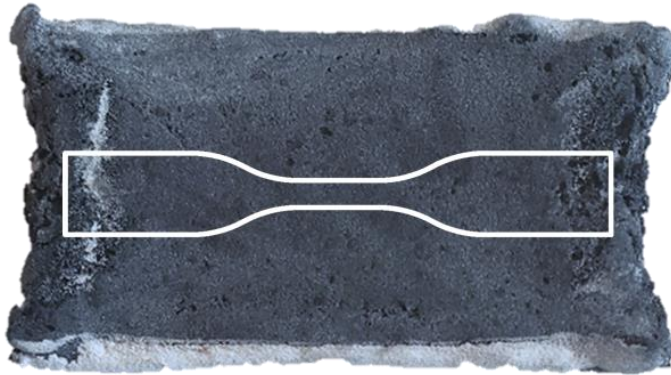


*Figure 3.20 Position of ASTM D638 type V tensile bar with respect to RF-sintered geometry*

Figure 3.21 shows a characteristic example of the tensile bars after machining. Large amounts of external porosity were observed across the surfaces of the specimens. Porosity in laser sintered parts is often attributed to incomplete melting of the polymer particles and can result in the formation of voids within the parts [106]. However, the spherical morphology of the voids in the tensile specimens suggested the porosity was unlikely caused by incomplete particle melting. Another possible source for the voids was through gas desorption from the graphite particles that trapped bubbles within the molten polymer. In experiments conducted by Hashiba et al., mixtures containing graphite powder showed a peak in CO<sub>2</sub> desorption at 200°C [107]. Similar temperatures were achieved during the RF heating experiments to ensure melting of the polymer, and thus gas desorption within the molten parts was possible.



*Figure 3.21 ASTM D638 type V tensile bar machined from RF-sintered specimens*

The five specimens were tested according to ASTM D638 with an testing speed of 1 mm/min. Strain measurements were collected using an Epsilon Technology Corp. model 3442 extensometer with a 0.3” gage length to match the specimens. The extensometer was

mounted to the samples for the duration of the experiments, and the samples were tested to failure. A characteristic stress/strain response from the tension tests is shown in Figure 3.22. Three of the five samples fractured within the gage section of the tensile bar, while the remaining two samples fractured near the grip section.

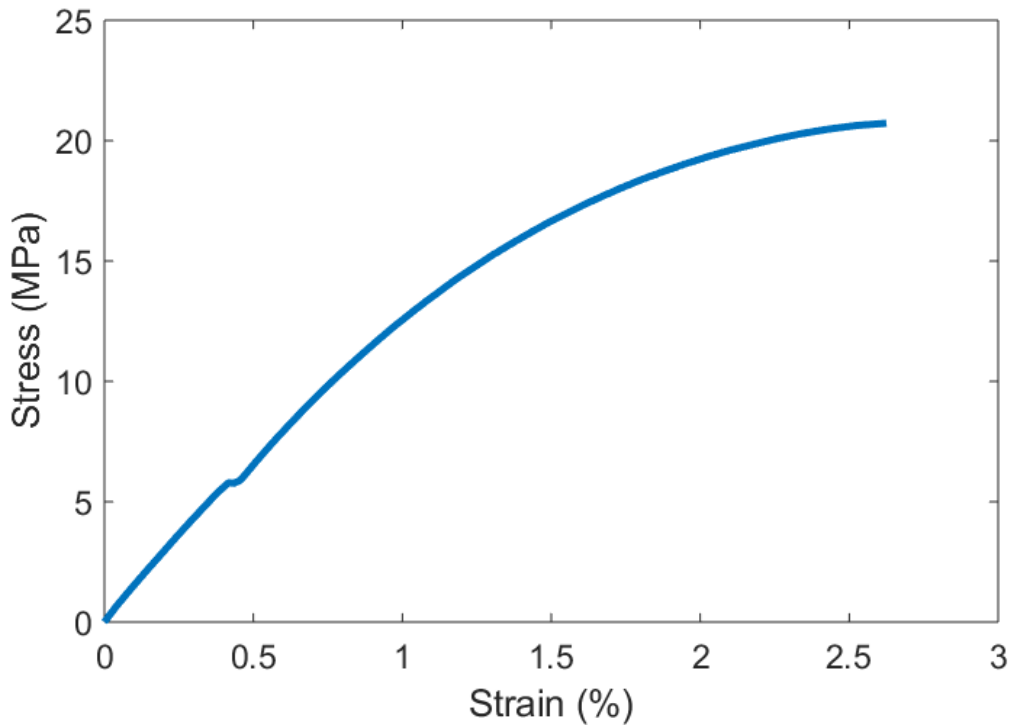


*Figure 3.22 Characteristic stress/strain response from RF-sintered tensile specimens*

The mechanical properties of the RF-sintered specimens were compared with laser sintered nylon 12 as reported by Stratasys Direct Manufacturing, and the results are shown in Table 3.1. The error reported from the experimental results corresponded to the standard error of the measurements across the five samples. In general, the mechanical properties of the RF-sintered parts were considerably poorer than laser sintered nylon 12, showing a reduction in the modulus, ultimate tensile strength, and elongation at break. The external porosity on the samples likely contributed to the lower tensile strength and elongation by

creating stress concentrations within the specimens. Examination of the fracture surfaces revealed the failure locations coincided with one of the voids in nearly every test.

*Table 3.1 Mechanical properties of laser sintered nylon 12 compared with RF-sintered properties. The error from the experimental results corresponds to the standard error of the measurements across the five samples*

	Nylon 12 [108]	Experiments
Tensile Modulus	1,700 [MPa]	1,361 ± 44 [MPa]
Ultimate Tensile Strength	46 [MPa]	16.5 ± 1.2 [MPa]
Elongation at Break	4-15 %	2.12 ± 0.35 %

The reduction in mechanical properties of nylon 12 through the addition of graphite agrees with the results observed by Lee et al., where the introduction of carbon black and graphite negatively impacted the flexural strength of the polymer composite [81]. The strength of RFAM parts could be improved by considering other forms of carbon for the dopant such as carbon nanotubes. Previous studies have shown the addition of carbon nanotubes can also improve the electrical conductivity of the composites and reduce the amount of dopant necessary to achieve electrical percolation [79] [80]. Further testing is required to improve the mechanical performance of RFAM parts and mitigate the formation of voids within them.

### 3.3 CLOSURE

Radio frequency additive manufacturing relies on the combination of an electrically insulating polymer with an electrically conductive dopant to achieve selective fusion when subjected to RF radiation. The feasibility of the process is determined by the ability to modify the electrical properties of the polymer with the addition of the dopant and the ability to demonstrate powder fusion using RF radiation. It was shown that the electrical properties of nylon powder could be enhanced with the addition of graphite powder. As

the graphite content was increased above 30% by weight, the effective properties of the composite mixture transitioned from insulating to conducting in nature. RF heating experiments on the mixtures showed that temperature rises above the melting temperature of the polymer matrix were possible for certain compositions. Selective fusion of the doped mixtures supported the RFAM hypothesis and established a proof-of-concept for the process.

One of the key findings from the RF heating experiments on the nylon/graphite mixtures was identifying the range of graphite concentrations that corresponded to the highest degree of heating in 27.12 MHz RF radiation. Increasing the graphite content had a positive effect on the heat generation for concentrations below 32.5% graphite by weight. Above this limit, however, the heating decreased with increasing graphite content due to a reduction in the loss tangent and penetration depth at higher concentrations.

The graphite content corresponding to the maximum temperature rise in the experiments represents an important parameter in the development of a radio frequency additive manufacturing system. Supplying too much dopant to the powder bed produces diminishing returns on the observed heating. Therefore it is not advantageous to increase the graphite content above the critical limit. This has the effect of bounding the design space of RFAM parts to graphite concentrations below the 32.5% limit.

The initial RF heating experiments established the feasibility of the RFAM process, but the bench-top testing necessarily limited the complexity of parts that could be produced. The forms used to pattern the dopant restricted the achievable geometries to prismatic structures. Removal of the forms before heating introduced additional sources of variability between experiments, and the definition of the doped geometry depended on the friction between the powder bed and the walls of the form. The experimental system further restricted the doped powders to be uniform in composition. As demonstrated by the fused

parts, uniformly doped powder beds exhibit inhomogeneous heating as a result of the geometry. To improve the heating uniformity, a system capable of spatially varying the dopant concentration may be necessary. Furthermore, the use of graphite powder as the electrically conductive dopant causes a reduction in the mechanical strength and ductility of the fused parts. Alternative dopant materials such as carbon nanotubes should be considered in future work to provide strength improvements in addition to electrical conductivity.

One of the goals of radio frequency additive manufacturing is to produce geometrically complex polymer parts. Therefore, a precise method of patterning the dopant to allow spatial gradation and three dimensional geometries is required. Building on the electrical property measurements and RF heating results, approaches to functionally grade the powder bed and distribute the dopant are explored in subsequent chapters. The findings of the bench-top experiments highlighted the potential of RFAM to create parts in a volumetric fashion and introduced important research challenges to be addressed during the process development.

## **Chapter 4: Computational Design Strategy to Improve RF Heating Uniformity**

The utility of additive manufacturing originates from the ability for designers to produce complex geometries that cannot be manufactured using conventional methods. Heating uniformity issues in RF applications present a challenge to the development of a radio frequency additive manufacturing process because they place limitations on the geometries that can be created. The focus of this chapter is to introduce computational models for the doped powder bed in RFAM and use them to predict the temperature rise and phase change behavior during RF radiation exposure. The models are then used in a computational design strategy in which several solutions are proposed to improve the heating uniformity within the parts and thus improve the geometric resolution of the RFAM process by functionally grading the dopant throughout the powder bed.

### **4.1 PREDICTION OF TEMPERATURE RISE AND PHASE TRANSITION USING FINITE ELEMENT ANALYSIS**

Analytical solutions to RF heating problems exist only for simple geometries. As the geometry of the lossy material grows in complexity, predicting the temperature rise within the material requires numerical methods and finite element analysis (FEA) [63] [61]. Radio frequency additive manufacturing seeks to create arbitrary geometries; thus, such methods are necessary to predict the effects of RF heating on a powder bed. RF heating simulations are comprised of an electric component as well as a thermal component. For this reason, COMSOL Multiphysics® is commonly used in RF heating simulations. COMSOL® is a powerful FEA engine capable of calculating the electric and thermal effects in RF heating problems with complex geometries. To predict the temperature rise for RFAM parts, COMSOL® version 5.3a was used in conjunction with the supplemental AC/DC and Heat Transfer modules.



#### 4.1.1 AC/DC Model Parameters

For the electric component in the simulation, three primary relationships were used to determine the heat generation. Gauss' Electric Law in semiconducting media (Equation 4.1), the electric field definition (Equation 4.2), and the right-hand-side of Ampere's Law in point form (Equation 4.3) were applied to determine the current density ( $\mathbf{J}$ ), electric field strength ( $\mathbf{E}$ ), and electric potential ( $V$ ) [109]. The inputs to the electrical model were the peak root mean square potential difference at the electrodes ( $V_0$ ), frequency ( $\omega$ ), and the electrical properties of the doped and virgin powder regions ( $\sigma$  and  $\epsilon_r$ ). In Equation 4.3,  $\epsilon_0$  represents the permittivity of free space and has a value of  $8.85 \times 10^{-12}$  F/m.

$$\nabla \cdot \mathbf{J} = 0 \quad [4.1]$$

$$\mathbf{E} = -\nabla V \quad [4.2]$$

$$\mathbf{J} = (\sigma + j\omega\epsilon_0\epsilon_r)\mathbf{E} \quad [4.3]$$

The applicator and virgin powder bed were modelled as a rectangular cavity, and the electrodes were simulated as voltage boundary conditions on opposite faces of the applicator. In the case of RFAM where the size of the applicator was much smaller than the radiation wavelength, the electroquasistatic (EQS) approximation was valid. Under the EQS approximation, wave propagation effects and magnetic field contributions to heating can be ignored [109]. Eliminating the wave effects greatly reduced the computational complexity of the RF heating simulations. By considering the voltage as the primary input, the electroquasistatic approximation was enforced. The remaining four faces of the applicator were prescribed electrically insulating boundary conditions in which the current density normal to the surface was zero, depicted in Equation 4.4.

$$\mathbf{n} \cdot \mathbf{J} = 0 \quad [4.4]$$

The doped geometry was placed in the center of the cavity with corresponding electrical properties. From the current density and electric field, the resistive power density ( $Q_{rh}$ , W/m<sup>3</sup>) was determined according to Equation 4.5. The power density represented the volumetric energy loss within the doped region and provided a measure of the electric field heating.

$$Q_{rh} = Re\{\mathbf{J} \cdot \mathbf{E}\} \quad [4.5]$$

The properties in the electrical simulation were derived from the measurements outlined in Chapter 3. The values for the model parameters are given in Table 4.1. The electrical properties in the models did not include a dependence on temperature. Previous studies have shown the conductivity of graphite/polymer composites to decrease with increasing temperature, possibly due to the disruption of conductive pathways through thermal expansion during heating [110]. Further testing is required on the nylon and graphite composites to confirm the temperature dependence and incorporate it into the simulation models.

*Table 4.1 Electrical properties used in simulation for doped and virgin powder regions*

Property	Symbol		Value	
Electrode Voltage	$V_0$		1200	[V]
Frequency	$f$		27.12	[MHz]
Effective Conductivity	$\sigma_{\text{eff}}$	Virgin	0	[S/m]
		Doped	0.04	[S/m]
Relative Permittivity	$\epsilon_r$	Virgin	2	
		Doped	13.8	

### 4.1.2 Heat Transfer Model Parameters

The temperature rise in the simulations was calculated in the thermal component of the model according to Equations 4.6 and 4.7. The electric and thermal modules were coupled together through the resistive power density as depicted in Equation 4.6. The inputs to the thermal model were density ( $\rho$ ), specific heat ( $C_p$ ), and thermal conductivity ( $k$ ), and temperature was the output [111].

$$\rho C_p \frac{\partial T}{\partial t} + \nabla \cdot q = Q_{rh} \quad [4.6]$$

$$q = -k \nabla T \quad [4.7]$$

Thermal insulation boundary conditions were prescribed to each external face with the exception of the top face in which thermal convection was considered. The thermal insulation prevented outward heat flux according to Equation 4.8, while the convection heat flux followed Equation 4.9.

$$-n \cdot q = 0 \quad [4.8]$$

$$-n \cdot q = h(T_{ext} - T) \quad [4.9]$$

The thermal models also included phase transition between the solid and liquid phases. COMSOL® uses an apparent heat capacity formulation to model phase change by assuming a smooth transition between phases across a predefined temperature interval. Outside the temperature window, either the solid or liquid phase properties were used depending on whether the temperature was above or below the transition region. Within the interval, the material had mixed properties according to the smooth transition function ( $\theta$ ) that represented the fraction of each phase at a given temperature. The thermal properties were calculated according to Equations 4.10-4.13, where the heat capacity ( $C_p$ ) incorporated the latent head of fusion ( $L$ ) to compensate for energy losses during the phase

transition. The subscripts  $S$  and  $L$  refer to the properties for the solid and liquid phases, respectively.

$$\rho = \theta\rho_S + (1 - \theta)\rho_L \quad [4.10]$$

$$k = \theta k_S + (1 - \theta)k_L \quad [4.11]$$

$$\alpha_m = \frac{1}{2} \left[ \frac{(1 - \theta)\rho_L - \theta\rho_S}{\theta\rho_S + (1 - \theta)\rho_L} \right] \quad [4.12]$$

$$C_p = \frac{1}{\rho} [\theta\rho_S C_{p,S} + (1 - \theta)\rho_L C_{p,L}] + L \frac{\partial \alpha_m}{\partial T} \quad [4.13]$$

The thermal properties used in the simulations were taken from values found in literature and are given in Table 4.2. One of the simplifications in the models was that only the thermal properties of the polymer powder were considered, and no distinction was made between the thermal properties of the virgin and doped regions. In omitting the contribution from the dopant, the melting characteristics of the polymer powders were prioritized. The addition of a graphite dopant has been shown to increase the thermal conductivity of polymer mixtures. However, graphite powders have a wide range of reported thermal conductivities, and the values for dry powder mixtures have not been widely studied [112]. Without direct property measurement, it was decided to consider only the polymer properties in the simulations. Further, as RF radiation heats the volume simultaneously, the thermal conductivity plays a smaller role in the heating of the mixtures [26]. The models allowed thermal conduction into the surrounding virgin powder bed and sintering beyond the domain of the doped region. An opportunity for future work would be direct thermal property measurement of the nylon/graphite composites to enhance the simulations.

**Table 4.2** Thermal properties used in the simulations, including phase change. The values corresponded to pure nylon 12 powder and were taken from sources in literature.

Property	Symbol		Value	Reference
Convection Coefficient	$h$		25 [W/m <sup>2</sup> K]	[113]
Melting Point	$T_{S \rightarrow L}$		180 [°C]	[89]
Latent Heat	$L_{S \rightarrow L}$		96.7 [kJ/kg]	[114]
Thermal Conductivity	$k_S$	Solid	0.1 [W/mK]	[115]
		Liquid	0.26 [W/mK]	[115]
Density	$\rho_S$	Solid	490 [kg/m <sup>3</sup> ]	[113]
		Liquid	1010 [kg/m <sup>3</sup> ]	[113]
Heat Capacity	$C_{p,S}$	Solid	1287 [J/kgK]	[116]
		Liquid	2500 [J/kgK]	[114]

Figure 4.1 shows a representation of the simulated domains in COMSOL® with the doped geometry in the center. The voltage and convection boundary conditions are displayed. The models were simulated in a time-dependent, transient study with a prescribed radiation exposure time.

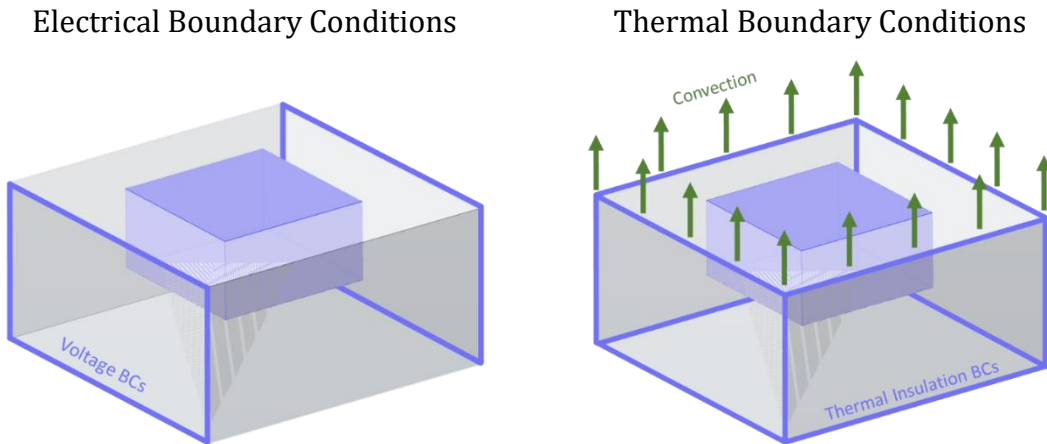


**Figure 4.1** Simulated domains in COMSOL®. The electrodes are represented by voltage boundary conditions. The doped region and surrounding region are distinguished by prescribing electrical properties corresponding to the doped and virgin nylon powders, respectively.

## 4.2 DEPENDENCE OF HEATING UNIFORMITY ON DOPED GEOMETRY

The COMSOL® models were used to predict the temperature rise due to RF radiation for various geometries. Figure 4.2 gives the temperature profiles at the center cross section for a sphere and cubic doped region. The white lines in the figures correspond to the electric field within the powder bed. Although the applied electric field is uniform, the presence of the doped geometry causes distortions in the field as it interacts with the higher conductivity in the region. Referring to the power loss in Equation 2.5, a non-uniform electric field gives rise to non-uniform power loss within the material. The electric field is uniform within a spherical geometry, as evidenced by the parallel, equally spaced field lines in Figure 4.2a. The heating within the sphere is also uniform as a result of the uniform electric field. However, when the geometry is changed to a cube, as in Figure 4.2b, the electric field within the conducting region becomes curved with local concentrations in the field lines. Local hot and cold regions arise from the non-uniform electric field in the cube. Non-uniform heating is expected for any geometry that deviates from spherical. The presence of sharp corners and flat faces are particularly prone to causing electric field concentrations within the doped region.

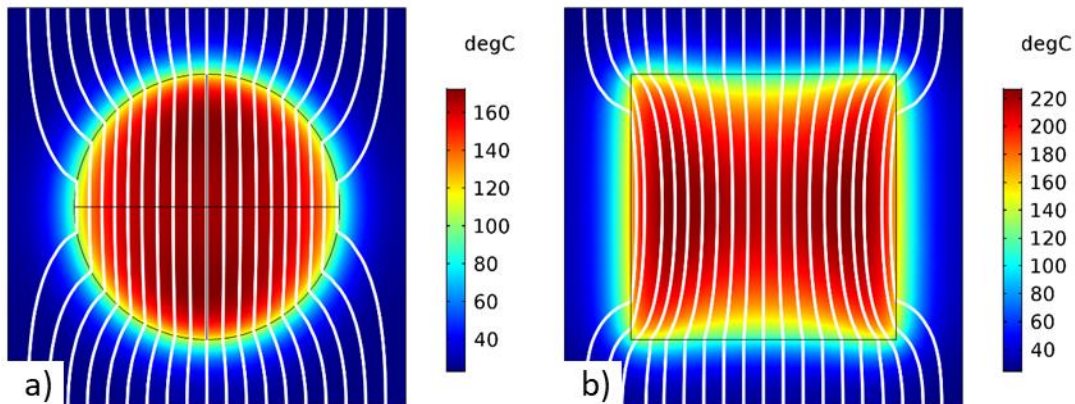


*Figure 4.2* Temperature distribution at the center cross section for a sphere (a) and cube (b). The white lines in the image correspond to the electric field lines in the powder bed.

The simulated surface temperatures compared to the experimentally measured IR surface temperatures for square, circular, and rectangular doped regions are given in Figure 4.3. Comparing the temperatures at three locations for each of the geometries shows close agreement between the models and the experiments. Another point of agreement is in the presence of hot spots on the sides for the square and rectangle, however the shape of the temperature distributions differs between the simulations and experiments. The local hot spots in the IR images are much more exaggerated than the simulations suggest, but the general temperature distributions are similar.

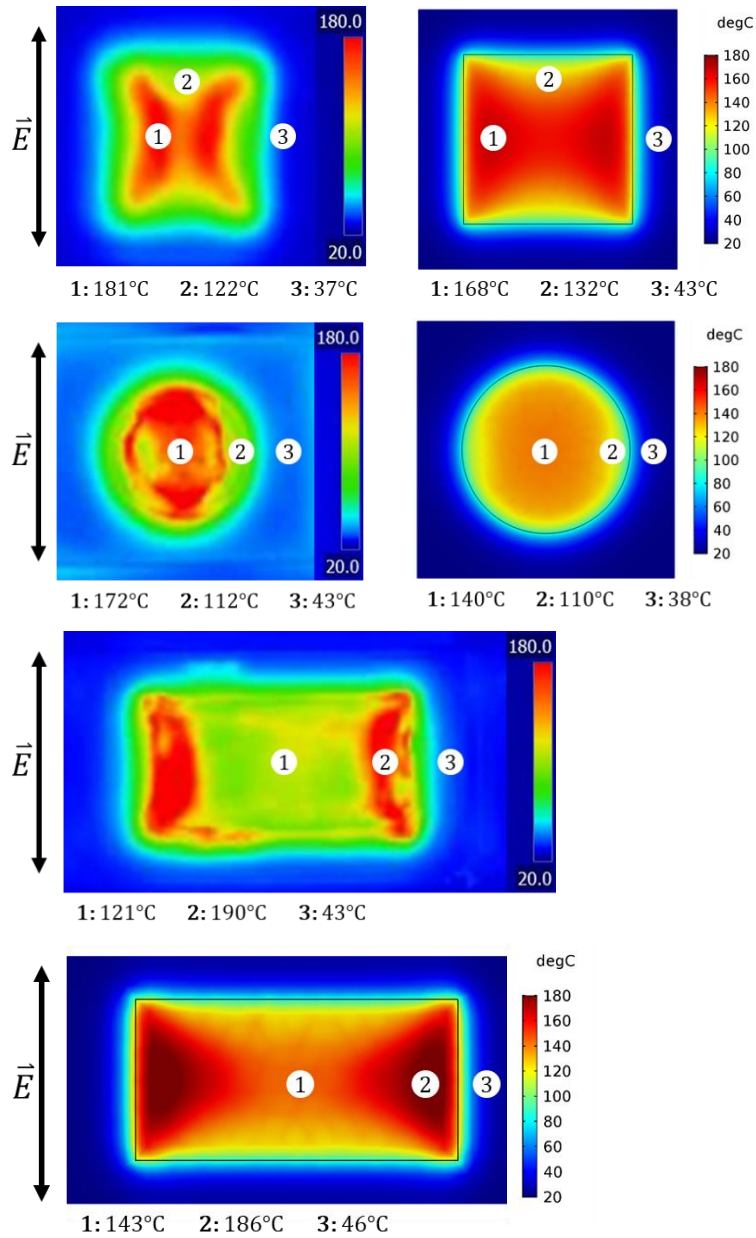


**Figure 4.3** Comparison between the simulated surface temperature and the experimentally measured surface temperature for doped regions with square, circular, and rectangular cross sections. The numbers in the figure correspond to the temperature measurement locations.

The geometry of the sintered parts can be approximated by considering the phase of the powder bed at the end of the simulation. Although the models do not account for cooling effects, the part geometry can be predicted by representing the volume of the



domain that is in the liquid phase after the simulated RF heating. Due to the steep thermal gradients at the phase transition boundary, accurate predictions often require an extremely fine FEA mesh and can be computationally expensive to solve [117]. The phase change parameter in COMSOL® ( $\theta$ ) is represented by a continuous value between 0 and 1 where the material at a given location is entirely solid when  $\theta=0$ , entirely liquid when  $\theta=1$ , and has mixed properties between the two domains. Smaller windows can produce sharp transitions in phase but with an added computational complexity from the necessary mesh refinement. To reduce the computational expense, a transition window of 60°C is used for the RF simulations.

The geometry is approximated by displaying only the volume in which the phase change parameter is equal to one where the temperature exceeds the melting temperature of the polymer. The thermal model is improved by incorporating phase transition by considering the energy required to fuse the polymer (latent heat). Figure 4.4 shows the comparison between the geometry predictions from the simulations with the experimentally fused parts for the circular, square, and rectangular cross sections. The geometric predictions successfully capture the main trends in the fused parts. Namely, the elongation of the cylinder in the direction of the applied electric field and the thickening of the sides in the square and rectangular parts show agreement between the simulation models and the fused geometries.

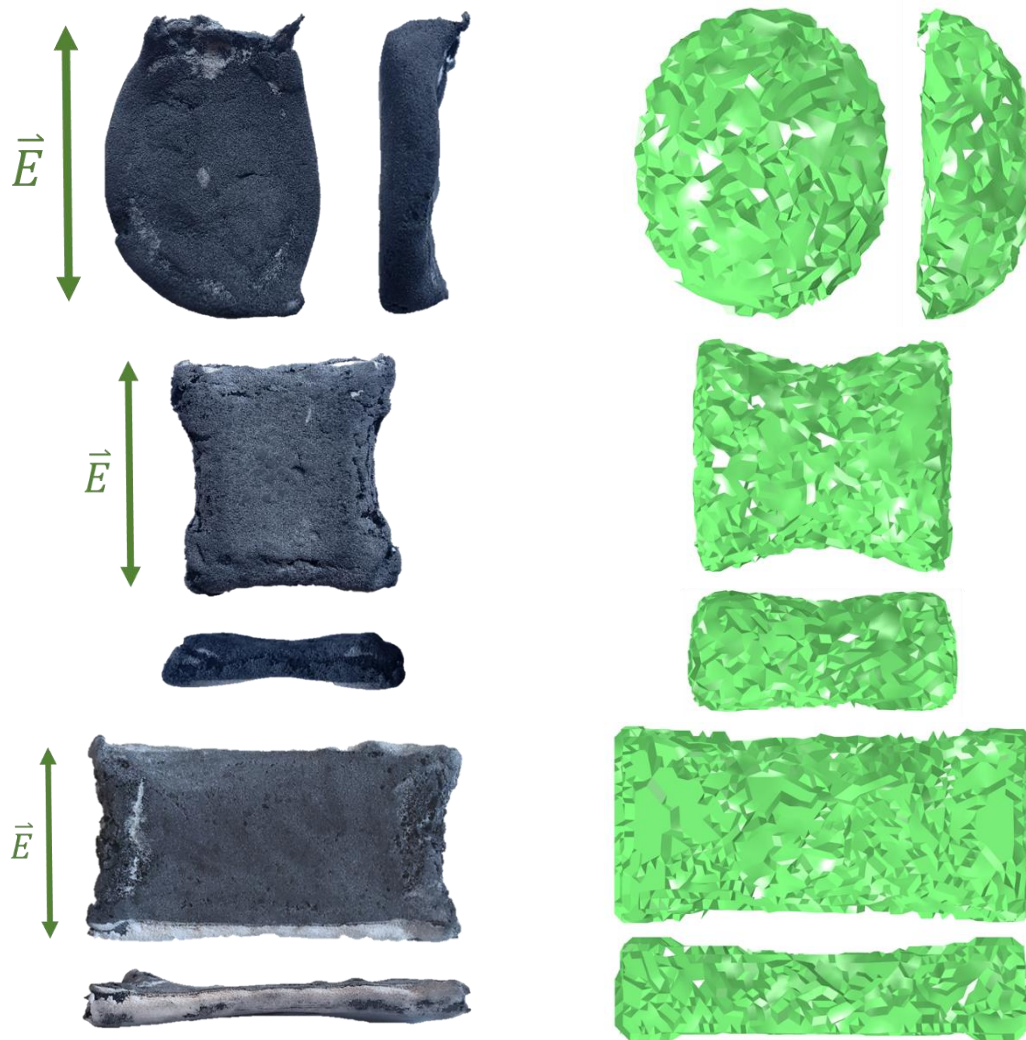


**Figure 4.4** Comparison between experimental (left) and simulated geometry (right) by considering the volume in the liquid phase at the end of the simulation run

The geometric dependence of heating uniformity on the doped geometry must be addressed for the RFAM process to create parts with arbitrary geometries. Previous studies have proposed solutions to improve the heating uniformity in RF applications such as modifying the material and electrode geometries [63] and adding sacrificial material above cold regions to artificially thicken them [65]. In most cases, the electrical properties of the substance being heated are fixed, and the geometry can be modified to some extent to improve heating uniformity. In the case of RFAM parts, the geometry is fixed, but the

electrical properties can be varied by adjusting the amount of dopant throughout the part. In this way, the dopant can be functionally graded within the powder bed. Computational methods are needed to determine the correct grading within the part to improve the heating uniformity.

### **4.3 COMPUTATIONAL APPROACHES TO FUNCTIONALLY GRADE ELECTRICAL CONDUCTIVITY**

The topic of functionally grading materials is an active research endeavor in multi-material AM processes, where two materials are combined in such a way that local flexibility or rigidity can be achieved within a single part [118]. This principle will be adapted for the RFAM process to functionally grade the graphite concentration within the nylon composites to improve the heating uniformity and enable the fabrication of complex structures. The COMSOL® models can be used in a computational design strategy to functionally grade the dopant. The simulations are carried out on a desktop computer with a 3.60 GHz processor, 16 GB of RAM, and 4 core CPU.

#### ***4.3.1 Computational Challenges with Traditional Optimization Techniques***

Topology optimization techniques using the SIMP approach are widely used in structural applications and can be adapted to determine the required grading [119] [120] [121] [122]. These techniques rely on spatial gradients to converge on a solution. Analytical relationships describing the tradeoff between geometry and heating uniformity are unavailable for arbitrary shapes, and so RF problems must be treated as black boxes in which the mapping from input to output is unknown. In the absence of analytical gradients, finite differencing approaches can be used to calculate the gradients at each iteration. However, calculating gradients in a 3D finite element model with the finite differences approach creates an additional computational expense. The number of required function

calls per iteration increases by the number of nodes in the FEA mesh, and the problem quickly becomes intractable.

To illustrate the challenges of traditional optimization, two approaches were taken to improve the heating uniformity. The first approach sought to functionally grade the electrical conductivity to represent varying the dopant concentration. The second approach consisted of modifying the doped geometry with a constant electrical conductivity to achieve uniform heating within the desired geometry. Both methods used the *fmincon* function in Matlab to solve the nonlinear, constrained, multivariable optimization problem.

To enable functional grading, the electrical conductivity was varied spatially throughout the simulated domain. In typical FEA settings, properties are applied to the elements in the mesh, and the results are calculated at the nodes. However, material property definitions in COMSOL® are decoupled from the FEA mesh, and spatial variation of the properties was achieved by assigning unique conductivity values to designated coordinates throughout the domain. COMSOL® then used a linear interpolation scheme between the specified coordinates to assign the properties to the elements when solving. To ensure the electrical conductivities were defined on a similar length scale to the elements in the FEA mesh, the coordinates of the mesh nodes were used as the locations for the property assignment. Although it is uncommon to define properties at nodal locations, the interpolation mechanism in the COMSOL® solver compensated for the discrepancy.

In a normal black box optimization problem, each unique conductivity value defines a different variable to optimize, and so the dimensions of the problem scale with the number of conductivity definitions. To reduce the dimensionality of the problem, cubic smoothing splines were used to define the electrical conductivity at every point within the material volume. The splines enabled the conductivity to be defined by the number of

control points instead of the number of mesh nodes, drastically reducing the number of parameters in the optimization. Figure 4.5 shows a 3D representation of how the conductivity was defined within the geometry for a cube doped region for a 4x4x5 control point grid. To further reduce computational expense, symmetry about the y-axis was applied.

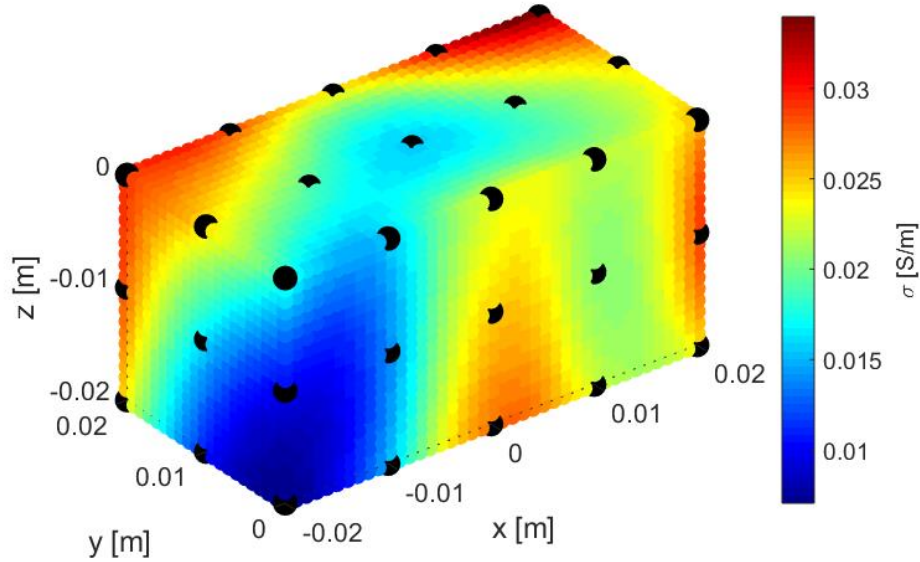


**Figure 4.5** Cubic spline definition of electrical conductivity. The black points represent the control points of the spline. The control points are 4 dimensional where the first three are spatial, and the fourth corresponds to the electrical conductivity.

To optimize the electrical conductivity, the temperature at each mesh node was computed and used to determine the value of the objective function. A penalized norm objective function was used in the optimization, defined by Equation 4.14 where  $n$  represents the number of mesh nodes,  $T_i$  represents the temperature at a given node,  $T_m$  is the average temperature across all mesh nodes, and the exponent  $p$  is used for penalization.

$$f = \sum_{i=1}^n (|T_i - T_m|)^p \quad [4.14]$$

Even with the reduced dimensionality imposed by the spline representation, the optimization required several hours to compute on the desktop computer and failed to

converge on a nontrivial solution. To improve convergence, the number of control points in the spline representation and the control point spacing were varied, and a range of values for the penalization exponent were considered. Gradient-based optimization algorithms can be sensitive to starting conditions, so the initial values of conductivity as well as the finite differencing step size were also varied. The use of splines to define the conductivity assumed an underlying smoothness to the solution, but the failure of the optimization routine to converge on a nontrivial solution suggested the assumption was invalid.

Another attempt at optimization was made by modifying the boundaries of the doped geometry to improve heating uniformity within the desired geometry. Splines were used to define the edges of a square, as depicted in Figure 4.6. The optimization varied the location of the control points to change the geometry. The number of control points of the spline were adjusted as well as the initial configuration, but again the optimization failed to generate a nontrivial solution.

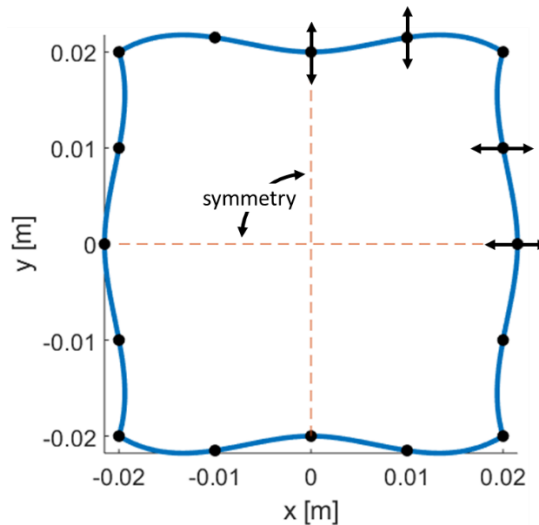


**Figure 4.6** Spline representation of the cubic geometry. The dashed lines represent the lines of symmetry imposed during the optimization. The black points are the control points for the spline, and the arrows represent the direction of movement.

The failure of the optimization methods to find viable solutions was most likely caused by the black box nature of the problem and the reliance on global objective functions to evaluate the performance. The added computational expense from determining the gradients using finite differencing and the failure of the global objective function to capture local effects prevented the optimization from being a practical approach to improving the heating uniformity in RF heating.

#### ***4.3.2 Heuristic Tuning Method***

Instead of using optimization to tune the electrical conductivity, the heating uniformity was improved by applying a heuristic to adjust the conductivity. The basis for the heuristic was that the conductivity should be raised in regions where the local temperature is lower than a specified target temperature and lowered when the temperature is above. The heuristic was validated by performing simulations in COMSOL® in which the electrical conductivity was increased, and the average temperature recorded at the end of the analysis. The normalized temperature rise as a function of electrical conductivity is shown in Figure 4.7. The maximum value for the trend occurred at an electrical conductivity of 0.0425 S/m, after which the temperature rise began to decrease with increasing conductivity. The simulations showed the heuristic to be valid as long as the electrical conductivity was kept below 0.0425 S/m where an increase in conductivity led to an increase in temperature. The RF heating experiments showed a similar trend where the electrical conductivities of the powder mixtures at the peak temperature rise were between 0.0423 S/m and 0.0862 S/m corresponding to graphite concentrations of 32.5% and 35% by weight, respectively.

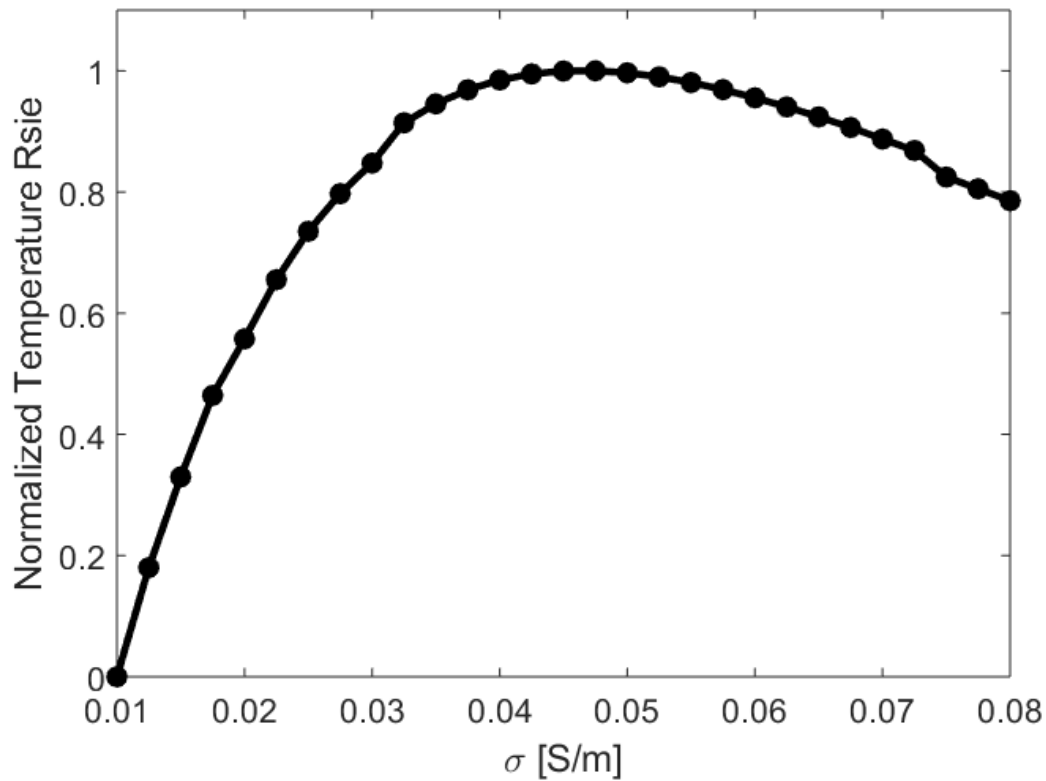


*Figure 4.7 Normalized average temperature as a function of electrical conductivity.*

To functionally grade the electrical conductivity, the heuristic was applied in an iterative scheme at each of the nodal locations in the finite element mesh, and the values were applied to the elements using an internal interpolation algorithm in the COMSOL® solver. The main simplification in the heuristic method was that each mesh node was treated as fully independent from the neighboring nodes. Considering the nodes to be independent, however, enabled the heuristic to be applied at every element simultaneously for a given iteration. In this way, the electrical conductivity was incrementally adjusted at each mesh node location after a single function call to the finite element simulation. By comparison, optimization using finite differencing would have required  $n+1$  function calls for  $n$  mesh nodes in a given iteration to tune the conductivity.



Starting with uniform electrical conductivity, the conductivity for the next iteration was adjusted based on the current node temperature relative to a target temperature. A flowchart of the heuristic tuning procedure is shown in Figure 4.8, and the heuristic is defined in Equation 4.15. For a given iteration, the temperature at each mesh node (denoted by  $i$ ) was queried, and the conductivity was adjusted according to Equation 4.15. The size of the adjustment was determined by the proportionality constant ( $K_i$ ) and the difference between the nodal temperature and target temperature ( $\Delta T_i$ ). The temperature difference term was normalized to the maximum observed difference ( $\Delta T_{max}$ ), penalizing nodes with larger errors by applying a stronger correction. The sign of  $\Delta T_i$  implicitly accounted for the direction in which the heuristic was applied by reducing the conductivity when the target temperature was greater than the nodal temperature. If the temperature at a given node passed through the target temperature between iterations, indicated by a sign reversal in  $\Delta T_i$ , the proportionality constant at the node was halved for the next iteration. In this way, the nodal temperature converged on the target temperature. The heuristic tuning procedure was repeated until either the maximum number of iterations was met or the maximum temperature difference fell below a predetermined threshold.

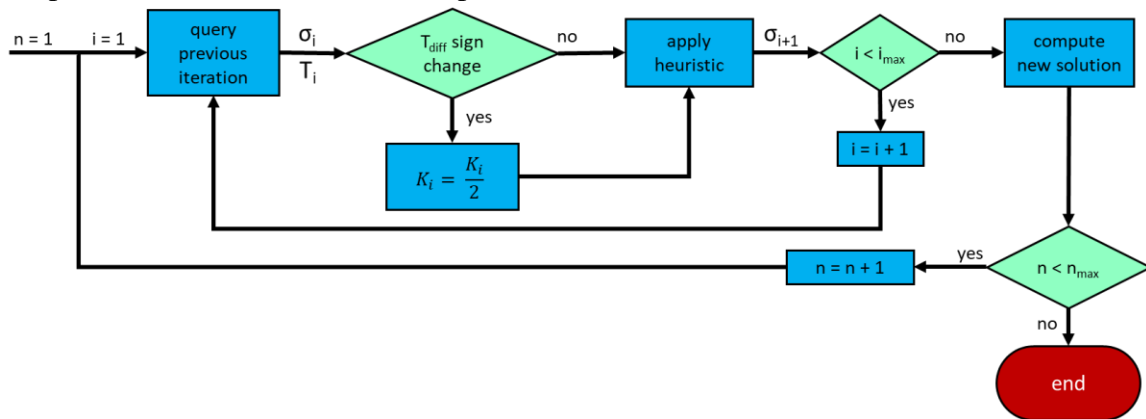


**Figure 4.8** Flowchart describing how the heuristic tuning method was applied to the simulation results. The variables  $n$  and  $n_{max}$  represented the current and maximum iteration, while  $i$  and  $i_{max}$  corresponded to the current and maximum number of nodes. The proportionality constant,  $K$ , was uniquely assigned to each node for every iteration.

$$\sigma_{i+1} = \sigma_i + K_i * \frac{\Delta T_i}{\Delta T_{max}} \quad [4.15]$$

$$\Delta T_i = T_{target} - T_i \quad [4.16]$$

$$\Delta T_{max} = \max(T_{target} - T_i) \quad [4.17]$$

While the heuristic tuning method did not guarantee optimal solutions, the computational expense was dramatically reduced compared with SIMP methods by eliminating the need to calculate gradients at each iteration. In most cases, the tuning procedure converged on a solution after only 15 function calls to the COMSOL® simulation, making the process tenable on a standard desktop computer.

The uniformity index was used to evaluate the effectiveness of the tuning process. The index, defined in Equation 4.18, considers the temperature difference across the entire part volume and is useful for making direct comparisons for a given model configuration [123]. An initial temperature ( $T_{initial}$ ) of 20°C was prescribed in the calculations, and the remaining quantities were computed in COMSOL® using a fourth order numerical integration technique across the FEA nodes.

$$UI = \frac{\frac{1}{V} \int_V \sqrt{(T - T_{av})^2} dV}{T_{av} - T_{initial}} \quad [4.18]$$

Smaller values of the index indicate greater heating uniformity with a minimum value of zero to signify no temperature differences across the domain. The uniformity index calculations were carried out within the COMSOL® models and were restricted to the doped region only.

Before applying the heuristic tuning method, a convergence study was carried out to measure the effect of element size on the uniformity index in the FEA simulations. COMSOL® generated the mesh using five independent parameters that governed the element size, and the values of the parameters were sorted into different categories of mesh

refinement ranging from coarse to fine. To reduce the computational expense, the powder bed was given a coarser mesh than the doped region. This was a valid assumption when determining heating uniformity because uniformity index was calculated for the doped region only. The convergence study was conducted with a square prism geometry using tetrahedral elements to define the mesh. The element size of the powder bed was constant, while the elements in the doped region were varied according to the mesh size categories determined by COMSOL®. The uniformity index as a function of element size is shown in Figure 4.9. The x axis represents the inverse of the maximum element size, where higher values correspond to a finer mesh.

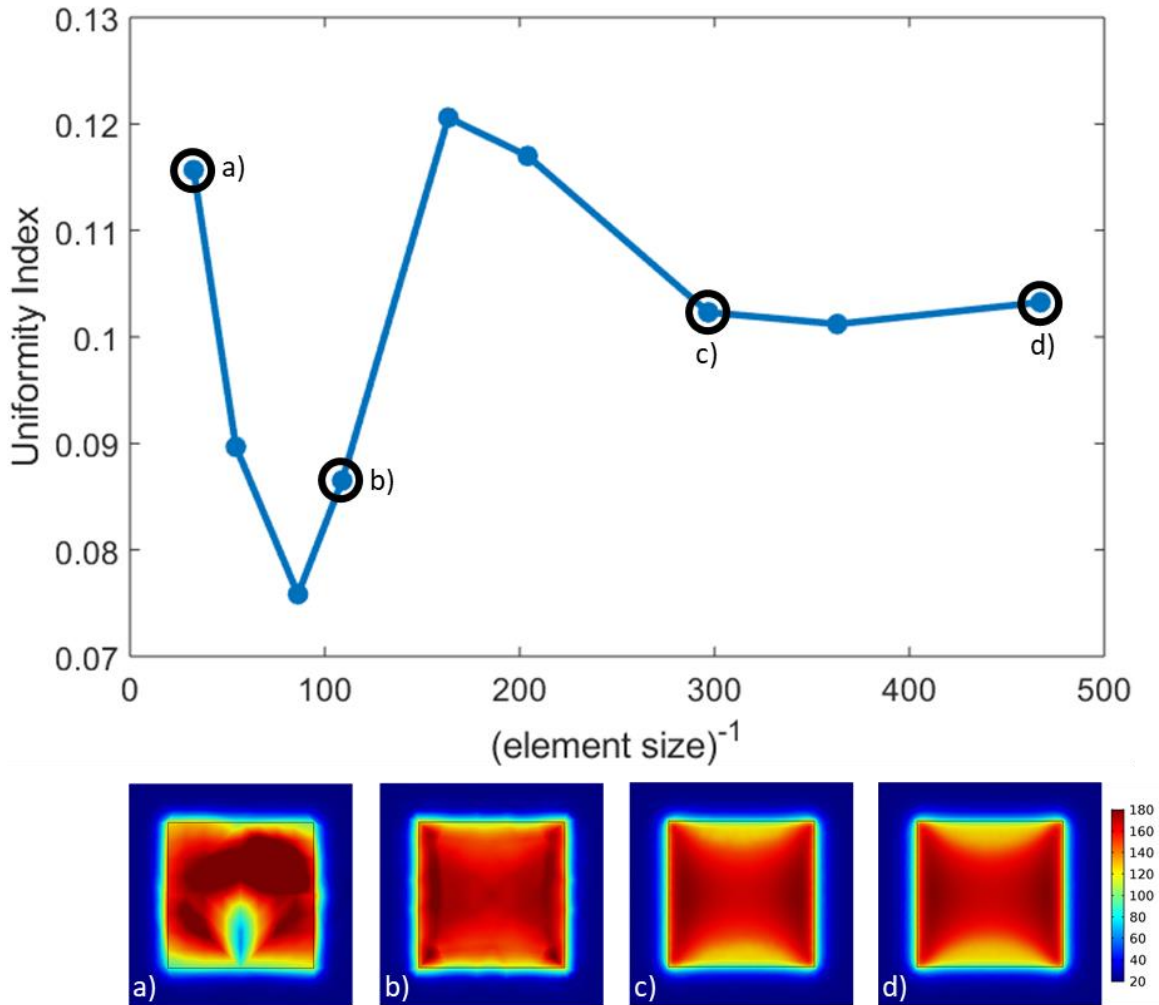


**Figure 4.9** Mesh convergence for square prism. The x axis is the inverse of element size, and so higher values represent a finer mesh.

The convergence study revealed large variations in the uniformity index for coarse meshes that stabilized as the mesh was refined. To balance computational time and model accuracy, the mesh size category corresponding to point c) in Figure 4.9 was used for the heuristic tuning simulations. The convergence study was intended to validate the meshing procedure in COMSOL®, which used internal algorithms to optimize the five sizing parameters for a given refinement category. Different geometries may lead to different values for the five parameters.

The heuristic tuning method was applied to three geometries: a square prism, an equilateral triangular prism, and a thin ring. The simulated domains are shown in Figure 4.10 where the electrode locations with respect to the doped geometries are marked in purple. The dimensions of the chamber are 6.24x6.24x2.0 cm, and the dimensions of the different geometries are given in Figure 4.10. The model results were processed in a Matlab script that tuned the electrical conductivity at each iteration and ran the COMSOL® simulations using the *LiveLink for Matlab* tool. To start the tuning process, a constant electrical conductivity of 0.0425 S/m was prescribed to the doped region because it was associated with the highest degree of heating in the COMSOL® models.

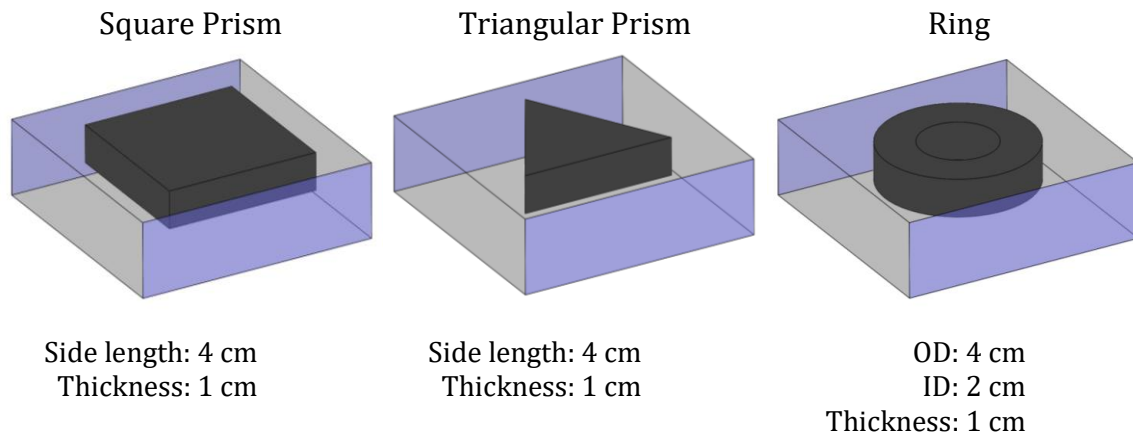


**Figure 4.10** Simulated geometries used in the heuristic tuning method. The dark regions represent the doped geometry where the tuning was applied, and the location of the electrodes with respect to the geometry are indicated in purple. The dimensions of the chamber are 6.24x6.24x2.0 cm.

The maximum value of conductivity was prescribed as the initial conditions in the functional grading simulations, and so the process of tuning necessarily reduced the total effective conductivity within the part. For this reason, the tuned parts required a longer RF exposure time to compensate for the reduction in the effective conductivity relative to the un-tuned, constant conductivity case. Figure 4.11 shows the predicted geometry, simulation RF exposure time, and uniformity index for the constant electrical conductivity

case (left) and functionally graded conductivity (right) for the square prism. The tuning process was performed for 7 iterations completed in 553 seconds. The uniformity index was improved from 0.135 in the case of constant conductivity to 0.083 for the functionally graded conductivity. The predicted geometry also showed improvement after functional grading, where the curvature was reduced on the top and bottom faces.

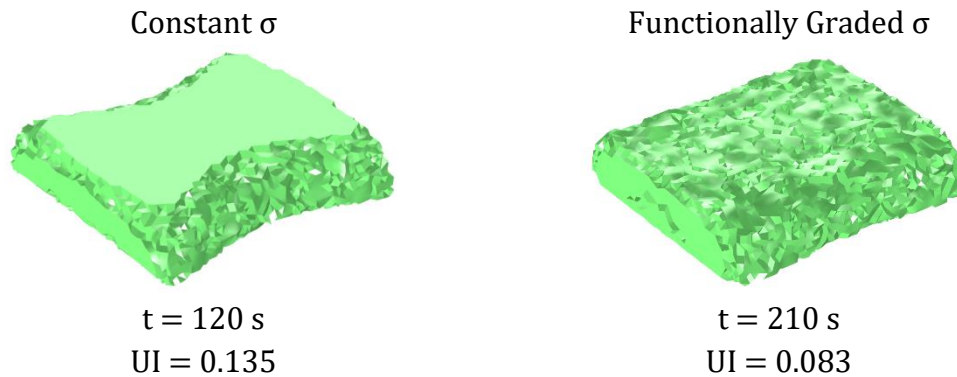


**Figure 4.11** Comparison between constant conductivity (left) and functionally graded conductivity (right) for a 4x4x1 cm square prism, where  $t$  represents the simulated RF exposure time and UI is the uniformity index.

In a similar fashion, the tuning process was carried out for an equilateral triangle prism with a side length of 4 cm and depth of 1 cm. The comparison between the constant conductivity and functionally graded conductivity cases is given in Figure 4.12. For a constant conductivity, the electric field concentrated at the corner facing the electrodes and caused the region to sinter beyond the doped region. The uniformity index was improved from 0.262 to 0.094 after functionally grading the conductivity. The results are shown after 15 iterations of the heuristic tuning process and required 385 seconds to complete.

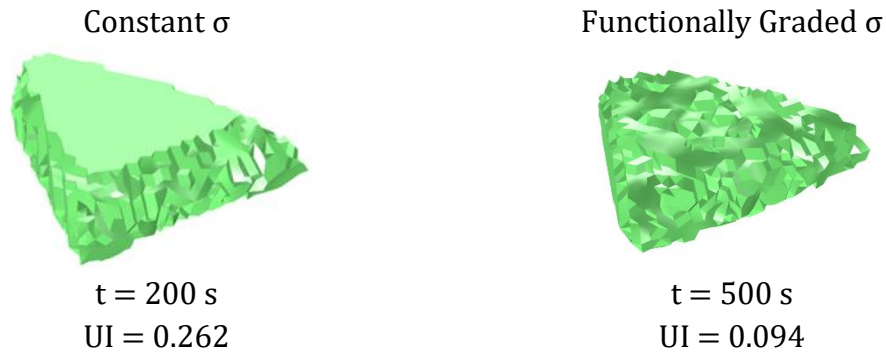


**Figure 4.12** Comparison between constant conductivity (left) and functionally graded conductivity (right) for a triangular prism with a side length of 4 cm and 1 cm thickness, where  $t$  represents the simulated RF exposure time and UI is the uniformity index.

The heuristic tuning procedure was also tested on a thin ring with an inner radius of 1 cm, outer radius of 2 cm, and thickness of 1 cm. The comparison between the un-tuned and functionally graded electrical conductivities is shown in Figure 4.13. The geometry predictions showed substantial sintering in the sides of the ring in the direction of the applied electric field, and no sintering in the top and bottom regions for the constant conductivity case. After 15 iterations of functionally grading the electrical conductivity and 811 seconds of computational time, the uniformity index was improved from 0.263 to 0.077. Further, the geometry predictions for the tuned conductivity showed the formation of a single ring as opposed to the two separate sintered regions suggested by the constant doping simulation.

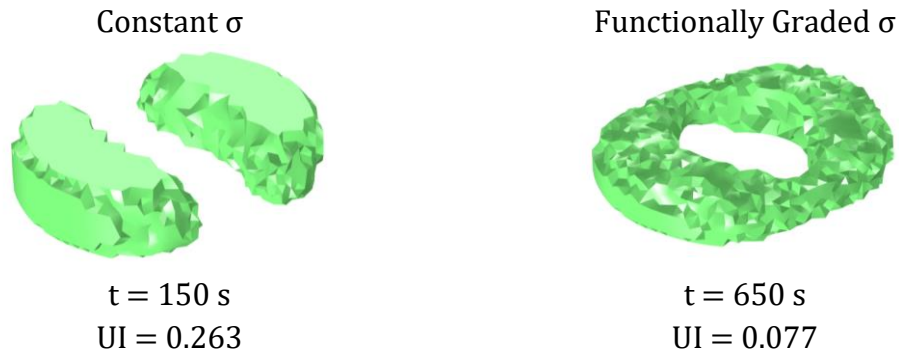


**Figure 4.13** Comparison between constant conductivity (left) and functionally graded conductivity (right) for a 4 cm outer diameter, 2 cm inner diameter, and 1 cm thick ring, where  $t$  represents the simulated RF exposure time and UI is the uniformity index.

The functionally graded electrical conductivity distribution within the parts can provide additional insight into the interaction between the electric field and the doped geometry. Figure 4.14 shows the graded electrical conductivity at the center cross section of the square prism located 0.5 cm from the top and bottom faces. A majority of the tuning occurred along the perimeter of the doped region, while the conductivity did not vary significantly throughout the interior. The tuned conductivity in the interior was also notably low and nearly zero in most areas. The top and bottom regions were prescribed the highest conductivity, corresponding to the cold spots in the un-tuned case.

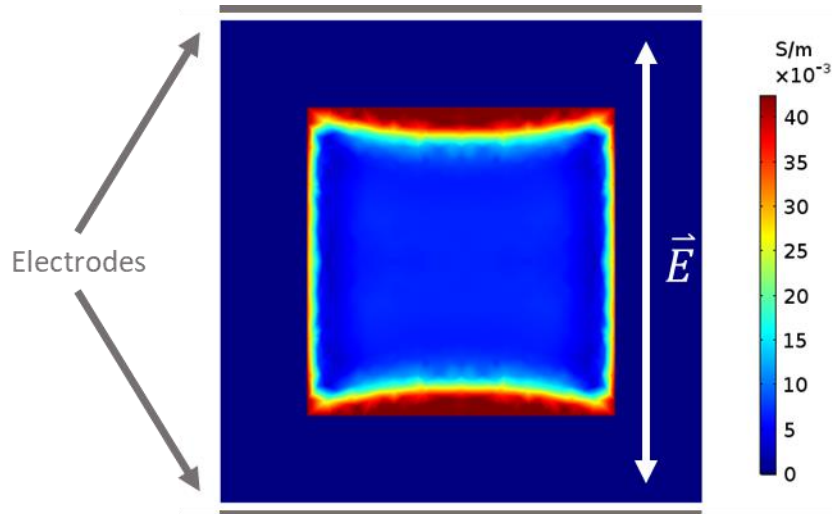


**Figure 4.14** Spatially tuned conductivity for a 4x4x1 cm square prism at the center cross section.



The functionally graded conductivity at the center cross section of the triangular prism is shown in Figure 4.15. Similar to the square prism, the conductivity throughout the interior was nearly zero, and most of the tuning was concentrated around the perimeter. In the constant doping case, the electric field concentrated at the corner facing the electrodes which caused a sharp increase in the temperature. In response, the conductivity was reduced in the upper corner and increased in the other two corners during the functional grading process.

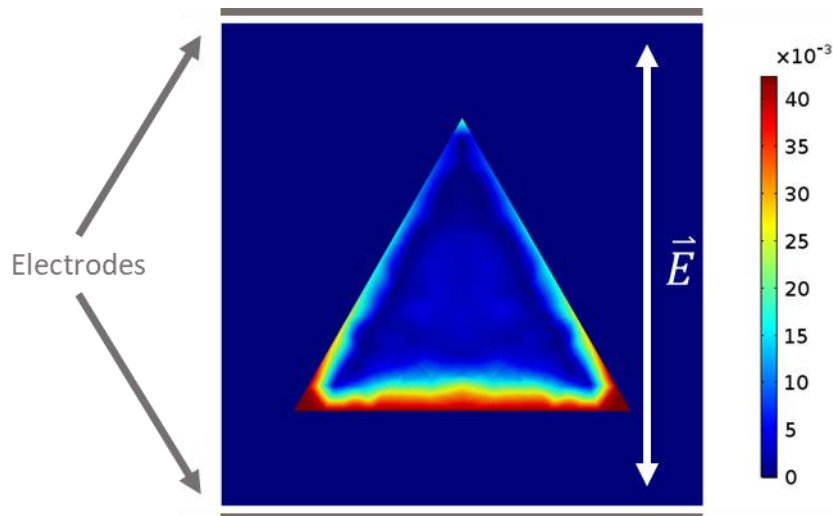


*Figure 4.15 Spatially tuned conductivity for a triangular prism with a side length of 4 cm and depth of 1 cm at the center cross section.*

Lastly, the functionally graded conductivity at the center cross section of the thin ring is given in Figure 4.16. The results were consistent with the previous two cases in which the conductivity within the interior was greatly reduced compared to the edges. The highest conductivity was prescribed to the top and bottom regions where the un-tuned predicted geometry showed a lack of fusion.

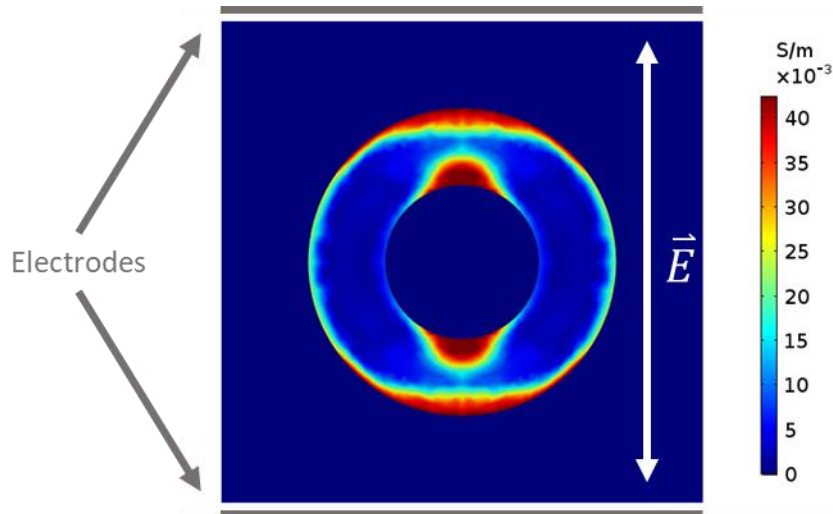


**Figure 4.16** Spatially tuned conductivity for a 4 cm outer diameter, 2 cm inner diameter, and 1 cm thick ring at the center cross section.

The distribution of the electrical conductivity in the functionally graded geometries highlighted the need for computational approaches to improve the heating uniformity and provided an explanation for the failure of the traditional optimization techniques to find a nontrivial solution. The steep gradients in the tuned electrical conductivity at the boundaries disproved the underlying assumption of smoothness imposed by the cubic spline representation of conductivity in the optimization attempts. The heuristic tuning method did not make an assumption of smoothness but sacrificed the guarantee of finding optimal results. However, the results of the heuristic tuning method demonstrated the effectiveness of spatially varying the electrical conductivity as a means of improving the geometrically-induced heating uniformity issues in RF heating applications. The computational expense of the heuristic tuning procedure was greatly reduced compared to traditional optimization techniques making it a viable option for functionally grading the dopant in RFAM parts.

### 4.3.3 Changing Electrode Configuration to Improve Heating Uniformity

In addition to functionally grading the electrical conductivity, modifying the electrode configuration was considered to improve the heating uniformity in the RF heating simulations. Birla et al. showed that rotating material with respect to the electric field in an RF applicator improved the heating uniformity in fruit [124]. However, simulating a rotating electric field can be difficult because the boundary conditions must also change at each time step [61]. Therefore, instead of modelling a continuously rotating powder bed, a two-stage heating process was chosen in which the electrode configuration was modified sequentially during the simulation. The two-stage process consisted of activating opposing pairs of electrodes by changing the boundary conditions in the simulation as shown in Figure 4.17 for the thin ring. A portion of the simulation was conducted using the first configuration then switched to the second configuration for the remaining time steps.

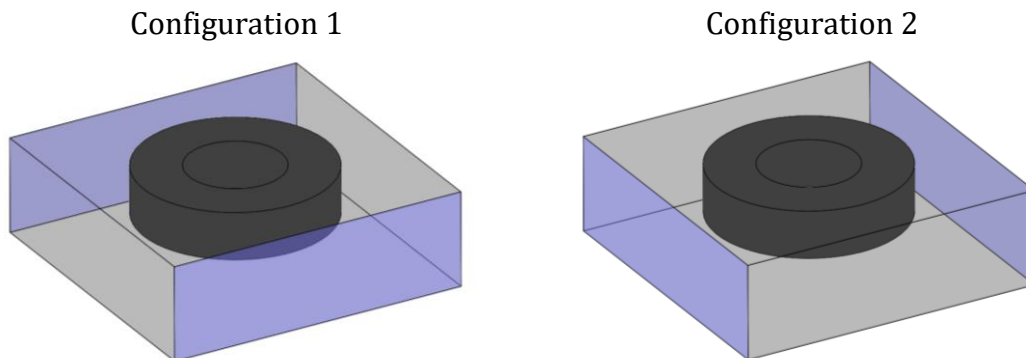


*Figure 4.17 Electrode configurations for orientation-dependent simulations of a thin ring*

Figure 4.18 shows the effect of applying multiple electrode configurations to the thin ring. The electrodes were activated for 75 seconds in the first configuration followed by 45 seconds in the second configuration. The heating times were asymmetrical because regions that were predominately heated in the first configuration began to cool as the second configuration was applied. The uniformity index for a constant electrical conductivity and single electrode configuration was 0.263 and improved to 0.109 with the

two-stage process. The heating uniformity for multiple electrode configurations and a constant doping nearly matched the functionally graded uniformity index of 0.077 without implementing an iterative computational design strategy.

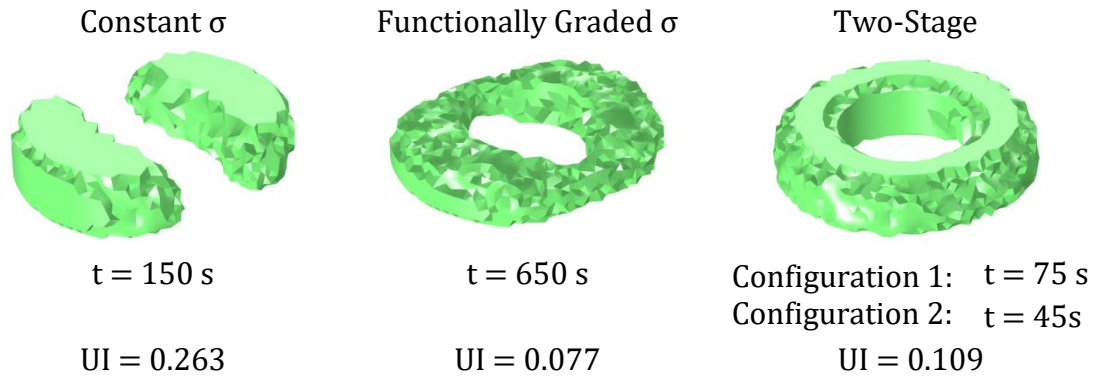


**Figure 4.18** Predicted geometry and uniformity index calculations for a thin ring in a single electrode configuration with constant electrical conductivity (left), single electrode configuration with functionally graded electrical conductivity (middle), and constant electrical conductivity with multiple electrode configurations (right)

With the successful application of the two-stage heating method on the thin ring, the process was tested on a more complex geometry. With a large aspect ratio and detailed features, a longhorn head was selected as the representative geometry. The two electrode configurations used in the simulations are shown in Figure 4.19.

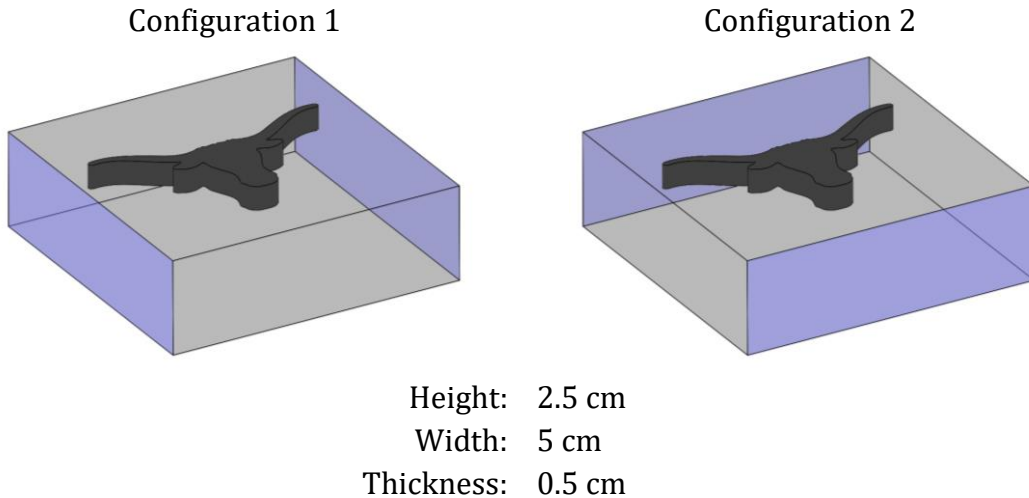


**Figure 4.19** Electrode configurations for orientation-dependent simulations of a longhorn head. The height, width, and thickness correspond to the bounding dimensions of the longhorn head geometry.

Figure 4.20 shows the predicted geometries and uniformity index values for each electrode configuration as well as the combined two-stage case. For the first configuration, nearly all the fusion occurred in the horn region, while the predicted geometry for the second configuration showed fusion only in the head region. By implementing the two-stage process, the effects of the individual configurations were superimposed to produce a closer resemblance to the desired geometry. The uniformity index in the combined case was only slightly lower than in the second configuration but captured more detail in the predicted geometry. The smaller degree of heating in the horn region for configuration 2 had less of an effect on the uniformity index because the horns made up a smaller proportion of the part volume. The two-stage heating process improved the heating uniformity for the longhorn, but it was unable to resolve some of the finer details and curvature present in the desired part.

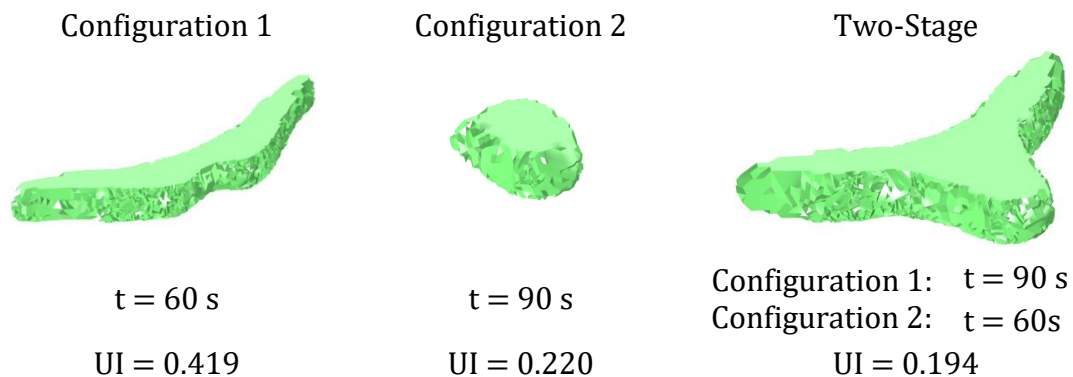


**Figure 4.20** Predicted geometry and uniformity index for longhorn head simulations in each electrode configuration as well as the two-stage combined configuration.

The two-stage heating results showed the predicted geometry and heating uniformity can be improved by rotating the powder bed with respect to the electrodes. For the thin ring simulation, the heating uniformity was close to the functionally graded case and did not require multiple function calls to the finite element simulation. Two-stage heating of the longhorn head highlighted the effectiveness of the process where the

predicted geometry for the combined configurations resembled a superposition of the two individual configurations. For certain geometries, two-stage heating could improve the resolution of RFAM parts without the need to functionally grade the powder bed.

#### ***4.3.4 Multiple Electrode Configurations to Ease Functional Grading Effort***

Implementing a two-stage heating approach improved the uniformity index for uniformly doped geometries. Subsequent simulations were conducted to evaluate whether the uniformity index could be reduced further by combining the two-stage heating process with the heuristic tuning method to functionally grade the electrical conductivity. A diamond geometry with a side length of 3 cm and thickness of 1 cm was chosen to test combined effects, and the electrode configurations are illustrated in Figure 4.21. The diamond geometry was selected because the vertices were oriented towards the electrodes in both configurations, increasing the likelihood of electric field concentrations and non-uniform heating.

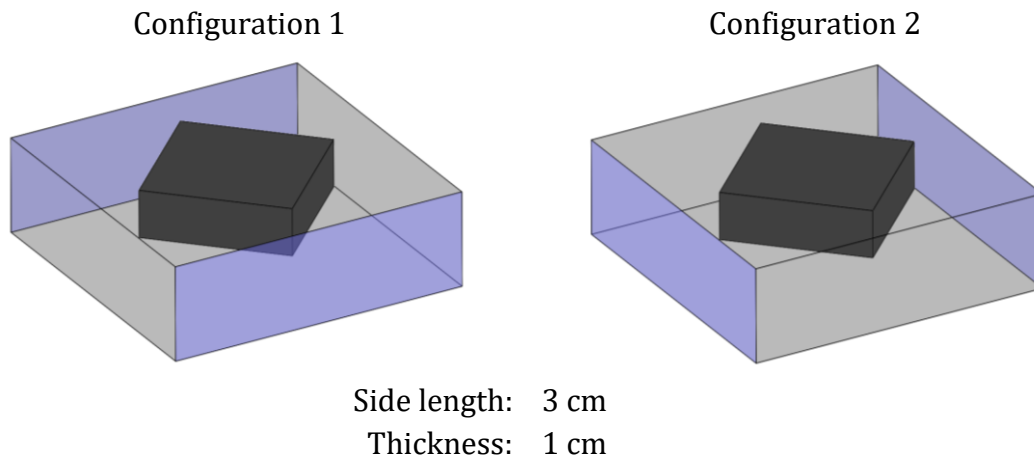


**Figure 4.21** *Electrode configurations for orientation-dependent simulations of a diamond*

To establish a baseline, the first configuration was used in the heuristic tuning process. The uniformity index for a constant electrical conductivity and single electrode

configuration was 0.161. Functional grading with the electrodes in the first configuration improved the uniformity index to 0.125, as shown in Figure 4.22.

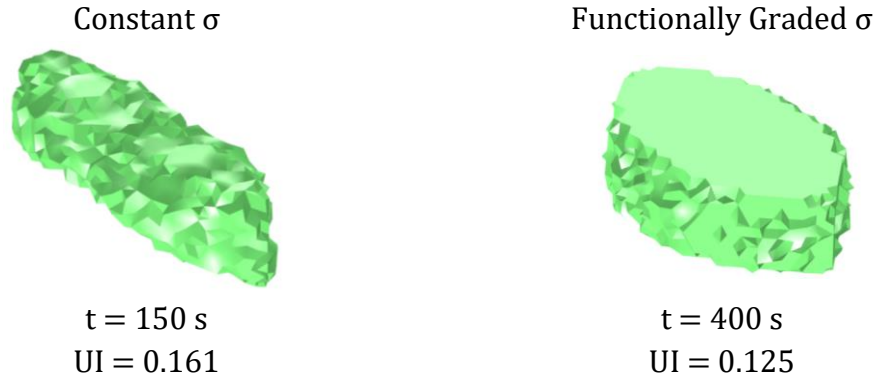


*Figure 4.22 Predicted geometry and uniformity index for single electrode configuration heating and functional grading for the diamond geometry*

Next, the two-stage heating mechanism was applied, and the functional grading process was repeated. The heuristic tuning method did not need to be adjusted to accommodate the two-stage heating because the finite element simulation was treated as a black box with the electrical conductivity values at the mesh nodes as inputs and final temperature distributions as outputs. The predicted geometries and uniformity index values for the constant and functionally graded conductivities are given in Figure 4.23. Two-stage heating improved the uniformity index compared with the single stage results even after functional grading. The lowest value for the uniformity index was achieved by combining the effects of multiple electrode configurations and heuristic tuning.

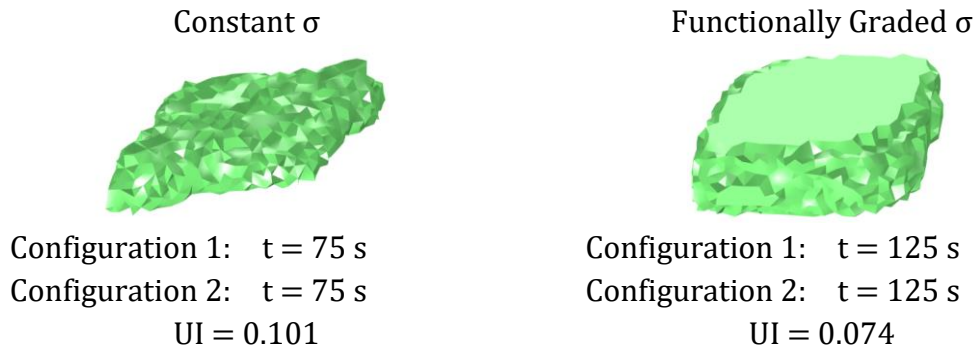


**Figure 4.23** Predicted geometry and uniformity index for multiple electrode configurations and functional grading for the diamond geometry

The functionally graded electrical conductivity distributions at the center cross section for the single-stage and two-stage electrode configurations are shown in Figure 4.24. For the single-stage process, very little heating occurred along the sides of the diamond, and the electrical conductivity was tuned to its maximum value in those regions. The pattern for the two-stage process was noticeably different, and the majority of the tuning occurred around the perimeter. As demonstrated in the conductivity distributions and the uniformity index values, functional grading with multiple electrode configurations was the most effective method for improving the heating uniformity in the RF simulations.

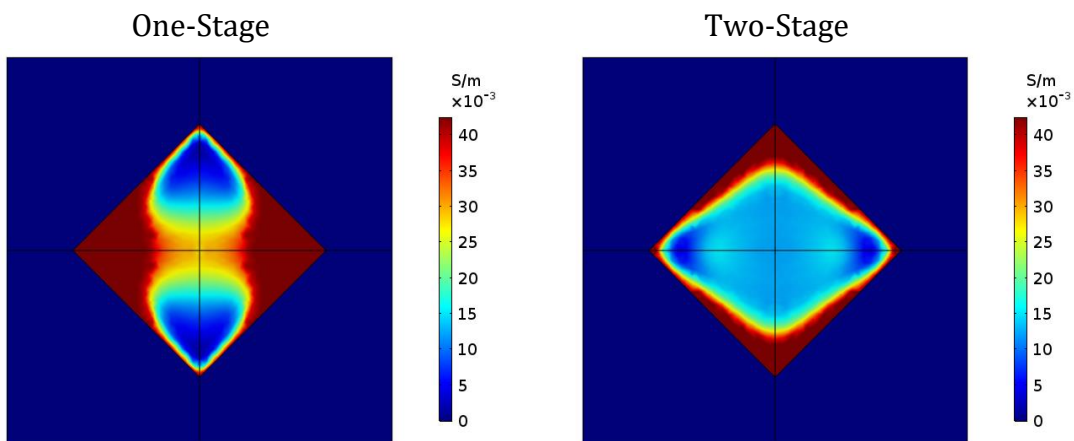


**Figure 4.24** Spatially tuned conductivity for the diamond geometry with the electrodes in the first configuration (left) and multiple configurations (right)



#### 4.4 CLOSURE

Finite element analysis simulations in COMSOL Multiphysics® enabled the prediction of temperature rise and phase change behavior of the doped powder beds in RFAM. The models were used to show the electric field concentrations within non-spherical geometries that led to thermal gradients within the parts. Geometrically-induced non-uniform heating was responsible for the unintended curvature seen in the parts produced in the RF heating experiments. A computational design strategy using the COMSOL® FEA models was proposed to improve the heating uniformity by functionally grading the electrical conductivity throughout the doped region. The electrical conductivity was spatially graded by applying a heuristic to adjust the conductivity values at every node in the FEA mesh in an iterative process. The design strategy was evaluated according to the relative change in the uniformity index before and after tuning. An alternative method to improve the heating uniformity was demonstrated by modifying the electrode configuration during the simulations. Lastly, the two methods were combined to produce the greatest effect on heating uniformity. In order to manufacture the functionally graded parts for the RFAM process, a system for spatially patterning the dopant in different concentrations is required. The following chapter focuses on the design of a dopant deposition mechanism capable of defining the geometries on a layer-by-layer basis with spatially varying dopant concentrations.

## **Chapter 5: Design of a Dopant Delivery Mechanism for RFAM**

Previous chapters have demonstrated the feasibility of RFAM by showing how graphite-doped nylon powders can be fused by exposing them to RF radiation. A method for improving the heating uniformity for different geometries was proposed, and the theoretical improvements were evaluated using computational models developed in COMSOL Multiphysics®. While the benchtop fusion experiments and FEA simulations were useful in establishing the viability of volumetric sintering, additional work is required before RFAM can be considered a manufacturing process. Towards that end, a mechanism for patterning the dopant and functionally grading the powder bed are important considerations in the development of the process. In this chapter, requirements for the RFAM process are discussed as well as two methods for delivering the dopant to the nylon powder bed.

### **5.1 SYSTEM REQUIREMENTS FOR THE RFAM PROCESS**

The functional requirements of a radio frequency additive manufacturing system involve the coordination between three main components. A mechanism for patterning the dopant is needed to define the geometry of the parts. The powder bed consisting of the doped and virgin powder regions should be contained within a build chamber. Lastly, the system must include a means of supplying RF radiation to the powder bed. The RFAM process is established through the cohesive integration of the three subsystems.

#### ***5.1.1 Dopant Delivery Requirements***

The mechanism for defining the doped geometry is perhaps the most critical of the three components as it determines the minimum spatial resolution of the final parts. The primary task of the delivery mechanism is to precisely deposit controlled volumes of dopant throughout the powder bed. It should be capable of patterning three dimensional

geometries at a temperature that is low enough to ensure fusion does not take place. To create complex geometries, the powder bed should be self-supporting, meaning the entire volume is occupied by either doped powder or virgin powder. For this reason, the dopant should be delivered on a layer-by-layer basis as with other powder bed fusion processes such as binder jetting, selective laser sintering, and multi jet fusion. The speed of dopant delivery is another important parameter in reducing the processing time of RFAM parts over other AM methods. Finally, based on the computational models shown in the previous chapter, functional grading of the dopant within the powder bed may be necessary to improve the geometry of RFAM parts. Therefore, the dopant delivery system must be able to deposit variable dopant concentrations throughout the powder bed. The method of using forms to define the geometry for the RF fusion experiments in Chapter 3 not only was limited to simple prismatic shapes, but also was capable of delivering only constant dopant concentrations. Spatial grading of the dopant is necessary to validate the computational design strategy from the previous chapter and demonstrate improved geometric resolution from functionally grading the dopant in the powder bed.

### ***5.1.2 Build Chamber Requirements***

The build chamber in radio frequency additive manufacturing serves two functions. In addition to containing the powder bed, the volume of the chamber should be expandable to support the repeated deposition of thin powder layers. The material used to form the build chamber is particularly important in the context of RFAM because the entire chamber and powder bed are subjected to RF radiation. Therefore, the build chamber should be made of an RF-transparent material because any energy absorbed by the chamber walls would detract from the power available to heat the doped powder. Further, if the dopant is to be defined on a layer-by-layer basis, the chamber must accommodate layer spreading by changing volume throughout the build process. In typical powder bed fusion additive

manufacturing systems, the build chamber functions as a piston such that its base lowers into the chamber as new powder layers are spread across the surface. A similar architecture could be implemented for RFAM.

### ***5.1.3 RF Generator Requirements***

The final component of a radio frequency additive manufacturing system is the RF generator and applicator that together supply radiation to the powder bed. There are a variety of RF generators ranging from small-scale to industrial-sized equipment. The initial fusion experiments showed that it is possible to heat nylon mixtures to their melting temperature using a comparatively small 560 W RF generator. Higher power output could enable the production of larger parts. Industrial systems are manufactured with power ratings as high as 20 kW, but the size and cost of such systems would outweigh their benefit in an RFAM application [45]. To maximize the efficiency of heating, the RF generator should have a tuning circuit to ensure proper coupling between the source impedance and the load. In addition to the RF generator, the design of the applicator is an important consideration for the RFAM process. Namely, the spacing of the electrodes should be variable to improve the RF coupling characteristics of the system for parts that have different sizes [31]. The size of the electrodes is another important factor in the applicator design. The electrodes should be larger than the sample so that the electric field incident on the sample is as uniform as possible. The sample should also be placed in the center of the applicator to avoid fringing effects at the edges of the electrodes where the electric field is curved.

In developing a volumetric radio frequency additive manufacturing process, the design of the dopant delivery mechanism, build chamber, and RF components are important considerations. In an ideal RFAM system, the three components would interact as a single unit with minimal human intervention. The first step towards realizing a full-

fledged RFAM machine is establishing the mechanism for patterning the dopant and integrating it with the existing experimental RF equipment. The rest of this chapter introduces two possible methods for delivering the dopant in an RFAM application. The first system consists of depositing pre-mixed doped powders to define the geometry. The second system uses an inkjet print head to deliver the dopant as a nanoparticle ink into the powder bed.

## 5.2 DESIGN OF A POWDER DEPOSITION SYSTEM

After demonstrating RF fusion of the nylon 12/graphite mixtures, a system for spatially patterning the dry powders was devised. A prototype machine was developed by retrofitting a MakerBot Replicator 2 material extrusion AM machine. The prototype system is shown in Figures 5.1 and 5.2 with the critical components labeled.



*Figure 5.1* MakerBot Replicator 2 modified to pattern doped dry powders. The 3 axes of movement and their respective stages are labeled.

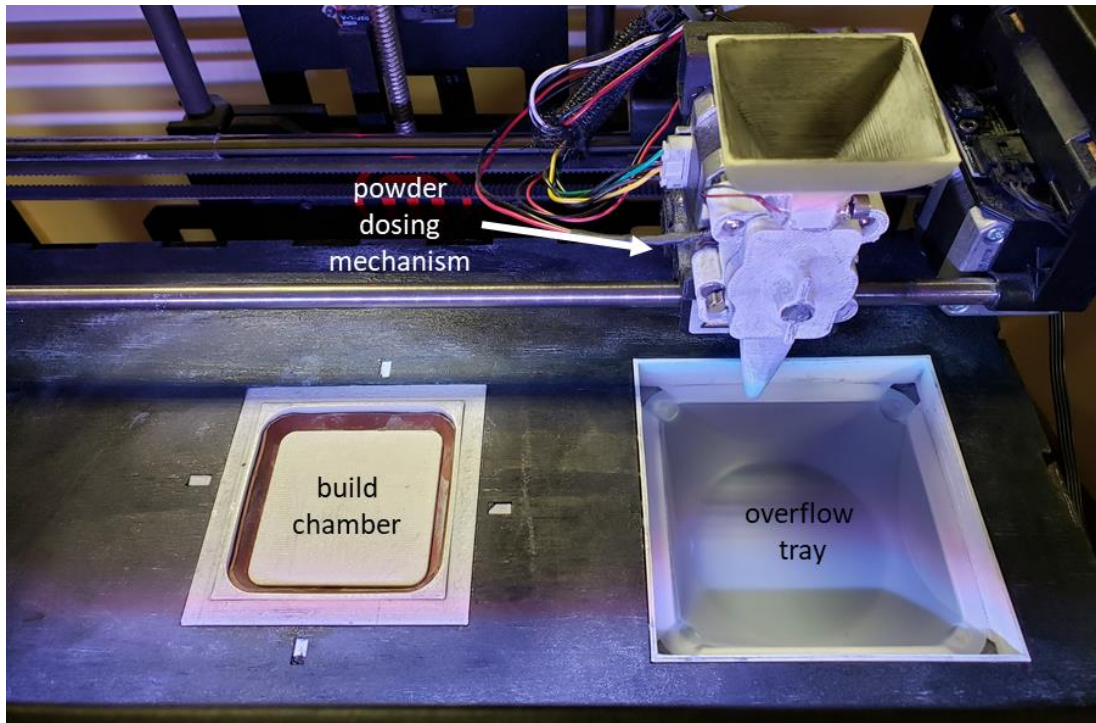


*Figure 5.2* Build area showing the powder dosing mechanism, build chamber, and overflow tray

### **5.2.1 Powder Dosing Mechanism**

Patterning of doped powders was accomplished by replacing the filament extruder and heating elements on the MakerBot system with a powder deposition mechanism. The mechanism, shown in Figure 5.3, was capable of dispensing individual volumes of doped powder and was powered by the existing stepper motor previously used to extrude the filament in the MakerBot. The dosing wheel containing 30 cavities was connected to the stepper motor. The doped powder was placed in the hopper above the wheel housing and gravity-fed through the mechanism. The cavities in the dosing wheel were filled with doped powder, and the wheel was rotated by the stepper motor. Discrete volumes of powder were deposited by advancing the wheel by 36 degrees corresponding to the sector angle of one cavity and allowing the powder to exit through the nozzle. Since the powder needed to travel from the top region of the dosing wheel to the bottom where the nozzle was located,

it was necessary to prime the mechanism by rotating it by at least one half of a revolution before patterning the dopant.

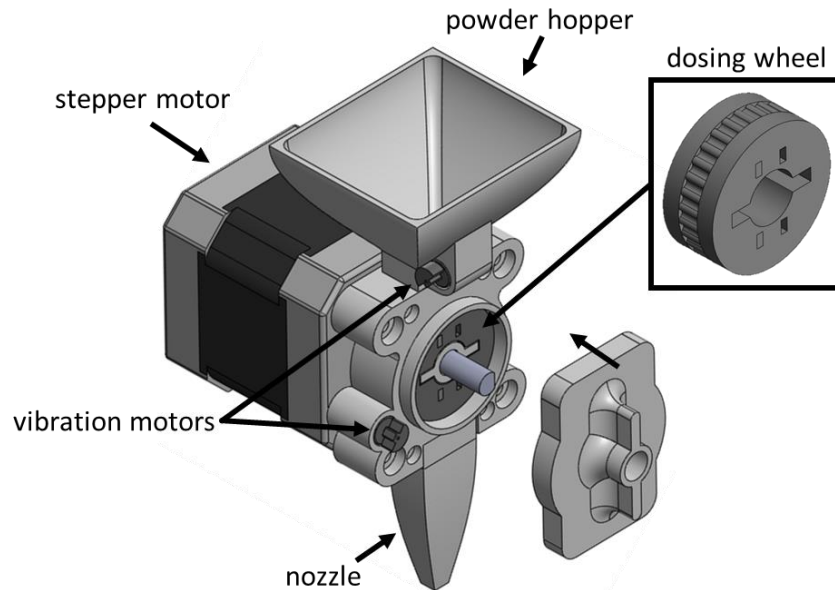


*Figure 5.3 Dosing mechanism for depositing discrete volumes of doped powder*

Early design iterations of the dispensing mechanism revealed the tendency of the doped powders to resist flowing from the hopper to the dosing wheel. For this reason, two eccentric rotating mass vibration motors were added to the hopper and housing to agitate the powders and promote flow through the mechanism. The location of the vibration motors was chosen to be as close to the entry and exit points on the dosing wheel as possible. The components of the dosing mechanism were created on a material extrusion AM machine in PLA plastic. Figure 5.4 shows the final design of the dosing mechanism as it was installed on the patterning machine. The mechanism was attached to a carriage on the MakerBot machine that restricted its motion to the x and y axes through motor-controlled stages in a gantry-style system.

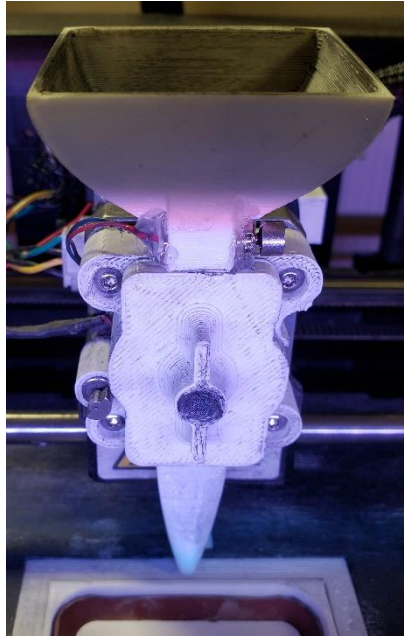


*Figure 5.4 Powder dispensing mechanism as implemented in the final design of the patterning machine*

### **5.2.2 Build Chamber Design**

The build chamber was designed to be removable and interchangeable so that the doped powder beds could be transported to the RF generator and placed between the electrodes for heating. The base of the chamber also needed to move relative to the walls to accommodate layer-wise powder deposition. An additional restriction on the design of the chamber was that all components needed to be manufactured from electrically insulating materials to avoid disturbing the electric field during the RF heating stage.

To enable the deposition of multiple layers, the MakerBot build plate was removed, and the base of the chamber was rigidly attached to the z axis carriage through a piston rod. The base was positioned inside four walls that were held in place by a wooden stand as depicted in Figure 5.1. Relative motion between the base and the walls was achieved by moving the z-stage of the machine with the walls fixed. For each layer, the cross section of the part was defined by patterning the doped powder with the dosing mechanism. After the doped powder was dispensed, the remaining region within the layer was filled with



virgin powder, and the powder bed was lowered by one layer thickness. The top surface of the chamber walls aligned with the platform of the stand so that virgin powder could be spread to the remaining regions. The prototype machine required the virgin powder to be spread manually, although automatic powder spreading could be incorporated into future versions.

After depositing all layers, the filled chamber containing the doped powder bed needed to be removed from the machine and placed in the RF applicator. A system incorporating multiple interlocking parts was designed to detach the filled chamber from the machine. Figure 5.5 shows the four-step procedure for removing the powder bed. The base was connected to the piston rod through an adapter that locked into a keyway cut into the bottom of the base. In the first step, the base was attached to the piston rod and moved down as the powder layers were deposited. Once the build process was completed, the adapter was rotated to align with the keyway and removed as shown in the second and third steps. Without a rigid attachment to the machine, the filled chamber could be removed and placed between the RF electrodes.

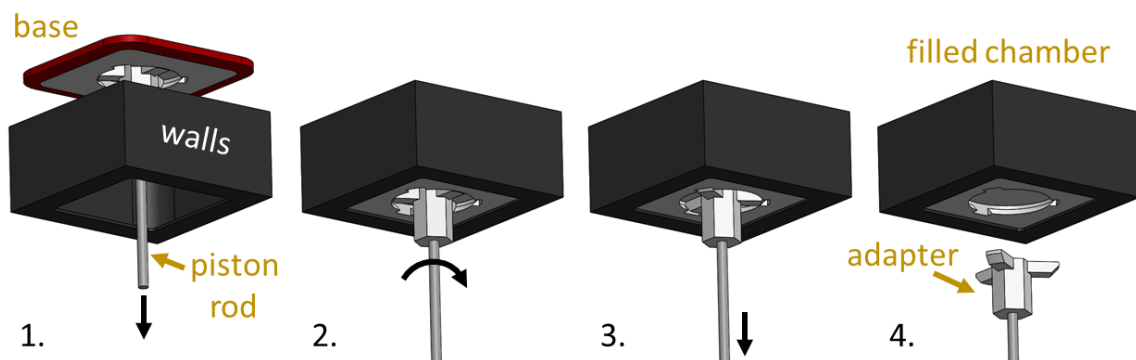


**Figure 5.5** Steps detailing the separation of the powder bed from the patterning machine to enable heating in the RF generator

It was important for the powder piston to seal properly with the walls of the build chamber to prevent the powder bed from leaking, so a rubber gasket was placed around the perimeter. To create the complex keyway geometry in the base and to ensure the chamber

would not interfere with the RF radiation, the base and walls were additively manufactured in PLA plastic. The build chamber contained no metallic components and could be placed directly between the electrodes in the RF generator to heat the entire powder bed after building.

The dimensions of the build chamber were 62.4x62.4x30 mm, but the maximum part thickness was slightly reduced because a thin layer of virgin powder was spread over the base before depositing the doped powder. The thin nylon layer provided thermal insulation to the bottom of the powder bed and prevented the doped region from fusing to the base. In this way, the build chamber could be reused in subsequent experiments. The chamber dimensions limited the size of the parts that could be fabricated, but the modular design of the machine facilitated alternate chamber geometries. The build chamber could be replaced by fabricating the base and walls in the desired geometry and creating a wooden platform with a cutout in the shape of the chamber cross section.

### ***5.2.3 Process Planning***

The motion of the stepper motors in the powder deposition machine was controlled by sending customized g-code commands to the machine. G-code (also called RS-274) is a programming language that is widely used in numerical control applications such as CNC machining and additive manufacturing [125]. In addition to controlling machine parameters such as advancing the stepper motors and homing the axes, g-code commands moved the nozzle to specific x and y locations, raised and lowered the piston, and coordinated the rotation of the dosing wheel.

Before generating the process planning steps, the layer thickness and the spacing between individual powder deposits were determined. The doped powder formed small mounds below the nozzle as it was dispensed by the dosing mechanism. Depicted in Figure 5.6, the peaks of the mounds protruded above the layer line but were leveled off when the

virgin powder was added and the layer was spread. After spreading, each of the powder deposits occupied a volume defined by the spacing between them and the layer thickness known as a voxel. Ideally, the volume of the voxel would match the volume of the cavities in the dosing wheel which was  $3.55 \text{ mm}^3$ . In practice, however, the voxel volume needed to be larger than the cavity volume to account for deposition inconsistencies and to ensure the doped powder did not extend above the layer surface after spreading. If the spacing or layer thickness were too small, a surplus of doped powder would develop at the surface and interfere with subsequent layers. Through empirical testing, it was determined that an x/y spacing of 1.81 mm and layer thickness of 2 mm gave the best results, corresponding to a voxel volume of  $6.55 \text{ mm}^3$ . The dimensions of the voxel were important because they determined the minimum achievable resolution of the process in the three build axes.

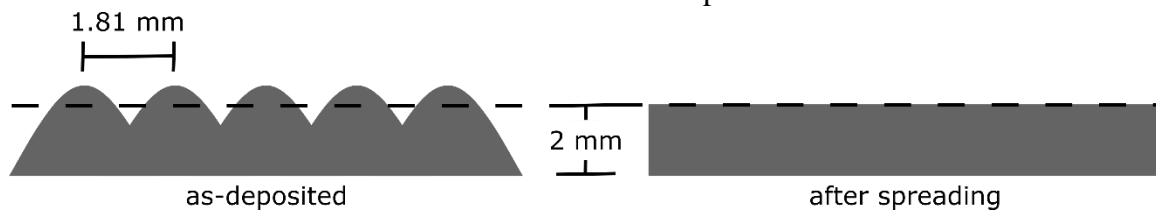


**Figure 5.6** Side view representation of doped layer before (left) and after (right) spreading. Each mound of doped powder was deposited at spacing of 1.82 mm in the x and y directions, and the layer thickness was 2 mm

After determining the spacing of the powder deposits and the layer thickness, the process planning steps were created. The part geometry was divided into layers, and the cross section was further subdivided into an array of points that were spaced according to the x/y resolution. The coordinates were processed in Matlab and converted into the appropriate g-code commands. The resulting g-code file contained all necessary instructions for defining the geometry, and only the process of spreading the powder required manual intervention. During tests of the powder deposition mechanism, it was discovered that the path of the nozzle as it traversed the array of points influenced the

geometric definition, particularly at the edges of the part. The most consistent results were achieved when the part was doped from the interior outward in a spiral pattern. Figure 5.7 shows the deposition points and nozzle paths for the square, triangular, and ring geometries along with the patterned results. Slight inconsistencies in the volume of powder deposited by the dosing mechanism were responsible for the observed deviations at the edges, but the overall coverage of the doped powder across the layer surface demonstrated the effectiveness of the selective doping and process planning strategies.

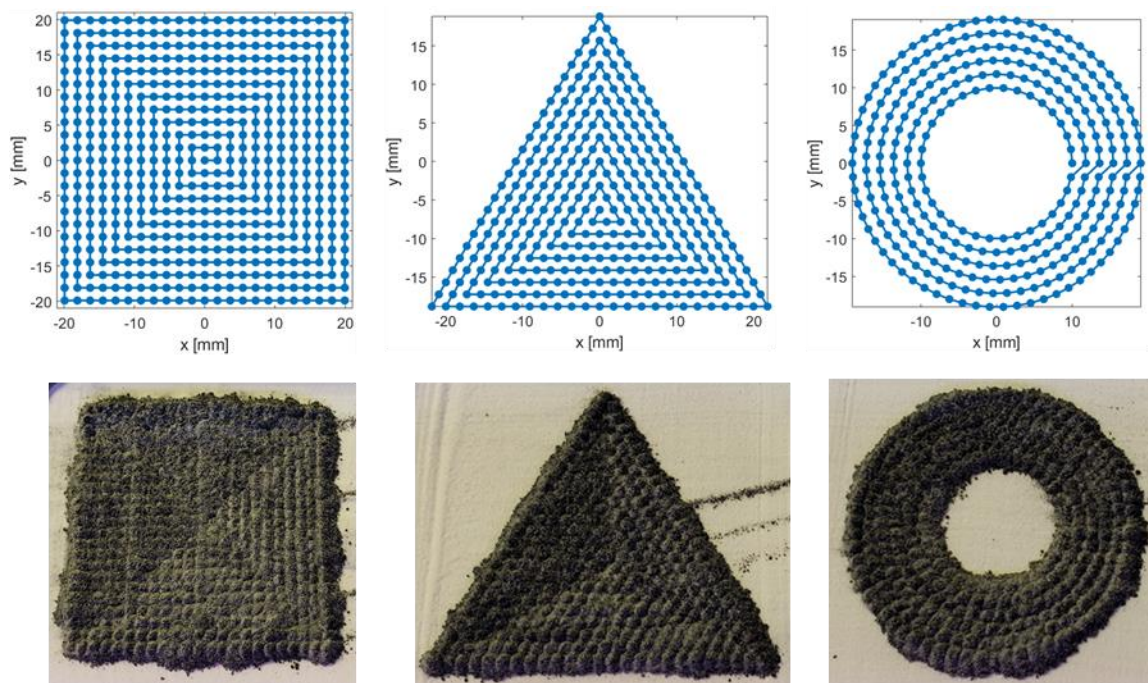


**Figure 5.7** Deposition points and paths (top) compared with patterned powder (bottom) for square, triangular, and ring geometries

The process planning procedure enabled the selective doping of arbitrary geometries provided they could be discretized into Cartesian points. After the files were prepared in Matlab, a laptop computer provided an interface with the prototype machine. An open-source software called ReplicatorG was used to interpret the g-code files and execute commands on the machine over a USB connection. The process planning steps in this implementation were capable only of creating uniformly doped geometries.

Modifications to the g-code file generation procedure to enable functional grading of the powder bed are presented in the next section.

#### ***5.2.4 Functional Grading with Powder Deposition Machine***

Functional grading of the powder bed in the deposition system was achieved by filling the powder hopper with mixtures of different graphite and nylon concentrations. The dopant concentrations were chosen based on the results of the computational design strategy that tuned the electrical conductivity throughout the part volume. The powder deposition system could not continuously vary the dopant and required discrete graphite concentrations. Four distinct levels of doping were considered for the functional grading experiments. The computational models were queried at each point that powder would be deposited in the samples, and one of four possible powder compositions was chosen based on the value of the tuned conductivity.

To enable functional grading of the dopant in the powder deposition machine, custom process planning instructions were written to generate the g-code that controlled the motion of the stepper motors. The functionally graded conductivities were separated into four groups corresponding to the four different powder mixtures used to define the doped geometry. The four powder mixtures contained 23%, 26%, 28%, and 35% graphite by weight, respectively. The part was divided into layers, and each point within the layer was assigned a value of 1 to 4 to represent the powder mixture to be deposited there. Figure 5.8 shows the functionally graded layer files for the bottom and top layers for a square prism, where the colors correspond to the powder mixtures of increasing graphite content.

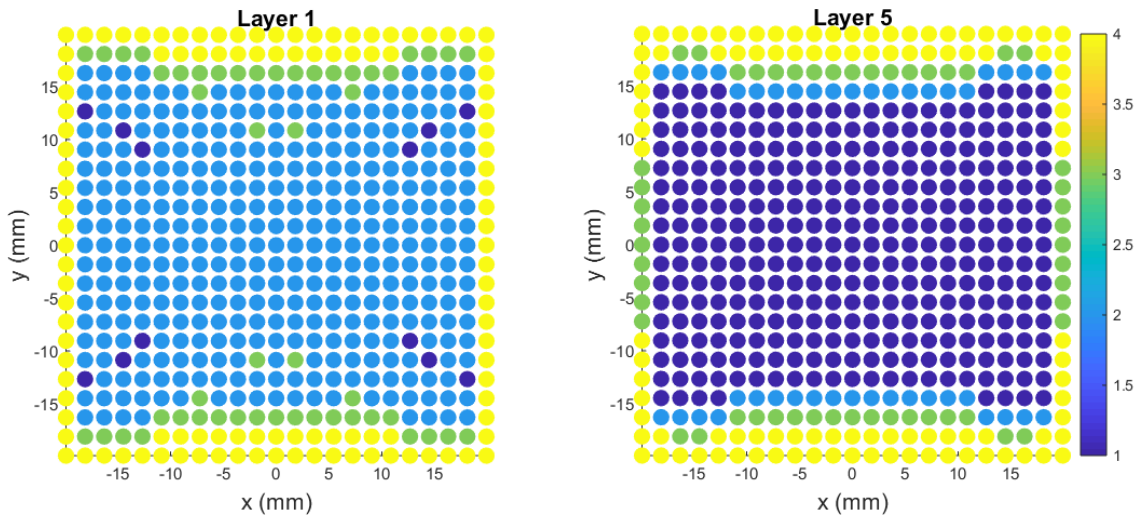


**Figure 5.8** Functionally graded layer files for a square prism for the bottom (left) and top (right) layers. The colors in the image represent the powder mixture to be deposited in the  $(x,y)$  location, and the graphite content increases with increasing powder designation.

The layer files were converted to g-code instructions that featured pauses within each layer to change the powder composition in the hopper. After depositing dopant in each of the locations specified by the layer file for a given concentration, the nozzle moved above the overflow tray so the powder mixture could be changed. The previous mixture was removed by vacuuming the remaining powder from the hopper and dosing wheel. The hopper was then filled with the next powder mixture, and the dosing wheel rotated one revolution to prime the system before deposition. As with powder spreading, the process of changing the powder compositions was performed manually but could be automated in future iterations of the machine.

### 5.2.5 Powder Deposition Limitations

The powder deposition system was a useful prototyping tool capable of selectively patterning dry nylon/graphite powders with the ability to discretely functionally grade the mixtures throughout the part geometry. However, there were several limitations in the system that would need to be addressed in future iterations of the machine design. The spatial resolution of the patterned dopant was considerably lower than other additive

manufacturing processes. Selective laser sintering has an in-plane resolution and layer thickness of 0.5 mm and 0.1 mm, respectively, compared with the 1.81 mm in-plane resolution and 2 mm layer thickness of the powder deposition machine [126]. Further, the observed inconsistencies in the deposition volume had a negative effect on the edge definition and could be improved by using alternate methods to produce the components in the powder dosing mechanism. The machine also required manual intervention at regular intervals to spread the powder and change compositions, which could be automated in future versions. Concerning functional grading of the powder bed, the greatest limitation of the prototype system was that it supported only discrete concentrations of pre-mixed graphite/nylon powders. Future systems could incorporate a mixing stage above the nozzle to allow continuous grading of the dopant. Despite its limitations, the powder deposition machine was an improvement over using forms to pattern the doped powders. The next section introduces an alternate method in which an inkjet print head supplies the dopant to the powder bed.

### **5.3 INKJET SYSTEM FOR PATTERNING DOPANT**

#### **5.3.1 *System Design***

Instead of depositing dry powder mixtures to define the doped geometry, an alternate method would be to deliver the dopant to the nylon powder bed using an inkjet print head and electrically conductive ink. The system would resemble a typical binder jetting machine, but the binder would be replaced with an ink mixture that contains conductive particles. Collaborators at the University of Nottingham developed a laboratory-scale inkjet system with custom-formulated conductive inks to use in the RFAM process. The system featured a 38x38x40 mm build chamber with a 16 nozzle piezoelectric print cartridge. The resolution in the x/y plane was restricted by the spacing between the nozzles which was 25  $\mu\text{m}$ , and a layer thickness of 262  $\mu\text{m}$  was used for the tests. In

piezoelectric print heads, ink is guided through a small channel, and a pulse of electricity is applied to a piezoelectric transducer located inside the nozzle. The electric current causes the transducer to deform a diaphragm and eject small volumes of ink through the nozzle [127].

To create the electrically conductive inks, carbon nanoparticles were added to a solvent mixture. The three primary factors that govern the jetability of a particle-based ink are the viscosity, surface tension, and propensity to clog the nozzle from particulate buildup [128]. The challenge in developing a custom ink formulation for RFAM was determining the maximum carbon nanoparticle loading that could be achieved before the onset of clogging in the nozzles. Rheology measurements and test prints were conducted at the University of Nottingham to evaluate the performance of the inks. An ink composition of 7.9% carbon nanoparticles, 87.4% dimethylformamide (DMF), and 4.7% polyvinylpyrrolidone (PVP) by weight was found to maximize the carbon loading while maintaining suitable jetting characteristics. The custom ink was used to print small geometries into a nylon powder bed, and RF heating experiments conducted on the samples are discussed in the next chapter.

The laboratory-scale printing equipment was useful for conducting initial RF heating tests on the particulate inks but was not capable of producing large parts. To scale up the process, further testing was required using the University of Nottingham's commercial binder jetting machine manufactured by Integrity. The build chamber in the Integrity machine measured 100x175x40 mm, and the layer thicknesses could be set in increments of 10  $\mu\text{m}$ . The machine used SG1024/MA print heads with 1024 nozzles arranged in 4 rows to achieve 600 DPI printing. In addition to the larger build volume over the laboratory-scale machine, the print heads in the Integrity system spanned the width of the powder bed and could print an entire layer in a single pass. Both Nottingham inkjet



systems were capable of high-resolution dopant patterning compared with the powder delivery machine, but further testing was required to evaluate the RF heating effectiveness of the ink-doped mixtures.

### 5.2.2 Build Chamber Design

The build chamber used in the powder deposition machine was matched to the desired electrode spacing during RF heating and required a new chamber to be constructed for each electrode configuration. A similar chamber design could be implemented in the inkjet patterning method, but the added machine functionality in the inkjet system offers alternate solutions for containing the doped powder bed. The Integrity machine at the University of Nottingham is equipped with dual print head capability such that two different ink mixtures can be printed simultaneously. The electrically conductive ink composes the first mixture, but a binder could be used in the second print head. As the powder layers are spread, the first print head defines the dopant geometry while the second print head creates the chamber geometry by binding the nylon around the part. The binder only defines the walls of the chamber and does not interact with the dopant. Upon completion, the powder bed contains a doped region surrounded by a binder-infused nylon box as shown in Figure 5.9.

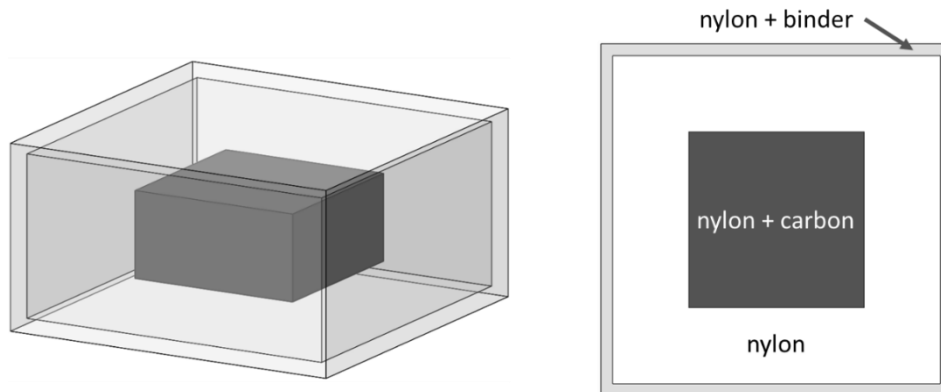


**Figure 5.9** Proposed build chamber design for the inkjet system where the chamber is divided into three regions containing nylon and carbon dopant, loose nylon powder, and nylon mixed with a binder to form the walls.

The filled chamber can be removed from the larger inkjet system powder bed and placed in the RF applicator for heating. Building the chamber geometry simultaneously with the part geometry eliminates the need to create a new build chamber for each electrode configuration as was the case in the powder deposition machine. It also enables printing different chamber dimensions without modifying the overall architecture of the inkjet system between builds.

### **5.3.3 Functional Grading**

Two methods are proposed to incorporate functional grading capability into the inkjet patterning system. In the first method, the concentration of dopant could be varied by performing multiple passes of the print head over the powder bed such that the number of droplets deposited to each pixel in the x/y plane are varied. For example, if eight ink droplets are required in one location and five in another, the print head would pass over the powder bed eight times before advancing to the next layer. An ink droplet would be placed in the first location during each of the eight passes, while the second location would receive an ink droplet for only five passes. A similar solution to achieve the same desired effect would be to slow the motion of the print head to jet multiple droplets in a given location before advancing. In either case, the dopant concentration could be functionally graded at the same resolution as the inkjet print head, which is determined by nozzle spacing.

Another method would be adjusting the resolution of the printed pattern to achieve different levels of grading. Instead of varying the dopant concentration at each pixel across the powder bed, the dopant could be graded in clusters of pixels. Within a pixel cluster, different dopant levels could be achieved by selectively turning certain pixels “on” or “off” based on the desired concentration. In this method, a 4x4 grid of pixels would have 17 possible states that could be graded by printing different patterns within the grid. Figure 5.10 shows an example of possible patterns for different levels in the 4x4 pixel cluster, but

intermediate levels could also be achieved. The disadvantage of using this method to adjust the dopant concentration is the reduction in resolution associated with considering pixel clusters. The in-plane resolution for a nozzle with 25  $\mu\text{m}$  spacing would be reduced to 100  $\mu\text{m}$  if a 4x4 pixel grid is used.

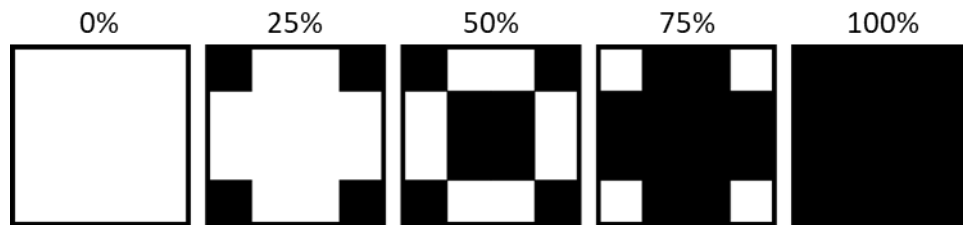


*Figure 5.10 Possible patterns for doping a 4x4 grid of pixels to different concentrations*

The inkjet dopant delivery system offers promising advantages over the powder deposition machine. Inkjet printing is a well-established technology capable of patterning ink droplets at high resolutions and accuracy. In the radio frequency additive manufacturing process, inkjet printing could enable high speed dopant delivery in addition to functional grading throughout the powder bed.

#### **5.4 CLOSURE**

In this chapter, two methods for patterning the dopant in a radio frequency additive manufacturing process were presented. In the first method, pre-mixed graphite and nylon blends were distributed to the powder bed using a dosing mechanism to deposit discrete volumes of doped powder at specified coordinates. A prototype system was developed to enable the powder deposition and featured a removable build chamber that could be transferred to the RF heating apparatus. Functional grading of the dry powders was achieved by modifying the process planning software to incorporate pauses during printing to change the powder composition based on input from the computational models. The second system used an inkjet print head to supply dopant to the powder bed in the form of an electrically conductive nanoparticle ink. Collaborators at the University of Nottingham

developed the ink formulations and experimental system for testing the RF heating characteristics of the ink-doped powder beds. Two strategies for functionally grading the dopant in the powder bed were also proposed for the inkjet system. The focus of this chapter was to introduce potential approaches for patterning the dopant in an RFAM system and highlight the design features of a prototype machine. The next chapter explores the capabilities of the powder delivery system and presents initial results on the effectiveness of functionally grading the powder bed.

## **Chapter 6: RFAM Capabilities and Design Guidance**

Previous chapters established the need for functionally grading the dopant in the RFAM process and proposed two methods for patterning the dopant to allow spatial variation. In this chapter, the effects of functional grading and two-stage RF heating are explored using the powder deposition machine described in the previous chapter. Initial RF heating experiments are conducted to test the feasibility of an inkjet dopant delivery system developed in collaboration with the University of Nottingham. The chapter concludes by offering design guidance for the RFAM process by identifying parts and features that are well-suited for RFAM as well as design choices that should be avoided.

### **6.1 RF HEATING EXPERIMENTS AND GEOMETRIC IMPROVEMENT**

#### ***6.1.1 RF-Sintered Parts and Functional Grading Experiments***

The powder deposition machine was used to validate the functional grading efforts described in Chapter 4. The experiments were carried out for three geometries: a 4x4x1 cm square prism, an equilateral triangular prism with a side length of 4 cm and thickness of 1 cm, and a thin ring with an outer diameter of 4 cm, inner diameter of 2 cm, and thickness of 1 cm. Geometries with functionally graded doping were created by dividing the tuned electrical conductivities into four categories and selectively doping the powder bed according to the model results. Geometries with a uniform doping were printed along with the functionally graded parts to evaluate the effectiveness of the tuning process on improving the sintered geometry.

The fused geometries for uniform and functionally graded dopant concentrations are shown in Figure 6.1 for the square prism, triangular prism, and thin ring along with the RF exposure times used in the experiments. The functionally graded parts were exposed for longer durations because the tuning process necessarily reduced the total graphite content within the doped region.

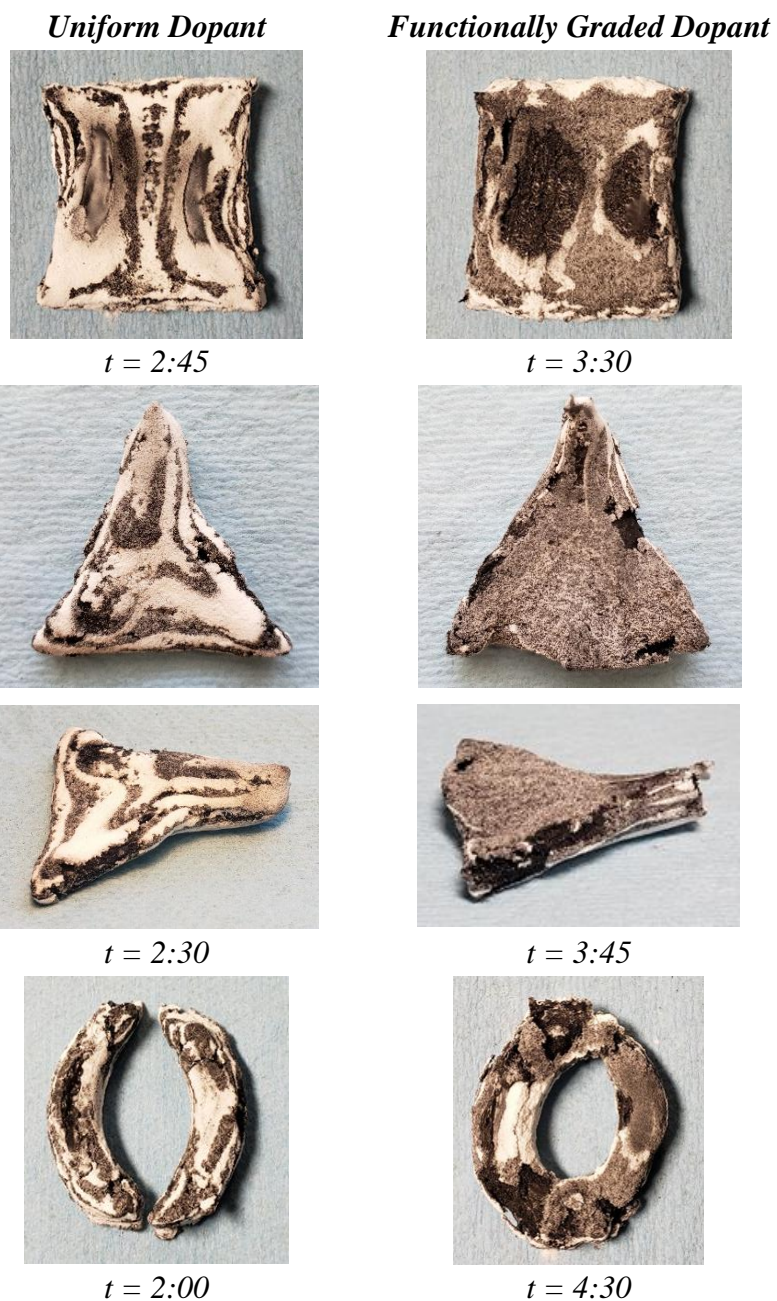


**Figure 6.1** Comparison between uniformly doped samples and functionally graded samples with corresponding RF exposure times in minutes

The effects of functional grading were subtle, but were most evident in the reduction in curvature on the top and bottom faces of the fused parts. The most significant improvement in the geometry between the uniform and functionally graded dopant was seen in the thin ring. Before grading the dopant, the ring formed two separate fused masses.

After functionally grading the dopant, however, greater fusion was achieved to consolidate the part into a single unit. The surface temperature profiles also indicated improvements in the functionally graded parts. Figure 6.2 shows the surface temperatures for the uniform and functionally graded square prism. Local hot regions predominantly along the sides of the uniformly doped part were less pronounced, and the temperatures were more uniform when the dopant was functionally graded. Despite the demonstrated improvements, the functional grading experiments were limited in the sense that only four dopant concentrations were used. The effects of functional grading could be amplified through continuous tuning of the powder bed. Although the differences between the tuned and uniformly doped parts were minor, the results served to validate the functional grading process as a means to improve the geometry of the sintered parts.

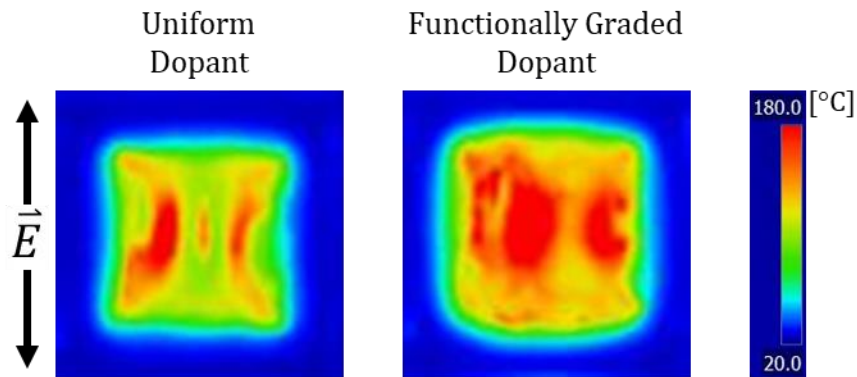


**Figure 6.2** Surface temperature for square prism captured at the end of the heating stage for a uniform dopant distribution (left) and functionally graded dopant (right)

The powder deposition machine was then used to test whether rotating the powder bed during the RF exposure could improve the part geometry without functionally grading the dopant. It was not feasible to continuously rotate the powder bed in the existing RF heating system, but the square build chamber could be rotated 90 degrees to apply the electric field in two orthogonal directions during heating. The build chamber was placed between the electrodes in one configuration, heated for a period of time, rotated 90 degrees,

and heated again in the new configuration. To test the effectiveness of the two-stage heating process, two geometries were selected. The first was the thin ring used in the functional grading experiments, and the second was a longhorn head. The thin ring was selected because the single-stage heating experiments revealed significant temperature rise along the sides of the ring with little heating in the top and bottom. By rotating the powder bed in a two-stage process, the heat could be distributed more evenly throughout the ring. The longhorn head was chosen due to the added geometric complexity and comparatively large aspect ratio.

The thin ring was heated for one minute in each electrode orientation. The fused geometry removed from the powder bed is shown in Figure 6.3. Compared to the single-stage heating and functionally graded results in Figure 6.1, the fused part produced after the two-stage heating process was the closest match to the intended geometry.



*Top/Bottom:  $t = 1:00$*

*Left/Right:  $t = 1:00$*

**Figure 6.3** *Fused ring geometry after two-stage heating where the powder bed was heated for one minute in each electrode configuration. Top/Bottom and Left/Right refer to the position of the electrodes with respect to the image.*

To demonstrate the effect of using multiple electrode configurations to heat the longhorn head geometry, the sample was first heated in each orientation separately. Figure 6.4 shows the fused mass removed from the powder bed after each of the experiments. In the first test, the electrodes were positioned on the left and right with respect to the image. In this configuration, the electric field was aligned in the direction of the horns and



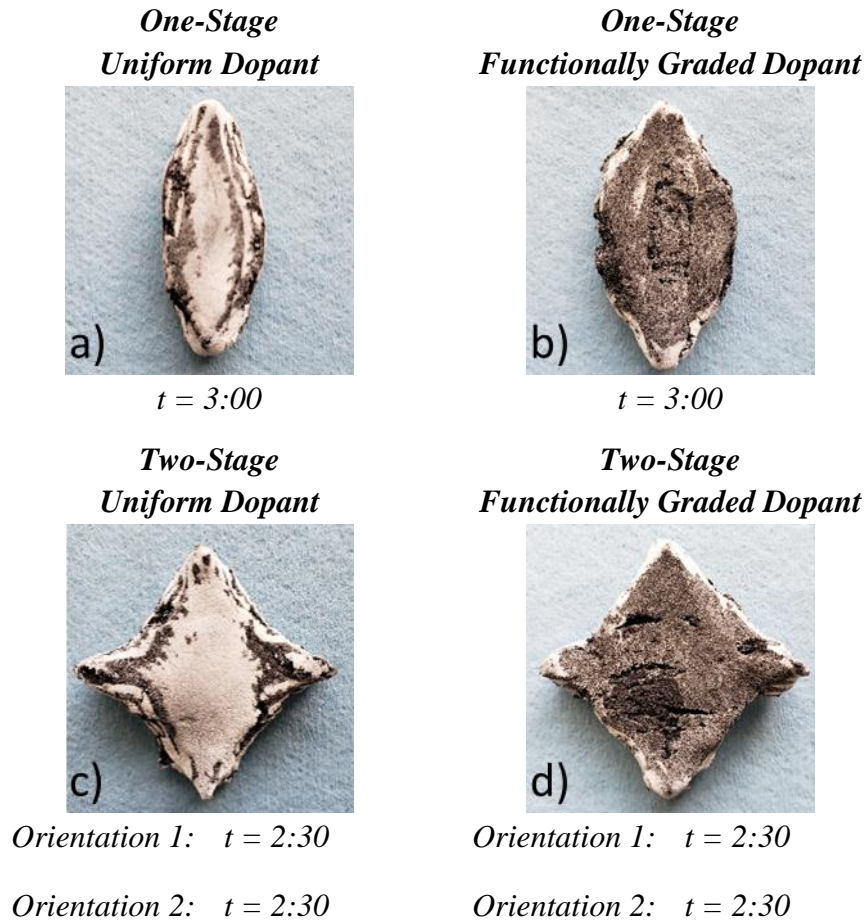
prevented heat generation within the head region. In the second experiment, the electrodes were placed on the top and bottom with respect to the image, and the heat was concentrated in the head region with little development in the horns. In the combined case, however, the longhorn head was first heated in the left/right configuration for 30 seconds and rotated to the top/bottom configuration for 2 minutes of RF exposure. After the two-stage process, the main features of the longhorn were present in the final fused part. Each of the three experiments produced parts that were similar to the COMSOL®-predicted geometries described in Chapter 4.



**Figure 6.4** Fused parts from uniform dopant concentration after heating in multiple electrode configurations with corresponding RF exposure times in minutes. Top/Bottom and Left/Right refer to the position of the electrodes with respect to the image.

The computational models suggested the heating uniformity and fused geometry could be improved further by combining the effects of functional grading with the two-stage heating process. To demonstrate the combined effect, a square diamond geometry was chosen where the corners of the diamond pointed towards the electrodes in both configurations. This geometry was a suitable candidate for showing the combined effect because the orientation of the corners relative to the electrodes provided adverse conditions for heating uniformity that could not be mitigated through functional grading or powder bed rotation alone. The models indicated a reduction in the uniformity index from 0.161 for a single electrode configuration and uniform dopant distribution to 0.074 when the effects of rotating the powder bed with a functionally graded dopant were considered. The

RF heating experiments for the diamond geometry followed the same procedure presented in Chapter 4 where the part was heated using a single electrode orientation with a uniform dopant distribution and functionally graded dopant. Then, the part was heated in a two-stage process in which the powder bed was rotated for the uniformly doped case and functionally graded case. The fused parts removed from the powder beds after the four experiments and the RF exposure times are shown in Figure 6.5. The COMSOL® models predicted an improvement in heating uniformity across each of the experiments which was confirmed by the relative geometry improvements in the fused parts. Matching the simulations, the experiments for the single-stage, uniform dopant produced the part with the greatest deviation in the intended geometry. Fusion was limited to the center section of the diamond with little heat generation in the sides. Even with functional grading, single-stage heating was unable to completely fuse the sides of the geometry. The results were improved when heating in two stages, but it was only by combining the effects of two-stage heating with functional grading that the sintered part most closely resembled the intended geometry.

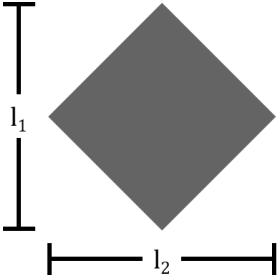


**Figure 6.5** Fused parts from square diamond geometry heated in four configurations with RF exposure times in minutes. a) Single electrode orientation with uniform dopant. b) Single electrode orientation with functionally graded dopant. c) Two electrode orientations with uniform dopant. d) Two electrode orientations with functionally graded dopant.

The experimental parts were also consistent with the COMSOL® predicted geometries presented in Chapter 4. The simulated geometries were compared with the RF-sintered parts by collecting measurements of the primary axes. The measurement results are provided in Table 6.1 where  $l_1$  and  $l_2$  correspond to the longitudinal and lateral dimensions of the diamond, respectively. From the measurements, the COMSOL® predicted geometries closely matched the fused parts with the exception of the longitudinal ( $l_1$ ) dimensions in the two-stage experiments where the fused geometry exceeded the simulation predictions. The discrepancy can be explained by the fact that the models only

represented the liquid phase volume at the end of the simulation, and regions that had transitioned from liquid back to solid due to cooling in the second heating stage were not displayed. Despite the discrepancies, the models still provided a reasonable estimation of the final part geometry, and the functional grading process was further validated by the experiments.

**Table 6.1** Measurement comparisons between geometry predictions in COMSOL® and experimentally-fused parts.

		COMSOL®	Experiment	
Single-Stage Uniform Dopant	l <sub>1</sub> [mm]	40.03	42.04	
	l <sub>2</sub> [mm]	15.84	16.86	
Single-Stage Functionally Graded Dopant	l <sub>1</sub> [mm]	41.04	41.40	
	l <sub>2</sub> [mm]	28.76	23.05	
Two-Stage Uniform Dopant	l <sub>1</sub> [mm]	23.73	40.18	
	l <sub>2</sub> [mm]	39.96	40.87	
Two-Stage Functionally Graded Dopant	l <sub>1</sub> [mm]	31.39	40.63	
	l <sub>2</sub> [mm]	39.17	42.09	

Applying the RF energy in a two-stage mechanism reduced the functional grading requirements. This can be seen by aggregating the functionally graded conductivity values across the part domains in the one- and two-stage simulations and displaying the results as histograms. The functionally graded conductivities for the two heating strategies are shown in Figure 6.6. In both cases, a majority of the points were tuned to the maximum conductivity level (0.0425 S/m) corresponding to the regions with low temperature rise where the heuristic tuning procedure attempted to increase the temperature by raising the conductivity. However, the histogram of the two-stage graded conductivities shows fewer points at the maximum value and a greater spread among the lower levels. The difference between the histograms suggests the two-stage tuning process provided a more even distribution of graded conductivity values than the single stage results. Therefore, it was

demonstrated that the functional grading effort can be reduced and the part geometry improved by combining a two-stage heating process with functional grading of the dopant.

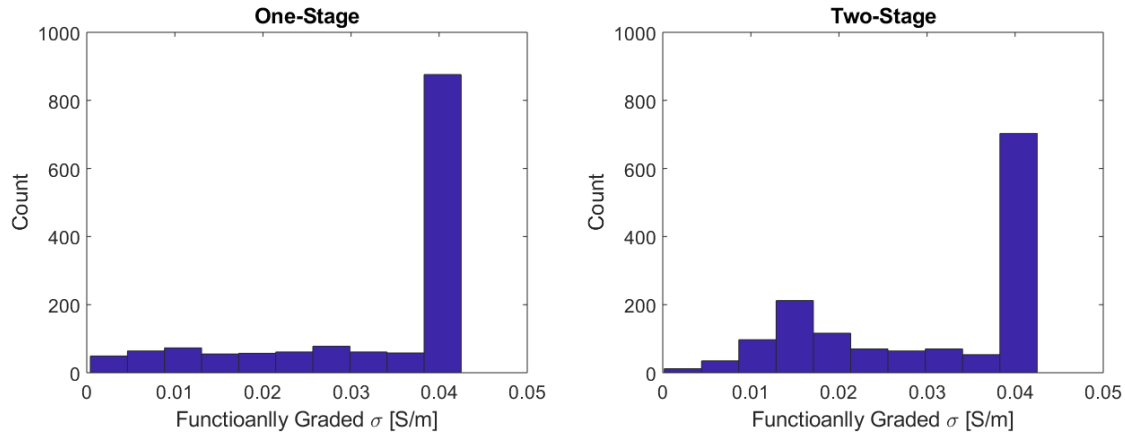


**Figure 6.6** Histograms comparing the aggregated, functionally graded conductivity values across the part domains for the one-stage (left) and two-stage (right) heating strategies

In each of the preceding tests, the powder deposition machine was used to print prismatic geometries to validate the computational models and demonstrate the effectiveness of implementing a two-stage heating process. However, the system was not limited to simple structures and was capable of patterning the dopant into fully three dimensional shapes. To demonstrate the capabilities of the machine, a lattice-like geometry consisting of two thin rings connected by vertical struts was patterned in the powder bed. The doped geometry as it was positioned in the powder bed is shown in Figure 6.7.

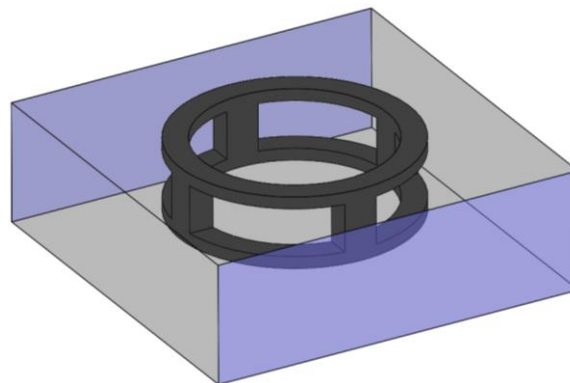


**Figure 6.7** Three dimensional strut geometry as positioned in the powder bed with the electrodes marked in purple.

Using a mixture containing 35% graphite by weight, the geometry of the ring lattice structure was patterned with the powder deposition machine. In the previous thin ring experiments, the best results were obtained by heating the powder bed in two stages without functional grading. For this reason, the two-stage method was chosen to heat the ring lattice. Figure 6.8 shows two examples of parts created from the heating experiments on the three dimensional geometry. In the first sample, the upper annulus did not fully form, but there were clearly defined spaces between the struts. Both rings were completely formed in the second sample, but there was significant oversintering in the virgin powder between the struts. The two parts were created under nominally identical processing conditions, but variations in the amount of dopant deposited and errors induced from manually spreading the powder layers revealed the limitations of the existing system. The inconsistencies in the results could be improved through greater process control in the dopant patterning system, however, the experiments demonstrated the ability to create three dimensional parts using the RFAM process.



*Orientation 1: 2:00*  
*Orientation 2: 1:30*



*Orientation 1: 2:00*  
*Orientation 2: 1:15*

**Figure 6.8** Fused part removed from powder bed after two-stage heating of the thin ring lattice structure.

### **6.1.2 RF Experiments on Inkjet-Printed Samples**

As described in Chapter 5, the resolution of the RFAM process could be improved by patterning the dopant using an inkjet printing system and carbon nanoparticle ink. The RF heating characteristics of the inkjet-printed parts were expected to differ from the dry powders because the dopant was suspended in a solvent, and the particle size was

considerably smaller than the graphite powders used in the previous experiments. To establish the feasibility of an inkjet dopant patterning system for RFAM, heating experiments were conducted on inkjet-printed samples.

Collaborators at the University of Nottingham aided in the printing of carbon-doped nylon samples that were shipped to the University of Texas for testing in the RF chamber. The initial experiments consisted of testing 20x20x3 mm square samples. The samples were created using a custom ink formulation developed at the University of Nottingham and printed on a laboratory-scale inkjet printer. The samples were printed with varying ink volumes and had an estimated carbon loading between 5% and 25% by weight.

The RF heating effectiveness was evaluated by measuring the surface temperature of the samples with a FLIR infrared camera as they were tested in the experimental RF chamber at the University of Texas. The RF experiments measured the total temperature rise on the visible top surface of samples with varying dopant concentrations. The dopant concentration was adjusted by printing different numbers of ink droplets at each pixel in the part. The carbon concentration within the part was estimated from the volume fraction of carbon in the ink mixture, the volume of ink deposited at each pixel, and the droplet spacing.

The temperature rise as a function of carbon content after 10 minutes of RF exposure is shown in Figure 6.9. Although there was significant variation in the measurements, the data could be separated into three regions. The first region showed almost no heating for concentrations below 10% carbon by weight followed by a period of rapid increase in temperature rise. In the second region, the temperature rise reached a maximum value at approximately 20% carbon by weight before beginning to decline. Lastly, the third region exhibited a steep drop-off in temperature rise as the dopant concentration increased beyond 20%. The heating curves from the ink-printed samples

followed a similar trend as the dry graphite/nylon powder mixtures, but at lower dopant concentrations. The smaller particle diameter of the carbon nanoparticles in the ink compared with the micron-sized graphite powders lowered the percolation threshold in the nylon composites. The results of the heating experiments can be used to map the electrical conductivity values in the computational models to the required carbon concentration and printing parameters.

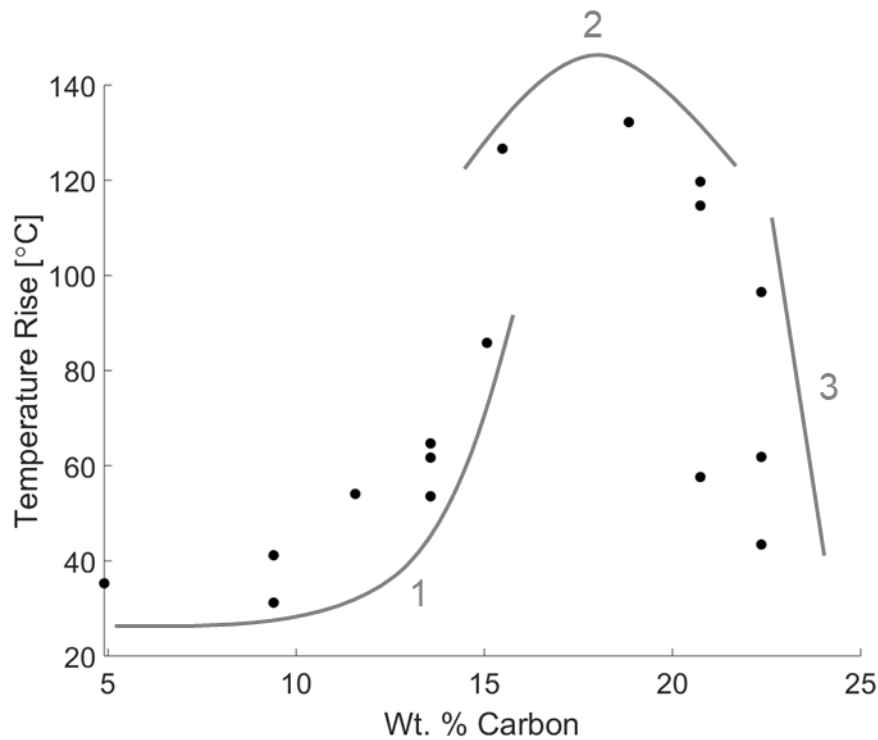


*Figure 6.9* Temperature rise as a function of carbon content for inkjet-printed samples after 10 minutes of RF exposure

Powder fusion was also demonstrated using the laboratory-scale inkjet system by printing a 20x20x10 mm sample with a carbon concentration of 17% by weight. The sample was heated for 10 minutes in the RF generator. After cooling, a fused mass was removed from the sample. The fused part, shown in Figure 6.10, measured 16x12x4 mm and represented a significant milestone in the development of the new additive manufacturing process as the first RF-assisted, volumetric, inkjet-printed part.



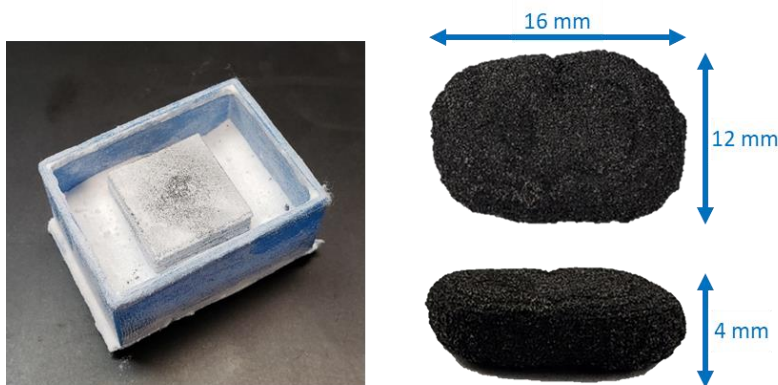


**Figure 6.10** Fused part from laboratory-scale inkjet printer, showing the printed part (left) and fused part after RF exposure (right). The printed dimensions of the part were 20x20x10 mm, and the final dimensions were 16x12x4 mm.

The laboratory-scale printing equipment was not capable of producing large parts. To scale up the process, further testing was required using the University of Nottingham's commercial binder jetting machine manufactured by Integrity. Limitations on the commercial machine meant printing the custom ink with high carbon loading was not possible due to particle agglomeration and nozzle clogging concerns. Commercial carbon inks were purchased through Nazdar with the product name "3D Black Fluid." The composition of the solvent and concentration of carbon within the ink were unknown, requiring the heating effectiveness experiments to be replicated with the commercial ink. To test the heating effectiveness of the commercial ink, mixtures of ink and nylon 12 were prepared and heated in the RF chamber.

The experiments consisted of mixing the ink into virgin nylon 12 powder in concentrations varying between 6% and 50% ink by weight. The mixtures were placed in a powder bed and exposed to RF radiation. Surprisingly, none of the mixtures produced a noticeable temperature rise during the experiments. Even testing the ink alone did not show any heat generation from the RF radiation. The ink was then added to a mixture of graphite and nylon powder containing 30% graphite by weight. RF heating experiments on the dry powder mixture showed significant heating and fusion, but the temperature rise was

reduced when the carbon ink was added. It was clear from the heating experiments that one of the materials used in the solvent was acting as an inhibitor to the sintering process either through physical separation of the particles or by reducing the electron motion in the mixtures. The heating experiments were then repeated after drying the nylon/ink mixtures overnight in an oven set to 140°C in an attempt to evaporate some of the solvent. The average surface temperature of the dried samples after 10 minutes of RF exposure is shown in Figure 6.11. The mixture containing 40% ink by weight produced the greatest temperature rise followed by a sharp decline. For concentrations above 50%, the mixtures did not produce any measurable rise in surface temperature. It is unclear whether the reduction in heating at higher concentrations was caused by the same factors as in the dry graphite powder mixtures or from residual solvent that had not fully evaporated during the drying process.

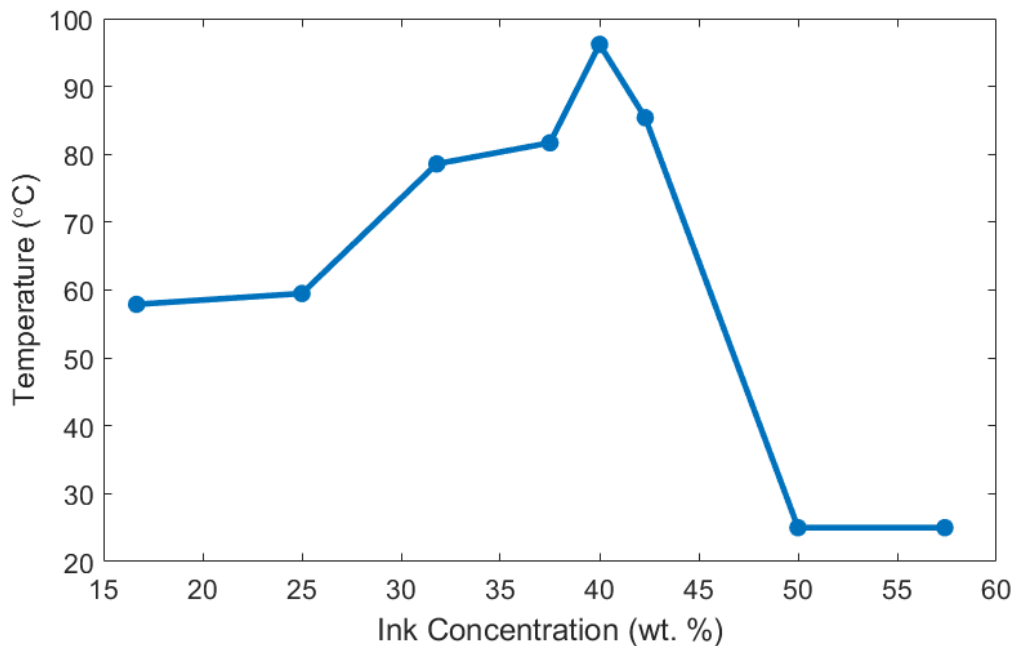


**Figure 6.11** Temperature rise as a function of ink concentration after drying in a 140°C oven overnight

The ink experiments showed that it was possible to heat mixtures containing the commercial ink and nylon powder, but the solvent needed to be evaporated for heating to occur. In the case of the commercial inkjet system, an infrared heat lamp can be used on each powder layer to remove the solvent before depositing the following layer. Further testing is required to develop an inkjet-based radio frequency additive manufacturing machine, but the initial results demonstrated the feasibility of heating and fusion with such a system.

## **6.2 DESIGN CONSIDERATIONS FOR RFAM**

Several factors should be considered when designing parts for the RFAM process. Part quality can be affected by attributes of the RF generator and applicator as well as the functional grading scheme. The powder deposition machine was used to show how different geometries have different RF heating characteristics. Although the geometric effects were mitigated through functional grading and rotating the powder bed, part design played a critical role in the resolution of the RFAM parts. The focus of this section is to offer design guidance for RFAM by considering the effect of various process parameters on part quality and providing an overview of features that are well-suited to the process as well as features that should be avoided. Table 6.2 provides a summary of the guidelines with images depicting unfavorable and favorable design choices. The guidelines are intended to improve the likelihood of success when creating RFAM parts.

### ***6.2.1 Effect of Process Parameters on Heating Uniformity***

The process parameters used in RFAM can affect the quality of the sintered parts. Functional grading has been shown to be a necessary component in creating complex geometries, and so this section investigates the effect of three different process parameters on the heating uniformity of functionally graded powders. The three parameters are the number of discrete gradations, the spacing of the electrodes, and the electrode voltage.

COMSOL® was used to determine the impact of each factor on the uniformity index, and the heating simulations were conducted for a 4x4x1 cm square prism.

### 6.2.1.1 Number of Dopant Gradations

The powder deposition machine used to create the functionally graded parts required the powders to be pre-mixed into distinct graphite concentrations. In applying the heuristic tuning method to functionally grade the powder bed, the electrical conductivity was continuously adjusted. The continuous results were then separated into a pre-determined number of levels corresponding to the pre-mixed powder concentrations. The effect of varying the number of dopant concentrations on the heating uniformity was investigated using the COMSOL® models. Figure 6.12 shows the tuned electrical conductivity divided into 1, 2, 4, 8, and 16 levels as well as the continuously tuned case.

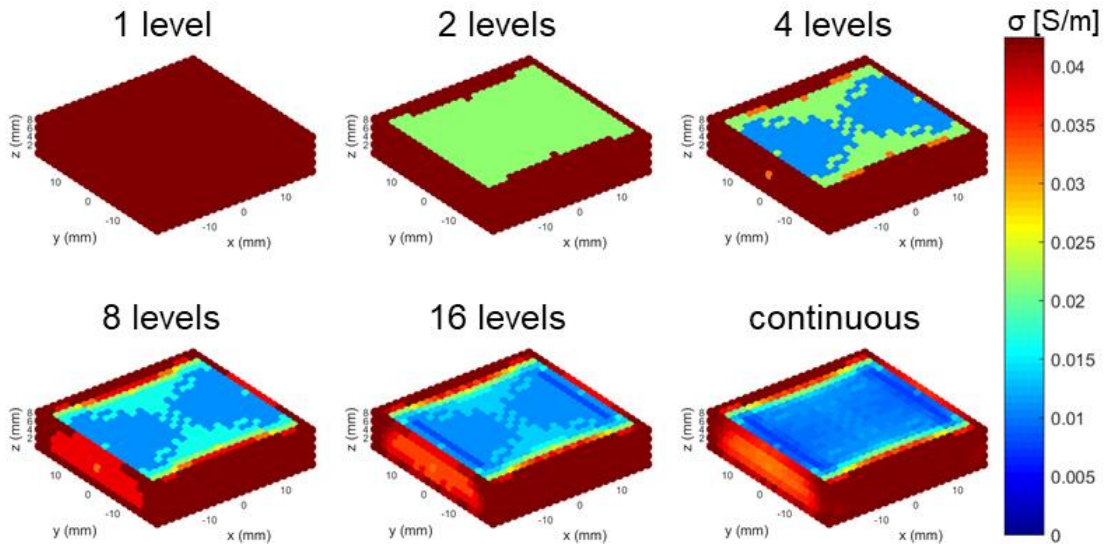


*Figure 6.12 Tuned electrical conductivity divided into 1, 2, 4, 8, and 16 levels as well as the continuously tuned conductivity for the 4x4x1 cm square prism*

The electrical conductivity of the doped region was defined in the COMSOL® models according to the different levels, and the uniformity index was evaluated after 120 seconds of simulated RF exposure with a prescribed electrode voltage of  $\pm 1,200 V_{\text{rms}}$  corresponding to an electric field strength of 385 V/cm. The uniformity index as a function

of the number of dopant levels is given in Figure 6.13. The simulation results showed little change in the heating uniformity between one and two dopant levels followed by steady improvements in the heating uniformity as the number of levels was increased. The uniformity index was reduced from 0.14 in the uniform case to 0.08 when the conductivity was divided into 16 levels. The uniformity index could be decreased further to 0.07 by continuously tuning the powder bed.

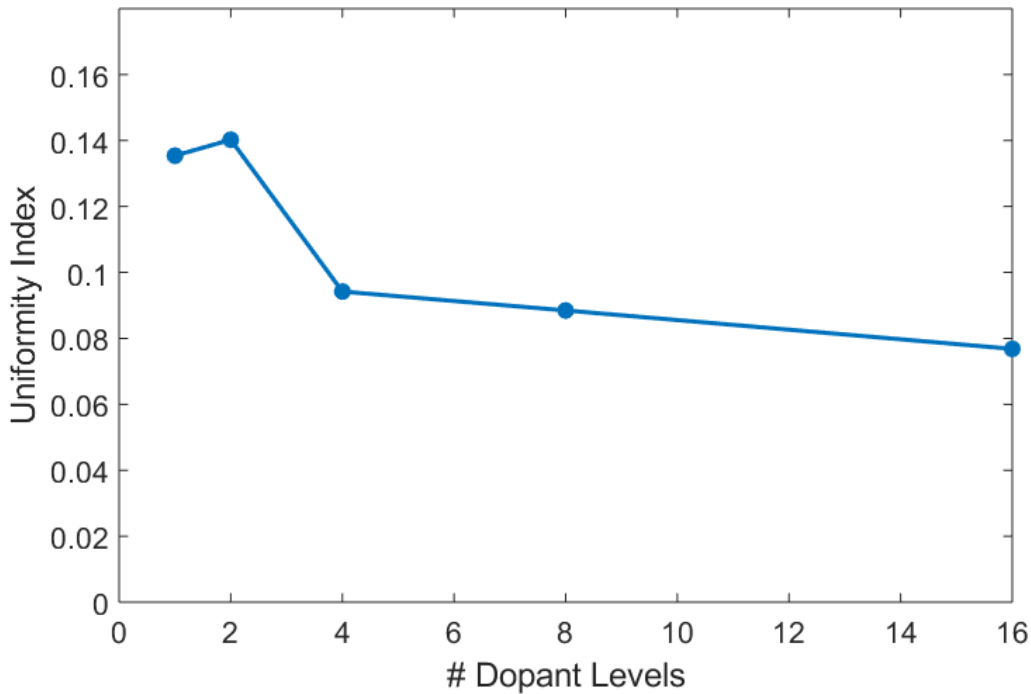


*Figure 6.13* Uniformity index as a function of the number of dopant levels used to functionally grade the powder bed.

Figure 6.13 shows the largest improvement in uniformity index between two and four levels followed by a gradual reduction as the number of levels increases. Therefore, the decision to use four levels of dopant in the RF heating experiments to functionally grade the powder bed was sufficient in demonstrating the potential improvements from grading. In the current system for patterning the dopant, greater effort is required to functionally grade the powder bed into more levels because the process is manual. Automatic powder

changing or mixing the dopant at the nozzle to enable continuous grading could improve the part quality in future machine iterations.

The heating uniformity improvements as a function of dopant gradation can also be seen in the temperature distributions in Figure 6.14. As the number of dopant levels increases, the temperature profiles at the center cross section of the prism become more uniform.

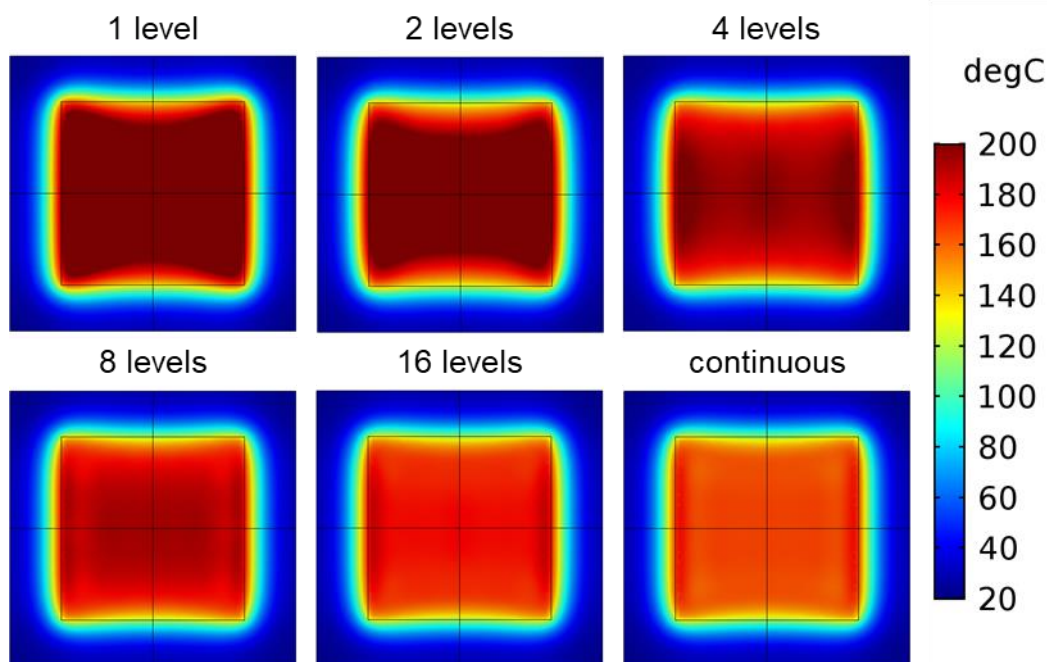


*Figure 6.14 Simulated temperature distributions in COMSOL®, taken 5 mm from the top and bottom faces for each of the grading levels*

### 6.2.1.2 Electrode Spacing

The electric field strength directly impacts the power loss in RF heating applications and influences the effectiveness of the heuristic tuning method. The magnitude of the applied electric field is defined as the voltage difference across the electrodes divided by the spacing between them. Two approaches for changing the electric field strength were considered. The distance between the electrodes and the applied voltage were adjusted to measure the effect of electric field strength on heating uniformity.

In creating parts for RFAM, the electrode spacing is determined by the size of the powder bed. The COMSOL® models were used to investigate the effect of increasing the electrode spacing on the uniformity index in the functionally graded parts. The simulations were conducted for a 4x4x1 cm prism, and the functional grading was carried out according to the heuristic tuning procedure outlined in Chapter 4. The electrode spacing ( $d$ ) was defined as the distance between the edge of the part and the electrodes when the part was placed in the center of the applicator. The results are given in Figure 6.15, where increasing the electrode spacing was shown to cause an increase in the uniformity index. Therefore, better heating uniformity can be achieved by reducing the electrode spacing as much as possible because it produces a larger electric field strength for a given electrode voltage.

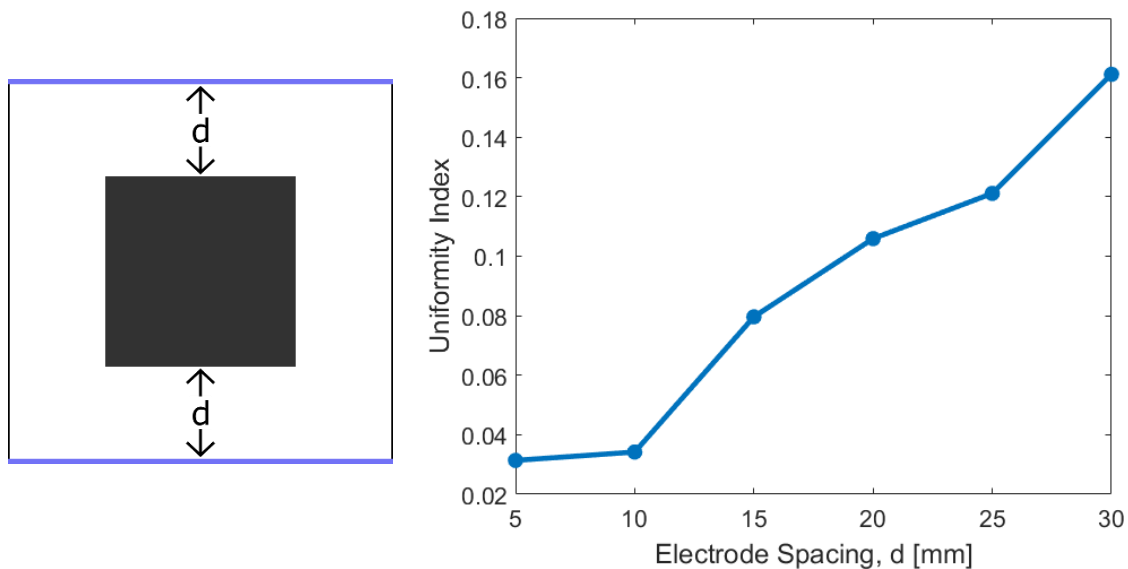


*Figure 6.15 Heating uniformity as a function of electrode spacing,  $d$ , defined as the distance between the edge of the part and the electrode*

### 6.2.1.3 Electrode Voltage

In addition to the electrode spacing, the electric field strength can be adjusted by changing the voltage supplied to the electrodes. The electrode voltage is limited by the power output of the RF generator, and increasing the maximum voltage may require

upgrading the system. To study the effect of electrode voltage on heating uniformity, simulations were conducted for a 4x4x1 cm prism. Similar to the electrode spacing simulations, the heuristic tuning procedure outlined in Chapter 4 was used to functionally grade the electrical conductivity. Shown in Figure 6.16, increasing the electrode voltage in the heating simulations greatly reduced the uniformity index value after applying the heuristic tuning process. The initial temperatures at higher voltages greatly exceeded the target temperature for tuning, and thus there appeared to be a slight increase in the uniformity index for electrode voltages above 2,000 V<sub>rms</sub> ( $E_{rms} = 641$  V/cm). The uniformity index could be lowered at the higher voltages by exposing the powder bed to RF radiation for a shorter duration, but a constant exposure time of 250 seconds was chosen for the comparisons. As the electrode voltage was increased, the applied electric field strength also increased. Similar to the electrode spacing tests, the increased electric field strength improved the effectiveness of the functional grading procedure. In the RF heating experiments, the electrode voltage varied between 1,000 V<sub>rms</sub> and 1,200 V<sub>rms</sub> when the 560 W generator was used to supply the voltage with estimated **E**-field strengths varying between 321 and 385 V/cm. The results suggest that larger RF heating systems would be capable of achieving better part accuracy than systems with a smaller power output.



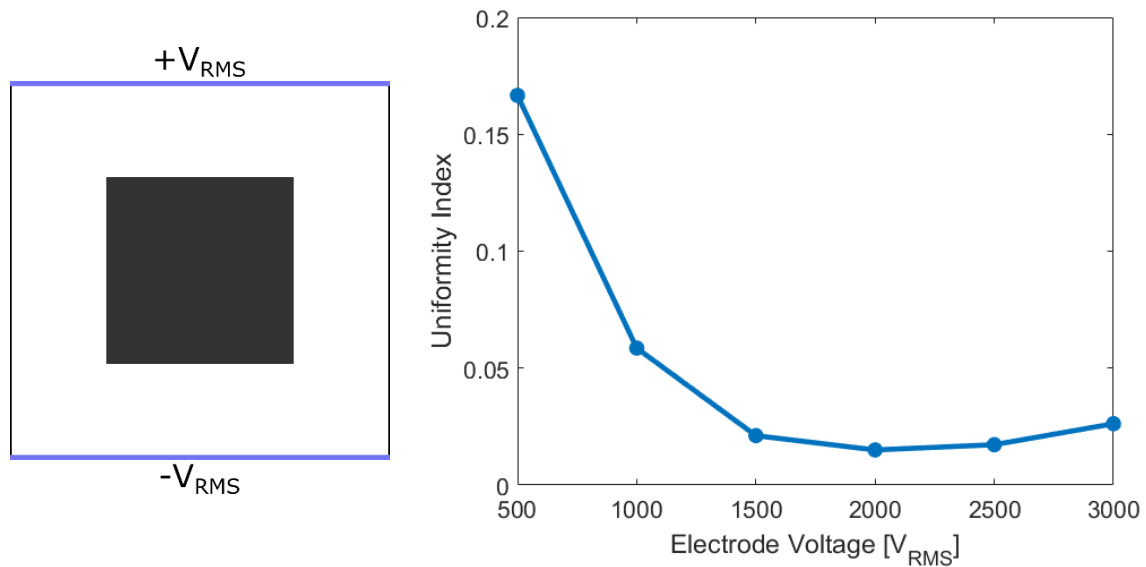


*Figure 6.16* Uniformity index as a function of electrode voltage

Either by reducing the electrode spacing or increasing the voltage, the strength of the applied electric field positively impacted the functionally graded heating uniformity. In RF heating applications, however, arcing can occur if the electric field becomes too large. When the electric field exceeds 10 kV/cm, the air inside the applicator can begin to ionize and break down resulting in unsafe processing conditions [31]. Therefore, it is important for designers to understand the tradeoff between increasing the electric field strength to achieve better geometric resolution and the possibility of arcing when determining the process parameters for RFAM parts. It should also be mentioned that the size of the part can affect the strength of the electric field. Using the spacing convention defined in Figure 6.15 and a constant electrode voltage, increasing the part dimensions causes a reduction in the electric field strength because the distance between the electrodes increases with the part size. Therefore, higher voltages are required to sustain the same electric field strengths in larger parts.

The number of gradations used in functionally grading the powder bed, the electrode spacing, and the applied electrode voltage were identified as process parameters

that can impact the heating uniformity in RFAM parts. Each of the parameters can be controlled to some extent and should be considered during the design stage for the best results. In general, the greatest RF heating uniformity is achieved by continuously grading the dopant, reducing the electrode spacing, and increasing the voltage. However, practical limitations on the electric field strength must also be considered to ensure the safe operation of an RFAM system.

### **6.2.2 RFAM Design Guidance**

The part geometry can significantly affect the resolution of features in the radio frequency additive manufacturing process. Although there is a complex relationship between the geometry and heating uniformity, several insights can be drawn from the RF sintering experiments. This section aims at identifying features that are well-suited for the RFAM process as well as features that should be avoided. Considering the RFAM capabilities and limitations during the part design stage can improve the chances of success and offer opportunities for future improvement of the process. The decision to use a uniform dopant concentration, functionally grade the dopant, rotate the powder bed, or combine functional grading with a rotating powder bed may change based on the geometry of the part. Features that are well-suited for each processing method can be identified from the simulation results and RF heating experiments. The guidelines are summarized in Table 6.2.

#### **6.2.2.1 Uniform Dopant Concentration**

The geometries that can be processed with a uniform dopant distribution and single electrode configuration are limited to those that are spherical or nearly spherical. The uniform electric field developed within spheres subjected to RF radiation causes heating within them to be uniform, but any deviation from a perfect sphere gives rise to geometrically-induced non-uniform heating. If the intended geometry is predominantly

spherical in shape, it may be possible to use a uniform dopant concentration to manufacture it with RFAM. The heating uniformity can be improved by rounding sharp corners as depicted in Figure 6.17 for a triangular prism with a side length of 40 mm. According to simulations conducted in COMSOL®, the uniformity index can be improved from 0.262 to 0.197 by applying a 5 mm radius to the corners of the triangular prism. While the use of fillets to round corners can improve the heating uniformity, the best results are achieved by functionally grading the powder bed. The simulations described in Chapter 4 suggest the uniformity index for the triangular prism can be reduced even further to 0.094 through functional grading.

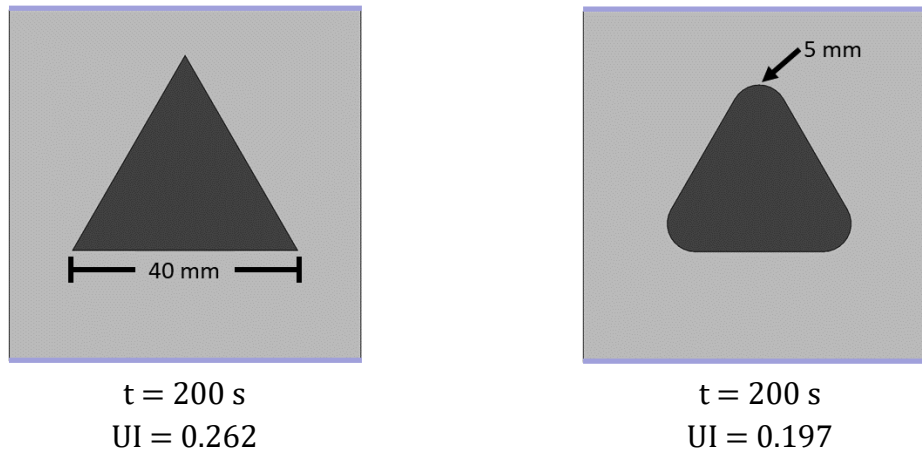


*Figure 6.17 Simulated geometry and uniformity index for triangle with filleted corners*

### 6.2.2.2 Functionally Graded Dopant

Functional grading of the powder bed is required when the part geometry differs substantially from spherical or includes flat faces and corners. Functional grading is most effective when the primary features are aligned with the applied electric field. In the case of the square diamond with a single electrode orientation, for example, fusion did not occur along the sides because the electric field was concentrated in the center of the part. Corners, faces, and edges cause field concentrations within the part, but functional grading of the powder bed can mitigate the effects and improve the resulting geometry.

### **6.2.2.3 Rotating Powder Bed**

Some geometries can be produced with a uniform dopant concentration by rotating the powder bed during heating. Parts that have multiple planes of symmetry such as cubes, cylinders, and rings are particularly suited for this method where functional grading of the powder bed is not required. While symmetric parts are good candidates for powder bed rotation, sharp corners aligned in the direction of the electric field can still cause adverse heating characteristics and should be avoided. Although the square diamond was symmetric about the two powder bed orientations, the corners caused field concentrations and non-uniform heating within the part resulting in unintended geometric anomalies. In the RF heating experiments, only two powder bed orientations were considered, but continuous rotation could expand the achievable geometries.

### **6.2.2.4 Functionally Graded Dopant with Rotating Powder Bed**

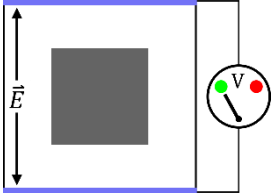
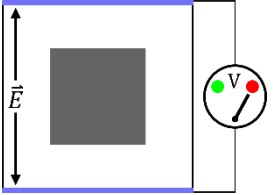
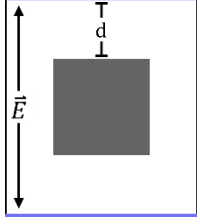
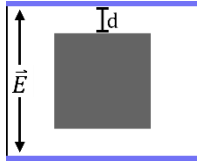
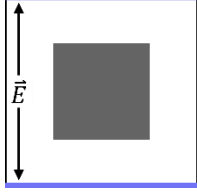
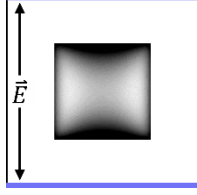
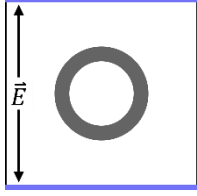
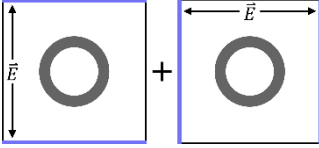
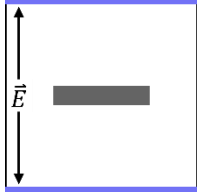
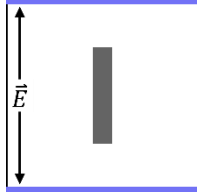
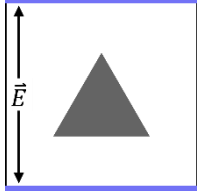
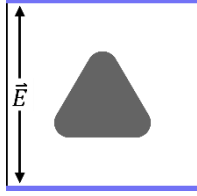
The RF heating experiments showed that the best geometric results can be obtained by combining the effects of functional grading with rotating the powder bed. If discrete powder bed orientations are used, parts with multiple planes of symmetry have the greatest likelihood of resolving successfully. However, functionally grading the powder bed can alleviate the electric field concentrations and enable fabrication of parts with flat faces and sharp corners. Continuous rotation of the powder bed could potentially offer additional geometric improvements, but simulating the rotating powder bed in the functional grading process would add computational expense.

### **6.2.2.5 Features to Avoid in RFAM**

Based on the results of the RF heating experiments, some features have been identified as unsuitable for the RFAM process in the current stage of development. Parts that have a combination of concave and convex features may have poor resolution after RF heating. This was shown in the longhorn head experiments where the main features were

resolved, but the region around the ears of the longhorn were missing entirely. The convex shape of the ears met the head in a sharp concave corner, and the region did not generate heat in either orientation in the RF experiments. Additional features that should be avoided are thin members that are not aligned with the electric field. In the ring lattice geometry, the thin struts connecting the two rings had much poorer resolution than the rest of the structure because the electric field was oriented perpendicular to the struts. For the best resolution, thin members should be aligned with the electric field. This could also be seen in the longhorn head experiments where fusion in the horns region was only possible when they were oriented in the same direction as the electric field. Among the part design considerations for RFAM, the orientation of features with respect to the electric field is perhaps the greatest predictor of part resolution. Designers creating parts for RFAM should therefore avoid orienting critical features perpendicular to the applied electric field.

Table 6.2 RFAM design guidelines with electrodes marked in purple.

Unfavorable	Favorable	Description
		<ul style="list-style-type: none"> <li>Heating can be improved by increasing the power supplied and thus the electrode voltage</li> <li><i>Note:</i> Large voltages can cause arcing, and caution should be exercised</li> </ul>
		<ul style="list-style-type: none"> <li>Reducing the electrode spacing, <math>d</math>, can improve heating by increasing the electric field strength</li> <li><i>Note:</i> Arcing can occur when the spacing too small, and caution should be exercised</li> </ul>
		<ul style="list-style-type: none"> <li>Non-spherical parts are subject to heating uniformity issues</li> <li>Consider functionally grading the dopant for parts with flat faces and sharp corners</li> </ul>
		<ul style="list-style-type: none"> <li>A single electrode orientation can lead to insufficient heating in certain regions</li> <li>Use multiple electrode orientations for parts that are symmetric about multiple axes</li> </ul>
		<ul style="list-style-type: none"> <li>Thin members oriented perpendicular to the electric field are less likely to resolve</li> <li>Thin members should be aligned parallel to the applied electric field</li> </ul>
		<ul style="list-style-type: none"> <li>Sharp corners can cause local temperature concentrations and should be avoided when possible</li> <li>Heating can be improved by adding fillets to corners</li> </ul>

### 6.3 CLOSURE

Using the powder deposition machine to pattern the dopant, the model results for functionally grading the powder bed were validated for several geometries. Functional grading was shown to improve the sintered geometry compared with a uniform dopant distribution, but the differences were subtle. The thin ring geometry demonstrated the clearest improvement by functional grading where the uniform dopant produced two separate parts that were joined into a single unit after functional grading. Rotating the powder bed was also shown to substantially improve the geometric resolution for the thin ring and longhorn head geometries. Combining the effects of functional grading with rotating the powder bed gave the best resolution for a diamond geometry and lessened the amount of grading that was required.

The results of the computational models and RF-sintering experiments were used to classify features that are well-suited for RFAM and inform design guidelines for the process. The effects of the functional grading scheme, electrode spacing, and electrode voltage influenced the heating uniformity in the simulations, and designers should therefore consider the process parameters when designing parts for RFAM. The part geometry also affected the heating uniformity, and various features were identified as suitable for each of the processing methods. In general, the orientation of features with respect to the applied electric field was the most important criterion for successful resolution. Future work in the development of radio frequency additive manufacturing will be focused on improving the resolution of the process by patterning the dopant with an inkjet printer. Successful initial results showed the feasibility of inkjet patterning, but continued effort is required to determine the effects of functional grading with the inkjet system.

## **Chapter 7: Conclusion**

The benefits of additive manufacturing are realized in the geometric complexity and design flexibility that can be achieved without requiring additional tooling. Polymer powder bed fusion processes offer additional utility by eliminating the need for support structures, but the layer-wise application of heat induces anisotropic mechanical properties and extends the production time for executing builds. The primary goal of this work is to introduce and develop a novel powder bed fusion method that achieves volumetric fusion of the polymer by means of RF radiation. The radio frequency additive manufacturing process is developed to improve the process speed and mechanical properties of polymer PBF by replacing the layer-wise heating strategies implemented in existing processes with a single stage, RF-assisted heating mechanism. This chapter describes the development of the RFAM process, summarizes the scientific contributions from this work, and explores avenues for future research.

### **7.1 SUMMARY OF WORK**

The work was motivated by explaining the fundamentals of RF heating and exploring its various applications throughout history. RF radiation was selected for this project because it has the advantage of large penetration depths and greater heating uniformity versus higher frequencies such as microwave and infrared. Historically, RF heating has been used in the medical industry for tissue heating as well as in the food industry for thawing, drying, and disinfecting. Previous research demonstrated that the electrical properties of insulating polymers can be enhanced through the addition of conductive dopants. RF heating was used to assist the curing of electrically conductive silicone composites, but volumetric fusion of a doped polymer using RF radiation as the sole energy source had not been demonstrated. Nylon 12 and graphite powders were



identified as two candidate materials for the polymer and dopant, respectively, for a volumetric radio frequency additive manufacturing process.

Next, electrical property measurements and RF heating experiments were conducted on mixtures of nylon 12 and graphite to assess the feasibility of RFAM. Using an impedance analyzer to measure the complex permittivity for various graphite concentrations, the primary loss mechanism was determined to be through electrical conduction as opposed to polarization. The effective conductivity of the mixtures increased with graphite content, and the percolation threshold of the mixtures was found to occur at graphite concentrations of approximately 30% by weight. The dielectric constant also exhibited an increasing trend with graphite content, and the tradeoff between charge storage and dissipation was observed as a peak in the loss tangent at 35% graphite by weight. RF heating experiments on the doped nylon mixtures followed a similar trend, such that maximum heating was observed in the mixture containing 32.5% graphite by weight. The experimental apparatus consisted of a parallel plate electrode applicator that contained the doped powder bed and an RF generator that supplied energy to the electrodes at a frequency of 27.12 MHz.

Upon determining the ideal graphite concentrations for RF heating, additional experiments were conducted to demonstrate fusion of the polymer using different geometries to define the doped portion of the powder bed. Thin forms with square, circular, and rectangular cross sections separated the doped powder from the surrounding virgin powder in the experiments. The powder beds were heated until the surface temperature exceeded the melting temperature of the nylon as measured by an infrared camera trained on the powder surface. The feasibility of RFAM was established by the fused parts that were removed from the powder beds after the experiments. However, non-uniform heating caused by the doped geometry was observed in the IR images and unintended curvature in

the fused parts. Mechanical property tests conducted on the RF-sintered samples showed a reduction in the tensile strength and ductility compared with laser sintered nylon 12. One possible source of the poorer mechanical properties could have been the formation of spherical voids within the parts due to gas desorption from the graphite particles during heating.

To mitigate the adverse geometric effects on heating uniformity, computational models were developed in COMSOL Multiphysics® to predict the temperature rise during the RF heating experiments. Incorporating the required thermal properties for phase change into the simulations enabled an approximate prediction of the final part geometry. Facilitated by the FEA models, two solutions were proposed to improve the heating uniformity. The first solution involved functionally grading the electrical conductivity throughout the powder bed to provide local tuning of the heating characteristics. The electrical conductivity was modified in an iterative scheme by applying a heuristic across the simulated domain according to the previously evaluated temperature. The heuristic raised the conductivity when the temperature was below a preselected target temperature, and lowered it when the temperature was above. The uniformity index provided a measure of evaluating the effectiveness of the heuristic tuning method by comparing the relative change with the un-tuned case. Functionally grading the electrical conductivity was shown to improve the uniformity index for several geometries, and the computational expense of the heuristic procedure was reduced compared with traditional optimization techniques. The second method for improving the heating uniformity involved a two-stage process in which the powder bed was rotated during heating so that the electric field was applied in two orientations. The simulations suggested an improvement in the uniformity index by rotating the powder bed without requiring the dopant to be functionally graded. However,

the best results were obtained by combining the effects of functional grading with multiple electrode orientations.

To validate the computational models, a method was needed for patterning the dopant and enabling spatial variation in dopant concentration. Two approaches for patterning the dopant were considered, and a prototype system was developed. The first method consisted of depositing pre-mixed formulations of nylon and graphite powders in distinct concentrations to a virgin powder bed. A prototype powder deposition device was designed and constructed by adapting a desktop filament extrusion machine. The doped powder was supplied by a dosing mechanism that traveled in the x and y axis of the build area. The powder was deposited to a chamber in a layer-wise fashion, and virgin powder was spread to the regions that did not receive dopant. The build chamber was designed to be removed from the machine easily and contained no RF-absorbing components apart from the patterned doped geometry. In this way, the chamber and powder bed could be placed in the RF applicator and heating could be isolated to the doped region alone. The second proposed method for patterning the dopant was to use an inkjet print head to deposit electrically conductive particles suspended in an ink solvent to a nylon powder bed. Collaborators at the University of Nottingham assisted by developing a laboratory-scale inkjet system and a custom ink formulation that contained carbon nanoparticles as the dopant. The custom system was used to establish the feasibility of an inkjet dopant patterning mechanism, and an alternate commercial inkjet machine was offered to scale the RFAM process and create larger parts.

The prototype powder deposition machine was used to pattern the dopant into several geometries, and RF heating experiments were conducted on the powder beds. Functional grading was achieved by depositing four different mixtures of varying graphite concentrations based on the results of the computational models. Tests were performed on

powder beds containing uniform dopant distributions, functionally graded dopant, powder bed rotation, and a combination of functional grading with powder bed rotation. The results suggested the geometry of the fused parts could be improved by implementing each of the techniques identified in the simulations. Experiments on the inkjet patterning system were conducted by heating small samples prepared with different printing parameters to vary the dopant concentration. The results demonstrated a similar trend to the dry powders, such that heating increased with increasing dopant concentration and reached a maximum before declining at higher dopant concentrations. Initial experiments on the commercial ink mixtures for use in the large-scale jetting system revealed the presence of a solvent that inhibited heat generation when subjected to RF radiation. The heating characteristics were improved by evaporating the solvent in an oven before applying the radiation, suggesting a commercial RFAM machine may require using IR lamps to evaporate the solvent at each layer.

After demonstrating the capabilities of the prototype system and conducting feasibility experiments on two inkjet solutions, design guidelines were created to explore the process parameters and features that must be considered when creating RFAM parts. It was shown that the heating uniformity could be improved through continuous grading of the dopant and by increasing the electric field strength. The orientation of the electric field was determined to have the greatest impact on the resolution of features. Designers should align thin members with the applied electric field and avoid sharp corners whenever possible. The initial insights from the guidelines highlight the capabilities and limitations of RFAM and motivate future development of the process.

## **7.2 CONTRIBUTIONS**

The primary contribution from this research is the development of a novel powder bed fusion process. Radio frequency additive manufacturing represents the first volumetric

AM method administered to thermoplastic polymers. Instead of applying heat on a layer-by-layer basis, it is possible as a result of this work to fuse the polymer in a single heating stage. Unlike existing PBF processes that require precise thermal conditions and a heated build chamber, a majority of the RFAM process can be conducted at room temperature because the energy is supplied during the final step. Polymer AM is often compared with injection molding in terms of production cost, speed, and mechanical properties. The single-stage part fusion in RFAM brings the field of additive manufacturing one step closer to reaching injection molding standards by removing the negative consequences of layer-wise heating.

The development of RFAM also enables several technological capabilities that were previously unavailable. Electrically conductive polymer composites have been studied extensively, but this work expands the concept to RF heating applications and provides a better understanding of the effect of dopant gradation on RF heating characteristics. The implications of this work extend beyond the scope of additive manufacturing as the results demonstrate the ability to achieve selective melting in conductive polymer composites by applying RF radiation.

Another contribution from this work is the computational design strategy used to functionally grade the dopant and achieve uniform part fusion. The heuristic tuning process to vary dopant concentration represents a new approach in improving RF heating uniformity. The ability to selectively deposit dopant in different concentrations within a powder bed enables local adjustment of the material's electrical properties, whereas most RF heating applications use materials with fixed properties. The heuristic tuning scheme facilitates manipulation of the electric field to alter the RF heating characteristics of the material. While this strategy is used to achieve uniform heating in RFAM, the same procedure could be applied to focus the electric field in certain regions of a part to generate

unique heating signatures. One potential application of this technique includes selectively heating joints in a structure where local softening of the polymer enables the geometry to be reconfigured.

RF sintering also impacts established design for additive manufacturing rules. Traditional paradigms focused on the avoidance of layer-wise heating effects are not valid for RFAM, and the guidelines for creating parts differ from other AM processes. The continued development of RFAM prompts further research into establishing new design guidelines for the process including metrology studies and mechanical property characterization efforts. Lastly, this work contributes to diversifying the broader field of engineering by promoting collaboration between different disciplines. Combining elements of electrical and mechanical engineering design principles in RFAM gives a new perspective on AM research and fosters interdisciplinary relationships for future process development. Volumetric fusion through RFAM provides a technological advancement towards the ongoing goal of using additive manufacturing to produce lightweight, functional parts for industrial use.

### **7.3 FUTURE WORK**

The avenues for future work in developing the RFAM process can be divided into three main categories. The first category consists of improvements that can be made to the existing process, and the second category involves expanding the capabilities of the process through continued experimentation with the inkjet dopant delivery system. Finally, the geometric resolution and mechanical properties of RFAM must be assessed through a metrology characterization effort.

Further modification of the current powder deposition prototype is required to refine the function of the machine and improve part resolution. As suggested by the computational models, continuous grading of the dopant yields the best results regarding

heating uniformity. The prototype machine requires the dopant to be graded in distinct concentrations of pre-mixed powder. However, the existing system could be adapted to enable continuous grading by dosing the nylon and graphite separately and mixing the two parts in the nozzle before they are deposited to the powder bed. In this way, the dopant concentration could be adjusted to any continuous level, and the effort required to change the powder compositions manually would be eliminated. Another opportunity to expand the capabilities of the process is by considering alternative materials for the electrically conductive dopant. In particular, carbon nanotubes have the potential to enhance the mechanical properties of the fused parts and lower the percolation threshold, thereby mitigating the adverse effects caused by the graphite powders and reducing the amount of dopant that is required.

Future work could also be focused on enhancing the computational models responsible for functionally grading the powder bed to achieve better part resolution. Although the computational expense is considerably smaller than gradient-based optimization, the heuristic tuning process requires each geometry to be simulated separately and repeatedly with different dopant distributions to generate the recommended functionally graded dopant distributions. There is an opportunity to implement a surrogate modelling approach in which the model can be trained on the dopant distributions for many different geometries to identify correlations between the tuned dopant distributions and heating uniformity. Dopant distributions for new geometries could be generated from the trained model at a reduced computational expense.

Future work aimed at upgrading the RF generator and applicator could provide additional benefits to the RFAM process. The RF generator used in the initial experiments is approximately 75 years old and requires manual adjustment of the output and tuning dials to provide coupling between the source and the load. Any changes in the electrical

properties of the powder bed during heating can shift the set point of the machine, requiring manual intervention and introducing inconsistencies between experiments. To achieve more reliable heating results, the RF generator should be replaced with a newer model that features a built-in matching circuit to ensure coupling between the source and load impedances is maintained throughout the duration of the experiment. The applicator could also be modified to achieve greater heating uniformity within the powder beds in RFAM. The simulations suggest rotating the powder bed during heating can yield superior results, but only two electrode configurations were considered due to experimental limitations. Incorporating a turntable into the applicator would enable continuous rotation of the powder bed throughout the experiment and potentially offer additional heating uniformity improvements. The challenge in adding a turntable is ensuring the electrical components do not interfere with the applied radiation. Therefore, all motors and wiring should be isolated from the applicator by placing them outside the Faraday cage and mechanically joining them to a turntable located beneath the electrodes. The accuracy of RFAM parts could be enhanced by incorporating these revisions to future iterations of the machine and applicator design.

Continued experimentation on the inkjet dopant delivery system is needed to broaden the capabilities of RFAM. The initial heating results from the inkjet-printed samples show significant scatter in the data. To facilitate functional grading, further testing is required to generate an accurate mapping between the printing parameters and effective electrical conductivity of the samples. The mapping can then be used to validate the computational models and functional grading simulations by performing similar experiments to those conducted using the powder deposition machine. Analogous experiments are also required for developing the commercial-scale inkjet system in addition to testing the IR lamp that evaporates the ink solvent at each layer. One of the



primary objectives of RFAM is to improve the process speed over other powder bed fusion methods, but the current prototypes are incapable of high throughput part production. In addition to increasing the attainable part volume over the existing systems, the commercial inkjet machine can be used as a testbed for targeting speed improvements. The development of an inkjet dopant delivery system is essential in creating high resolution RFAM parts at competitive build rates.

Lastly, a comprehensive metrology characterization of RFAM is essential to establishing its role within additive manufacturing. The geometric accuracy of RFAM can be quantified by building metrology test parts comprised of different feature types. Measurements of the features across many test part replicates can be used in statistical analyses to evaluate the accuracy of the process. The effects of part orientation and process parameters warrant continued investigation as the process is adapted and improved. The mechanical properties of RFAM parts should also be assessed using standard tension test specimens. Another primary objective of RFAM is to improve the anisotropic mechanical properties compared with layer-wise heating methods. To validate this claim, tensile specimens should be fabricated in different orientations within the powder bed to test the orientation dependence on the mechanical properties. The results of the metrology study and mechanical property assessment can be used to refine the existing design guidelines for RFAM.

#### **7.4 CLOSURE**

The radio frequency additive manufacturing process signifies a new paradigm in polymer powder bed fusion in which designers are no longer constrained by the challenges of layer-wise heating. The initial experiments offer promising insights into the feasibility of volumetric sintering and highlight the obstacles that must be overcome in the continued development of the process. The fused parts demonstrated by the prototype machine

showcase the capacity to create different geometries using the RFAM system while validating the various strategies aimed at improving part performance. Experimentation into the inkjet dopant patterning system motivates subsequent development of the process for enhanced build speed and resolution capabilities. RFAM enables additional research endeavors in the areas of computational design, manufacturing process development, and design for additive manufacturing. RFAM represents a small step towards the advancement of additive manufacturing as a viable production method, and the initial outcomes presented in this dissertation provide the groundwork for future growth.

## References

- [1] I. Gibson, D.W. Rosen, B. Stucker, *Additive Manufacturing Technologies: Rapid Prototyping to Direct Digital Manufacturing*, New York, NY: Springer, 2010.
- [2] R.G. Goodridge, C.J. Tuck, R.J.M. Hague, "Laser sintering of polyamides and other polymers," *Progress in Materials Science*, vol. 57, pp. 229-267, 2012.
- [3] J. Shen, J. Steinberger, J. Gopfert, R. Gerner, F. Daiber, K. Manetsberger, S. Ferstl, "Inhomogeneous shrinkage of polymer materials in selective laser sintering," in *Solid Freeform Fabrication Symposium*, Austin, TX, 200.
- [4] K. Manetsberger, J. Shen, J. Muellers, "Compensation of non-linear shrinkage of polymer materials in selective laser sintering," in *Solid Freeform Fabrication Symposium*, Austin, TX, 2001.
- [5] I. Gibson, D. Shi, "Material properties and fabrication parameters in selective laser sintering process," *Rapid Prototyping Journal*, vol. 3, no. 4, pp. 129-136, 1997.
- [6] P. Mercelis, J.P. Kruth, "Residual stresses in selective laser sintering and selective laser melting," *Rapid Prototyping Journal*, vol. 12, no. 5, pp. 254-265, 2006.
- [7] U. Ajoku, N. Saleh, N. Hopkinson, R. Hague, P. Erasenthiran, "Investigating mechanical anisotropy and end-of-vector effect in laser-sintered nylon parts," *Proceedings of the Institution of Mechanical Engineers*, vol. 220, no. 7, pp. 1077-1086, 2006.
- [8] W. Cooke, R.A. Tomlinson, R. Burguete, D. Johns, G. Vanard, "Anisotropy, homogeneity and ageing in an SLS polymer," *Rapid Prototyping Journal*, vol. 17, no. 4, pp. 269-279, 2011.
- [9] P.K. Jain, P.M. Pandey, P.V.M. Rao, "Effect of delay time on part strength in selective laser sintering," *International Journal of Advanced Manufacturing*, vol. 43, pp. 117-126, 2009.
- [10] T. Phillips, S. Fish, J. Beaman, "Development of an automated laser control system for improving temperature uniformity and controlling component strength in selective laser sintering," *Additive Manufacturing*, vol. 24, pp. 316-322, 2018.
- [11] D.T. Pham, X. Wang, "Prediction and reduction of build times for the selective laser sintering process," *Proceedings of the Institution of Mechanical Engineers*, vol. 214, no. 6, pp. 425-430, 2000.
- [12] M. Ruffo, C. Tuck, R. Hague, "Empirical laser sintering time estimator for Duraform PA," *International Journal of Production Research*, vol. 44, no. 23, pp. 5131-5146, 2006.
- [13] D.T. Pham, S.S. Dimov, "Characteristics and capabilities of RF systems," in *Rapid manufacturing : the technologies and applications of rapid prototyping and rapid tooling*, London, England, Springer, 2001, pp. 43-70.

- [14] H. Nouri, B. Khoshnevis, "Study on inhibition mechanism of polymer parts in selective inhibition sintering process," in *Solid Freeform Fabrication Symposium*, Austin, TX, 2015.
- [15] B. Asiabanpour, B. Khoshnevis, K. Palmer, "Advancements in the selective inhibition sintering process development," *Virtual and Physical Prototyping*, vol. 1, no. 1, pp. 43-52, 2006.
- [16] N. Hopkinson, P. Erasenthiran, "High speed sintering-early research into a new rapid manufacturing process," in *Solid Freeform Fabrication Symposium*, Austin, TX, 2004.
- [17] M. Shusteff, A.E.M Browar, B.E. Kelly, J. Henriksson, T.H. Weisgraber, R.M. Panas, N.X. Fang, C.M. Spadaccini, "One-step volumetric additive manufacturing of complex polymer structures," *Science Advances*, vol. 3, 2017.
- [18] B.E. Kelly, I. Bhattacharya, H. Heidari, M. Shusteff, C.M. Spadaccini, H.K. Taylor, "Volumetric additive manufacturing via tomographic reconstruction," *Science*, vol. 353, pp. 1075-1079, 2019.
- [19] I. Chodak, M. Omastova, J. Pionteck, "Relation between electrical and mechanical properties of conducting polymer composites," *Journal of Applied Polymer Science*, vol. 82, pp. 1903-1906, 2001.
- [20] W. Zhang, A.A. Dehghani-Sanij, R.S. Blackburn, "Carbon based conductive polymer composites," *Journal of Materials Science*, vol. 42, no. 3, pp. 3408-3418, 2007.
- [21] R. Uyar, F. Erdogdu, F. Sarghini, F. Marra, "Computer simulation of radio-frequency heating applied to block-shaped foods: Analysis on the role of geometric parameters," *Food and Bioproducts Processing*, vol. 98, pp. 310-319, 2016.
- [22] W. Hayt, *Engineering Electromagnetics*, McGraw-Hill Inc., 1989.
- [23] The Editors of Encyclopaedia Britannica, "Electromagnetic Spectrum," Encyclopaedia Britannica, 11 March 2019. [Online]. Available: <https://www.britannica.com/science/electromagnetic-spectrum>. [Accessed 13 April 2020].
- [24] S. Jiao, D. Luan, J. Tang, "Principles of Radio-Frequency and Microwave Heating," in *Radio-Frequency Heating in Food Processing: Principles and Applications*, Boca Raton, CRC Press, 2014, pp. 3-20.
- [25] M. Mehdizadeh, "Frequency allocations for industrial, scientific, and medical (ISM) applications," in *Microwave/RF Applicators and Probes: for Material Heating, Sensing, and Plasma Generation*, Waltham, William Andrew, 2015, pp. 369-370.
- [26] B. Vairamohan, I. Bran, G. Meric de Bellefon, "What's new in electrotechnologies for industrial process heating?," in *ACEEE Summer Study on Energy Efficiency in Industry*, Washington DC, 2011.

- [27] B.M. McKenna, J. Lyng, N. Brunton, N. Shirsat, "Advances in radio frequency and ohmic heating of meats," *Journal of Food Engineering*, vol. 77, pp. 215-229, 2006.
- [28] J. Sun, W. Wang, Q. Yue, "Review on microwave-matter interaction fundamentals and efficient microwave-associated heating strategies," *Materials*, vol. 9, pp. 231-256, 2016.
- [29] A.C. Metaxas, R.J. Meredith, *Industrial Microwave Heating*, Herts: Michael Faraday House, 1983.
- [30] S. Ryyanen, "The electromagnetic properties of food materials: a review of the basic principles," *Journal of Food Engineering*, vol. 26, pp. 409-429, 1995.
- [31] M. Mehdizadeh, "Electric field (capacitive) applicators/probes," in *Microwave/RF Applicators and Probes: for Material Heating, Sensing, and Plasma Generation*, Waltham, William Andrew, 2015, pp. 68-111.
- [32] H.A. Haus, J.R. Melcher, "Introduction to Electroquasistatics and Magnetoquasistatics," in *Electromagnetic Fields and Energy*, Englewood Cliffs, Prentice-Hall, 1989.
- [33] Z. Berk, "Heat and mass transfer, basic principles," in *Food Process Engineering and Technology*, Academic Press, 2018, pp. 79-126.
- [34] M. Mehdizadeh, "The impact of fields on materials at microwave and radio frequencies," in *Microwave/RF Applicators and Probes*, Waltham, William Andrew, 2015, pp. 1-33.
- [35] M. Mehdizadeh, "Fundamentals of field applicators and probes at radiofrequencies and microwave frequencies," in *Microwave/RF Applicators and Probes*, Waltham, William Andrew, 2015, pp. 34-67.
- [36] J. Hand, "Biophysics and Technology of Electromagnetic Hyperthermia," in *Methods of External Hyperthermic Heating*, Berlin, Springer-Verlag Berlin Heidelberg, 1990.
- [37] A. D'Arsonval, "Physiological action of currents of great frequency," in *Modern Medicine and Bacteriological Review, Volume 2*, Battle Creek, Modern Medicine Publishing Company, 1893, pp. 200-203.
- [38] J.L. O'Connor, D.A. Bloom, "William T. Bovie and electrosurgery," *Surgery*, vol. 119, no. 4, pp. 390-396, 1996.
- [39] R. Kovacs, "High Frequency Currents and Apparatus," in *Electrotherapy and Light Therapy*, Philadelphia, Lea & Febiger, 1945, pp. 187-204.
- [40] T. Watson, "Electrotherapy," in *Tidy's Physiotherapy*, Churchill Livingstone, 2013, pp. 417-455.
- [41] J. Osepchuk, "A history of microwave heating applications," *Transactions on microwave theory and techniques*, vol. 32, no. 9, pp. 1200-1224, 1984.

- [42] W.H. Cathcart, J.J. Parker, "Defrosting frozen foods by high-frequency heat," *Food Science*, vol. 11, no. 4, pp. 341-344, 1946.
- [43] J.C. Moyer, E. Stotz, "The blanching of vegetables by electronics," *Food Technology*, vol. 1, no. 2, pp. 252-257, 1947.
- [44] B.E. Proctor, S.A. Goldblith, "Radar energy for rapid food cooking and blanching, and its effect on vitamin content," *Food Technology*, vol. 2, no. 2, pp. 95-104, 1948.
- [45] Y. Jiao, J. Tang, Y. Wang, T.L. Koral, "Radio-frequency applications for food processing and safety," *The Annual Review of Food Science and Technology*, vol. 9, pp. 105-127, 2018.
- [46] J.C. Moyer, E. Stotz, "The electronic blanching of vegetables," *Science*, vol. 102, no. 2638, pp. 68-69, 1945.
- [47] W.H. Cathcart, J.J. Parker, H.G. Beattie, "The treatment of packaged bread with high frequency heat," *Food Technology*, vol. 1, no. 2, pp. 174-177, 1947.
- [48] S. Wang, G. Tiwari, S. Jiao, J.A. Johnson, J. Tang, "Developing postharvest disinfestation treatments for legumes using radio frequency energy," *Biosystems Engineering*, vol. 105, pp. 341-349, 2010.
- [49] S. Wang, M. Monzon, J.A. Johnson, E.J. Mitcham, J. Tang, "Industrial-scale radio frequency treatments for insect control in walnuts I: Heating uniformity and energy efficiency," *Postharvest Biology and Technology*, vol. 45, pp. 240-246, 2007.
- [50] S. Wang, J.N. Ikediala, J. Tang, J.D. Hansen, E. Mitcham, R. Mao, B. Swanson, "Radio frequency treatments to control codling moth in in-shell walnuts," *Postharvest Biology and Technology*, vol. 22, pp. 29-38, 2001.
- [51] B. Shrestha, O.-D. Baik, "Radio frequency selective heating of stored-grain insects at 27.12 MHz," *Biosystems Engineering*, vol. 114, pp. 195-204, 2013.
- [52] B. Shrestha, D. Yu, O.-D. Baik, "Elimination of *Cryptolestes Ferrungineus* S. in wheat by radio frequency dielectric heating at different moisture contents," *Progress in Electromagnetics Research*, vol. 139, pp. 517-538, 2013.
- [53] M.C. Lagunas-Solar, Z. Pan, N.X. Zeng, T.D. Truong, R. Khir, K.S.P. Amaratunga, "Application of radiofrequency power for non-chemical disinfestation of rough rice with full retention of quality attributes," *Applied Engineering in Agriculture*, vol. 23, no. 5, pp. 647-654, 2007.
- [54] S.-Y. Kim, H.-G. Sagong, S.H. Choi, S. Ryu, D.-H. Kang, "Radio-frequency heating to inactivate salmonella typhimurium and escherichia coli O157:H7 on black and red pepper spice," *International Journal of Food Microbiology*, vol. 153, pp. 171-175, 2012.
- [55] M. Gao, J. Tang, R. Villa-Rojas, Y. Wang, S. Wang, "Pasteurization process development for controlling Salmonella in in-shell almonds using radio frequency energy," *Journal of Food Engineering*, vol. 104, pp. 299-306, 2011.

- [56] H. Ramaswamy, J. Tang, "Microwave and radio frequency heating," *Food Science and Technology International*, vol. 14, no. 5, pp. 423-427, 2008.
- [57] T. Koral, "Radio frequency heating and post-baking," *Biscuit World*, vol. 7, no. 4, 2004.
- [58] Y. Wang, L. Zhang, J. Johnson, M. Gao, J. Tang, J.R. Powers, S. Wang, "Developing hot air-assisted radio frequency drying for in-shell macadamia nuts," *Food Bioprocess Technology*, vol. 7, pp. 278-288, 2014.
- [59] N.-H. Lee, C. Li, X.-F. Zhao, M.-J. Park, "Effect of pretreatment with high temperature and low humidity on drying time and prevention of checking during radio-frequency/vacuum drying of Japanese cedar pillar," *Journal of Wood Science*, vol. 56, pp. 19-24, 2010.
- [60] A. Altemimi, S.N. Aziz, A.R.S. Al-Hilphy, N. Lakhssassi, D.G. Watson, S.A. Ibrahim, "Critical review of radio-frequency (RF) heating applications in food processing," *Food Quality and Safety*, vol. 3, pp. 81-91, 2019.
- [61] S.L. Birla, S. Wang, J. Tang, "Computer simulation of radio frequency heating of model fruit immersed in water," *Journal of Food Engineering*, vol. 84, pp. 270-280, 2008.
- [62] S.R.S. Dev, S. Kannan, Y. Gariepy, G.S. Vijaya Raghavan, "Optimization of radio frequency heating of in-shell eggs through finite element modeling and experimental trials," *Progress In Electromagnetics Research B*, vol. 45, pp. 203-222, 2012.
- [63] B. Alfaifi, J. Tang, B. Rasco, S. Wang, S. Sablani, "Computer simulation analyses to improve radio frequency (RF) heating uniformity in dried fruits for insect control," *Innovative Food Science & Emerging Technologies*, vol. 37, no. A, pp. 125-137, 2016.
- [64] J.D. Hansen, S.R. Drake, M.A. Watkins, M.L. Heidt, P.A. Anderson, J. Tang, "Radio frequency pulse application for heating uniformity in postharvest codling moth (Lepidoptera: Tortricidae) control of fresh apples (*Malus Domestica* Borkh.)," *Journal of Food Quality*, vol. 29, pp. 492-504, 2006.
- [65] Y. Jiao, H. Shi, J. Tang, F. Li, S. Wang, "Improvement of radio frequency (RF) heating uniformity on low moisture foods with Polyetherimide (PEI) blocks," *Food Research International*, vol. 74, pp. 106-114, 2015.
- [66] X. Zhao, J. Zhao, J. Cao, X. Wang, M. Chen, Z. Dang, "Tuning the dielectric properties of polystyrene/poly(vinylidene fluoride) blends by selectively localizing carbon black nanoparticles," *Journal of Physical Chemistry*, vol. 117, pp. 2505-2515, 2013.
- [67] J.-C. Huang, "Carbon black filled conducting polymers and polymer blends," *Advances in Polymer Technology*, vol. 21, no. 4, pp. 299-313, 2002.

- [68] J. Amarasekera, "Conductive plastics for electrical and electronic applications," *Reinforced Plastics*, vol. 49, no. 8, pp. 38-41, 2005.
- [69] M. Stoppa, A. Chiolerio, "Wearable electronics and smart textiles: A critical review," *Sensors*, vol. 14, no. 7, pp. 11957-11992, 2014.
- [70] A.M. Grancaric, I. Jerkovic, V. Koncar, C. Cochrane, F.M. Kelly, D. Soulat, X. Legrand, "Conductive polymers for smart textile applications," *Journal of Industrial Textiles*, vol. 48, no. 3, pp. 612-642, 2017.
- [71] Y. Kim, B. Lee, S. Yang, I. Byun, I. Jeong, S.M. Cho, "Use of copper ink for fabricating conductive electrodes and RFID antenna tags by screen printing," *Current Applied Physics*, vol. 12, pp. 473-478, 2012.
- [72] R. Meredith, "Microwave energy for high speed, efficient vulcanization of extruded rubber," *Journal of Elastomers and Plastics*, vol. 8, pp. 191-209, 1976.
- [73] B. Krieger, "Microwave vulcanization: a lesson in business and technology," in *Materials Research Society Symposium Proceedings Vol. 347*, 1994.
- [74] C. Lee, "Microwave curing of silicone elastomers and foams for energy savings," *ACS Symposium Series*, vol. 107, pp. 45-50, 1979.
- [75] W. Zhang, R.S. Blackburn, A.A. Dehghani-Sanij, "Effect of carbon black concentration on electrical conductivity of epoxy resin-carbon black-silica nanocomposites," *Journal of Materials Science*, vol. 42, pp. 7861-7865, 2007.
- [76] D. Pantea, H. Darmstadt, S. Kaliaguine, C. Roy, "Electrical conductivity of conductive carbon blacks: influence of surface chemistry and topology," *Applied Surface Science*, vol. 217, pp. 181-193, 2003.
- [77] K. Miyasaka, K. Watanabe, E. Jojima, H. Aida, M. Sumita, K. Ishikawa, "Electrical conductivity of carbon-polymer composites as a function of carbon content," *Journal of Materials Science*, vol. 17, pp. 1610-1616, 1982.
- [78] H.-J. Choi, M.S. Kim, D. Ahn, S.Y. Yeo, S. Lee, "Electrical percolation threshold of carbon black in a polymer matrix and its application to antistatic fibre," *Scientific Reports*, vol. 9, no. 1, pp. 1-12, 2019.
- [79] R. Socher, B. Krause, S. Hermasch, R. Wursche, P. Potschke, "Electrical and thermal properties of polyamide 12 composites with hybrid fillers systems of multiwalled carbon nanotubes and carbon black," *Composites Science and Technology*, vol. 71, pp. 1053-1059, 2011.
- [80] Y. Sun, H.-D. Bao, Z.-X. Guo, J. Yu, "Modeling of the electrical percolation of mixed carbon fillers in polymer-based composites," *Macromolecules*, vol. 42, pp. 459-463, 2009.
- [81] J.H. Lee, Y.K. Jang, C.E. Hong, N.H. Kim, P. Li, H.K. Lee, "Effect of carbon fillers on properties of polymer composite bipolar plates of fuel cells," *Journal of Power Sources*, vol. 193, pp. 523-529, 2009.



- [82] Y. Konishi, M. Cakmak, "Nanoparticle induced network self-assembly in polymer-carbon black composites," *Polymer*, vol. 47, pp. 5371-5391, 2006.
- [83] H. Pierson, "Graphite Structure and Properties," in *Handbook of Carbon, Graphite, Diamond, and Fullerenes*, Park Ridge, Noyes Publications, 1993, pp. 43-68.
- [84] H. Pierson, "The Element Carbon," in *Handbook of Carbon, Graphite, Diamond, and Fullerenes*, Park Ridge, Noyes Publications, 1993, pp. 11-42.
- [85] J.F. Annett, R.E. Palmer, R.F. Willis, "Surface dielectric response of a semimetal: electron-energy-loss spectroscopy of graphite," *Physical Review B*, vol. 37, no. 5, pp. 2408-2414, 1988.
- [86] N. Deprez, D.S. McLachlan, "The analysis of the electrical conductivity of graphite powders during compaction," *Journal of Physics D: Applied Physics*, vol. 21, pp. 101-107, 1988.
- [87] L. McKeen, "Introduction to Use of Plastics in Food Packaging," in *Plastic Films in Food Packaging: Materials, Technology and Applications*, Waltham, William Andrew, 2013, pp. 1-16.
- [88] Y. Ohki, N. Fuse, T. Arai, "Band gap energies and localized states in several insulating polymers estimated by optical measurements," in *2010 Annual Report Conference on Electrical Insulation and Dielectric Phenomena*, West Lafayette, IN, 2010.
- [89] H. Ulf, W. Rohde-Liebenhau, "Nylon 12," in *Polymer Data Handbook*, Oxford, Oxford University Press, 1999, pp. 225-229.
- [90] W. Griehl, D. Ruestem, "Nylon 12 - preparation, properties, and applications," *Industrial nad Engineering Chemistry*, vol. 62, no. 3, pp. 16-22, 1970.
- [91] J.P. Kruth, X. Wang, T. Laoui, L. Froyen, "Lasers and materials in selective laser sintering," *Assembly Automation*, vol. 23, no. 4, pp. 357-371, 2003.
- [92] C. Majewski, H. Zarringalam, N. Hopkinson, "Effect of the degree of particle melt on mechanical properties in selective laser-sintered Nylon-12 parts," *Journal of Engineering Manufacture*, vol. 222, no. B, pp. 1055-1064, 2008.
- [93] H. Zarringalam, N. Hopkinson, N.F. Kamperman, J.J. de Vlieger, "Effects of processing on microstructure and properties of SLS Nylon 12," *Materials Science and Engineering*, Vols. 435-436, pp. 172-180, 2006.
- [94] M. Schmid, R. Kleijen, M. Vetterli, K. Wegener, "Influence of the origin of polyamide 12 powder on the laser sintering process and laser sintered parts," *Applied Sciences*, vol. 7, no. 5, pp. 462-477, 2017.
- [95] Arkema, "Thermoplastic Powders for Powder Bed Fusion," [Online]. Available: <https://www.arkema.com/en/markets-solutions/3d-printing/powder-bed-fusion/>. [Accessed 27 April 2020].
- [96] W. Zhou, Y. Gong, L. Tu, L. Xu, W. Zhao, J. Cai, Y. Zhang, A. Zhou, "Dielectric properties and thermal conductivity of core-shell structured

- Ni@NiO/poly(vinylidene fluoride) composites," *Journal of Alloys and Compounds*, vol. 693, pp. 1-8, 2017.
- [97] D. Michael, P. Mingos, D.R. Baghurst, "Applications of microwave dielectric heating effects to synthetic problems in chemistry," *Chemical Society Reviews*, vol. 20, pp. 1-47, 1991.
- [98] S. Marinković, C. Sužnjević, M. Djorđević, "Pressure dependence of the electrical resistivity of graphite powder and its mixtures," *Physica Status Solidi (a)*, vol. 4, pp. 743-754, 1971.
- [99] J. Yacubowicz, M. Narkis, "Dielectric behavior of carbon black filled polymer composites," *Polymer Engineering and Science*, vol. 26, no. 22, pp. 1568-1573, 1986.
- [100] H.S. Dahiya, N. Kishore, R.M. Mehra, "Effect of percolation on electrical and dielectric properties of Acrylonitrile Butadiene Styrene/graphite composite," *Journal of Applied Polymer Science*, vol. 106, pp. 2101-2110, 2007.
- [101] X. Wang, Z. Li, Z. Chen, L. Zeng, L. Sun, "Structural modification of carbon black for improving the dielectric performance of epoxy based composites," *Advanced Industrial and Engineering Polymer Research*, vol. 1, pp. 111-117, 2018.
- [102] W. Zhou, Q. Chen, X. Sui, L. Dong, Z. Wang, "Enhanced thermal conductivity and dielectric properties of Al/ $\beta$ -SiCw/PVDF composites," *Composites: Part A*, vol. 71, pp. 184-191, 2015.
- [103] H. Haus, "Polarization," in *Electromagnetic Fields and Energy*, Englewood Cliffs, NJ, Prentice-Hall, 1989, pp. 1-47.
- [104] R. Maxson, "Electrophysiotherapeutic apparatus". US Patent 2448540A, 7 September 1948.
- [105] R.S. Ferrari-John, J. Katrib, P. Palade, A.R. Batchelor, C. Dodds, S.W. Kingman, "A tool for predicting heating uniformity in industrial radio frequency processing," *Food and Bioprocess Technology*, vol. 9, no. 11, 2016.
- [106] D. L. Bourell, T. J. Watt, D. K. Leigh, B. Fulcher, "Performance limitations in polymer laser sintering," *Physics Procedia*, vol. 56, pp. 147-156, 2014.
- [107] M. Hashiba, T. Hino, Y. Hirohata, H. Shinbori, S. Deyama, H. Chiyoda, "Gas desorption and adsorption properties of carbon based material used for cathode ray tube," *Thin Solid Films*, vol. 332, pp. 141-145, 1998.
- [108] "Nylon 12 PA Laser Sintering Material Specifications," Stratasys Direct Manufacturing, 2015.
- [109] "AC/DC Module User's Guide," COMSOL Multiphysics® v. 5.3, Stockholm, Sweden, 2017.
- [110] A. Kiraly, F. Ronkay, "Temperature dependence of electrical properties in conductive polymer composites," *Polymer Testing*, vol. 43, pp. 154-162, 2015.

- [111] "Heat Transfer Module User's Guide," COMSOL Multiphysics® v. 5.3, Stockholm, Sweden, 2017.
- [112] T.C. Mokhena, M.J. Mochane, J.S. Sefadi, S.V. Motloung, D.M. Andala, "Thermal conductivity of graphite-based polymer composites," in *Impact of Thermal Conductivity on Energy Technologies*, IntechOpen, 2018, pp. 181-197.
- [113] T.T. Diller, R. Sreenivasan, J. Beaman, D. Bourell, J. LaRocco, "Thermal model of the build environment for polyamide powder selective laser sintering," in *Proceedings of the Solid Freeform Fabrication Symposium*, Austin, TX, 2010.
- [114] M. Vasquez, B. Haworth, B. Hopkinson, "Optimum sintering region for laser sintered nylon-12," *Journal of Engineering Manufacture*, vol. 225, no. B12, pp. 2240-2248, 2011.
- [115] M. Yuan, T.T. Diller, D. Bourell, J. Beaman, "Thermal conductivity of polyamide 12 powder for use in laser sintering," *Rapid Prototyping Journal*, vol. 19, no. 6, pp. 437-445, 2013.
- [116] J. Wen, "Heat Capacities of Polymers," in *Physical Properties of Polymers Handbook*, New York, NY, Springer, 2007, pp. 145-154.
- [117] N. Bannach, "Phase change: cooling and solidification of metal," 12 August 2014. [Online]. Available: <https://www.comsol.com/blogs/phase-change-cooling-solidification-metal/>. [Accessed 13 May 2020].
- [118] S.K. Bohidar, R. Sharma, P.R. Mishra, "Functionally graded materials: A critical review," *International Journal of Scientific Footprints*, vol. 2, no. 4, pp. 18-29, 2014.
- [119] H. Mlejnek, "Some aspects of the genesis of structures," *Structural Optimization*, vol. 5, pp. 64-69, 1992.
- [120] O. Sigmund, "A 99 line topology optimization code written in Matlab," *Structural and Multidisciplinary Optimization*, vol. 21, pp. 120-127, 2001.
- [121] G. Rozvany, "Aims, scope, methods, and unified terminology of computer-aided topology optimization in structural mechanics," *Structural and Multidisciplinary Optimization*, vol. 21, pp. 90-108, 2001.
- [122] G. Rozvany, "A critical review of established methods of structural topology optimization," *Structural and Multidisciplinary Optimization*, vol. 37, pp. 217-237, 2009.
- [123] B. Alfaifi, J. Tang, Y. Jiao, S. Wang, B. Rasco, S. Jiao, S. Sablani, "Radio frequency disinfestation treatments for dried fruit: Model development and validation," *Journal of Food Engineering*, vol. 120, pp. 268-276, 2014.
- [124] S.L. Birla, S. Wang, J. Tang, H. Hallman, "Improving heating uniformity of fresh fruit in radio frequency treatments for pest control," *Postharvest Biology and Technology*, vol. 33, no. 2, pp. 205-217, 2004.

- [125] T.R. Kramer, F.M. Proctor, E. Messina, *The NIST RS274NGC Interpreter-Version 3*, Gaithersburg, MD: National Institute of Standards and Technology, 2000.
- [126] J. Allison, C. Sharpe, C.C. Seepersad, "Powder bed fusion metrology for additive manufacturing design guidance," *Additive Manufacturing*, vol. 25, pp. 239-251, 2019.
- [127] P.-H. Chen, H.-Y. Peng, H.-Y. Liu, S.-L. Chang, T.-I. Wu, C.-H. Cheng, "Pressure response and droplet ejection of a piezoelectric inkjet printhead," *International Journal of Mechanical Sciences*, vol. 41, pp. 235-248, 1999.
- [128] H.C. Nallan, J.A. Sadie, R. Kitsomboonloha, S.K. Volkman, "Systematic design of jettable nanoparticle-based inkjet inks: rheology, acoustics, and jettability," *Langmuir*, vol. 30, pp. 13470-13477, 2014.